Summer 8-14-2015

Targeted Magnetite Tissue Delivery for Antiretroviral Pharmacokinetics

Tianyuzi Li
University of Nebraska Medical Center

Recommended Citation

Li, Tianyuzi, "Targeted Magnetite Tissue Delivery for Antiretroviral Pharmacokinetics" (2015). *Theses & Dissertations*. 8.
https://digitalcommons.unmc.edu/etd/8

TARGETED MAGNETITE TISSUE DELIVERY FOR ANTIRETROVIRAL PHARMACOKINETICS

by

Tianyuzi Li

A DISSERTATION

Presented to the Faculty of
the University of Nebraska Graduate College
in Partial Fulfillment of the Requirements
for the Degree of Doctor of Philosophy

Pharmacology & Experimental Neuroscience
Graduate Program

Under the Supervision of Professor Howard E. Gendelman

University of Nebraska Medical Center
Omaha, Nebraska

July, 2015

Supervisory Committee:

Michael D Boska, Ph.D.	JoEllyn M McMillan, Ph.D.
Xinming Liu, Ph.D.	Joseph A Vetro, Ph.D.

TARGETED MAGNETITE TISSUE DELIVERY:

IMPLICATIONS TOWARDS IMPROVING ANTIRETROVIRAL PHARMACOKINETICS

Tianyuzi Li, Ph.D.

University of Nebraska Medical Center, 2015

Supervisor: Howard E Gendelman, M.D.

Pharmacokinetics and pharmacodynamics studies are required for bench to bedside translation of any new drug, formulation or device. Multifunctional magnetite nanocarriers enable magnetic resonance imaging tracking of nanomaterial encased antiretroviral drugs serving to improve the effectiveness of formulation developments. Targeting ligands used to deliver nanoparticles to HIV harboring cells can be tested using multifunctional magnetite nanocarriers. To this end, two types of magnetite nanocarriers were developed. These included small magnetite antiretroviral therapy particles. The second were ALN-PEG coated magnetite particles for testing macrophages targeting ligands. Overall, these works should serve to speed the development of long acting nanoformulated ART to improve access and effectiveness of treatment regimens for the infected human host.

To my husband Wei An, my son Stanley Lee An, my parents Quanyou Li and Shenlian Tian

ACKNOWLEDGEMENTS

I would like to thank many people whose support made this work possible. My mentor and adviser, Dr. Howard E Gendelman provided the needed support and opportunities to complete this work in his lab. His enthusiasm for my science, my development and my project was inspirational. I was also fortunate to work with many wonderful individuals in Gendelman lab who were both great collaborators and friends. I thank members of my graduate supervisory committee, Drs. Michael D Boska, Xinming Liu, JoEllyn M McMillan, and Joseph A Vetro, for their encouraging and constructive feedback and research directions. I wish to especially thank Dr. Liu for showing me entrance to the scientific world and in helping me stay focused on my research project. I would like to thank my family for their support and my husband Wei An especially. He has managed to accomplish so many things under so much pressure, and he always tries his best on doing everything. Special thanks to my mother Shenlian Tian, father Quanyou Li, mother-in-law Huili Lv and father-in-law Maosen An, who have supported me throughout my graduate studies, and more stressful times when my son Stanley arrived.

TABLE OF CONTENTS

LIST OF FIGURES

LIST OF TABELS

LIST OF ABBREVIATIONS

3TC	Lamivudine
AchR	Nicotinic acetylcholine receptor
AcLDL	Acetylated low-density lipoprotein
ALN	Alendronate
ALN-PEG	ALN conjugated polyethylene glycol
ALN-PEG-FA	Folic acid conjugated ALN-PEG
ART	Antiretroviral therapy
ATV	Atazanavir
Azido-PEG	Azide-terminated peg5k
AZT	Azidothymidine
CLRs	C-type lectin receptors
CPMG	Carr-purcell-meiboom-gill
CP-PGs	Cyclopentenone prostaglandins
DAB	3,3'-diaminobenzidine
DAPI	4′,6-diamidino-2-phenylindole
DLS	Dynamic light scattering
DMSO	Dimethylsulfoxide
DPML	Dexamethasone palmitate incorporated in mannosylated liposomes
DSPC	1,2-distearoyl-sn-glycero-3-phosphorylcholine
DSPE-PEG$_{2000}$	1,2-distearoyl-*sn*-glycero-3-phosphoethanolamine-n-[methoxy-(polyethylene glycol)-2000]
EFV	Efavirenz
FBP	Folate binding protein
FDA	Food and Drug Administration
FDC	Follicular dendritic cells
FePt	Monodisperse iron-platinum
FePt@Van	Vancomycin-conjugated fept nanoparticles conjugates
FLASH	Fast low angle shot
FR	Folate receptor
FTC	Emtricitabine

Gp	glycoprotein
HDL	High density lipoprotein
HLA	Human leukocyte antigens
HPLC	High performance liquid chromatography
Iba-1	Ionized calcium binding adaptor molecule 1
LDL	Low density lipoprotein
LipoCardium	Liposome-based pharmaceutical formulation
LPS	Lipopolysaccharide
Mag-GNS	Magnetic gold nanoshells
MDM	Monocyte-derived macrophage
MHC	Major histocompatibility complex
MPS	Mononuclear phagocyte system
MR	Mannose receptor
MRI	Magnetic resonance imaging
MTB	Mycobacterium tuberculosis
MTX	Methotrexate
NanoART	Nanoformulated ART
Nef	Negative regulatory factor
NHS	N-hydroxysuccinimide
NIR	Near infrared
NP	Nanoparticles
NTA	Nitriloacetic acid
OA	Oleic acid
OCT	Optical cutting temperature compound
PBS	Phosphate-buffered saline
PCR	Polymerase chain reaction
PD	Pharmacodynamic
PDI	Polydispersity index
PIC	Pre-integration complex
PK	Pharmacokinetics
PLGA	Polylactic-co-glycolic acid
RANTES	Regulated on activation, normal T cell expressed and secreted
Rev	Regulator of viral protein expression

RGD	Arginine-glycine-aspartic acid
ROI	Region of interest
RVG	Rabies virus glycoprotein
SMART	Small magnetite antiretroviral therapy
SPIO	Superparamagnetic iron oxide
Tat	transactivator of transcription
TBBS	Tris buffered saline with tween
TDF	Tenofovir
TEM	Transmission electron microscopy
TGA	Thermal gravimetric analysis
THF	Tetrahydrofuran
Tnf-α	Tumour necrosis factor α
UPLC-MS/MS	Ultra performance liquid chromatography tandem mass spectrometry
VCAM-1	Vascular cell adhesion molecule-1
VIF	Viral infectivity protein
VPR	Viral protein R
WHO	World Health Organization

1. Chapter I. Introduction

1.1. The HIV pandemic

The first cases of acquired immunodeficiency syndrome (AIDS) were reported in 1981. Today tens of millions of people have died of AIDS-related causes. At the end of 2013, there are approximately 35 million people currently living with human immunodeficiency virus (HIV), the virus that causes AIDS. HIV has become one of the world's most significant health and development medical challenges. Intensive research had been done during the past 34 years. Directed collaborative and aggressive efforts on behalf of scientists and physicians worldwide has increased our knowledge of the HIV replication cycle, disease pathogenesis, innate and adaptive immunity and antiretroviral therapy (ART).

In 1987, azidothymidine (AZT) became the first approved HIV treatment. Since then, approximately 30 drugs were approved for treatment of HIV patients. Nearly a decade later, major breakthroughs were made with the introduction of a therapy that combined several drugs to limit the viral resistance and limit HIV replication to very low and often undetectable levels. Combination ART markedly reduced disease morbidity and mortality (1, 2). However, ART can only suppress the replication of HIV and does not eliminate it. Thus, new drugs, delivery systems and vaccines are in desperate need if an HIV cure is to be achieved.

1.2. HIV virology

HIV is a 100nm retrovirus including two identical copies of single-stranded RNA. It is a highly organized structure consisting of a cylindrical center surrounded by a sphere-shaped lipid bilayer where the viral envelope is attached. There are three structural genes contain the information needed to make structural proteins for new virus particles: gag which encodes the structural proteins of the core and matrix, env which encodes the viral envelope glycoproteins, pol which encodes the viral enzyme (3).

The basic structure of HIV is as follows (Figure 1):

- The viral envelope, outer coat of the virus, consists of two layers of lipids: glycoprotein (gp) 120 and the transmembrane gp41. Both of the two are encoded by env gene and are embedded in the viral envelope where "spikes" are formed. The lipid membrane is taken from the host cell during the budding process.

- The HIV matrix proteins consists of the p17 protein that is encoded by gag gene. They lie between the envelope and core.

- The viral core contains the viral capsid protein p24 which is encoded by gag gene. The viral capsid surrounds two single strands of RNA as well as enzymes needed for HIV replication, including reverse transcriptase, protease, ribonuclease, and integrase. All the enzymes are encoded by pol gene.

Viral particle membrane is consisting of glycoprotein heterodimer complexes. Gp120 and transmembrane gp41 are the two major elements in the complex. The function of gp120 and gp41 is to mediate host cell recognition, cell attachment as well as cell invasion in CD4+ T lymphocytes and monocyte-macrophages (4). Beneath the viral lipoprotein membrane, is the matrix protein p17, the core proteins p24 and p6, and the nucleocapsid protein p7 which bound to the RNA. The capsid contains viral genome, reverse transcriptase, integrase and protease (5).

HIV virus is also characterized by its accessory/regulatory genes which encode proteins with various regulatory or immuno-modulatory functions (6), including tat (transactivator of transcription), rev (regulator of viral protein expression), vif (viral infectivity protein), vpr (viral protein R) and nef (negative regulatory factor). Among them, tat protein, which promotes the expression of HIV gene, is expressed very early after infection. The rev protein ensures the export of the messenger RNA and genomic RNA from nucleus to cytoplasm. The function of the other accessory HIV proteins is less well understood.

Previous sequencing studies using samples from HIV infected patients identified that HIV virus DNA primarily exist in CD4+T lymphocytes, which suggests that CD4+ T cell is the primary target of HIV infection. Subsequent mechanistic studies revealed the life cycle of HIV replication in T cells. Before entering cells, the glycoproteins on viral envelope target and bind to the CD4 receptor on host cells. This interaction triggers a conformational change of viral glycoproteins and facilitate the interaction of virus and another two co-receptor on host cells, CCR5 and CXCR4. The interaction with co-receptors again triggers a conformational change of viral envelope proteins gp41 and enable virus envelope pierces host cells membrane. Next, virus envelope fuses with host cell membrane and virus genetic materials and enzymes are injected into host cells, while the envelope of HIV is left on the membrane of host cells.

The genetics materials of virus was coated by a protective viral capsid, which is digested in host cells to expose the containing viral RNA as well as key viral enzymes such as reverse transcriptase. Reverse transcriptase converts viral RNA into a single strand cDNA by using host deoxynucleotides and this process occurs within a complex consist of viral capsid and another host cell protein cyclophilin A. The synthesis of viral DNA occurs together with the degradation of its template RNA, which is mediated by the RNase activity of viral reverse transcriptase. Notably, this reverse transcription process leads to random mutation on the newly synthesized single strand DNA due to the poor proofreading capability of viral reverse transcriptase. These random mutations provide essential mechanism for virus to evolve and/or gain drug resistance. The single strand

DNA is later converted into double strand DNA through another round of reverse transcription. After the double strand DNA is generated, viral integrase binds with this viral double strand DNA and carries it into the host cell nucleus. Integrases also create a nick on host chromosome to facilitate the integration of viral DNA into host DNA and gaps are repaired by host cell DNA repair mechanism. The success of viral DNA integration marks the completion of HIV infection. Followed by the viral DNA integration, mechanisms of host cell DNA replication, RNA transcription and protein translation produce virus genomic materials and viral proteins. They are transported and gathered at cell membrane for virus packaging. Some viral enzymes can mediate these process. For example, viral protein Tat can transactivate transcription by binding the 5’ end of the viral DNA, resulting 1000 time increase of viral transcription (7).

To generate functional virus particle, the HIV DNA firstly produce a pre-protein encoded by pr55, which will be digested to become functional elements. Similarly, Gag-Pol is also a pre-protein and can be digested into three functional enzymes: protease, integrase, and reverse transcriptase. Pre-protein Gp160 migrates to the cell membrane and is cleaved during the virion formation to form the envelope protein gp41 and gp120. These proteins and host membrane proteins are incorporated on the plasma membrane to form viral envelope outside the capsid that contains the viral RNA genome. HIV particles are then assembled and released from host cells (8) (9) (10) (11).

1.3. HIV pathogenesis

There are two types of HIV, HIV type 1 and 2 (HIV-1, 2). There is limited knowledge about HIV-2, which has not been widely seen outside of Africa. Studies have shown striking similarities but also significant differences between the two. HIV-2 infection in human host is characterized by lower transmission rates, longer asymptomatic stage, slower decline in numbers of CD4+ T lymphocytes and lower mortality rate (12-15).

HIV-1 transmission occurs through exchange of body fluid from a virus carrier to an uninfected recipient. Body fluids that can pass HIV-1 virus include blood, semen, pre-seminal fluid, rectal and vaginal fluids, and breast milk. To transmit HIV, virus containing body fluids must contact with a mucous membrane or damaged tissue or be directly injected into the bloodstream.

HIV enters CD4+ cells via its interactions with CD4 receptor and the chemokine coreceptors, CXCR4 or CCR5. Cells bearing CD4 and chemokine receptors are activated CD4 T lymphocytes, resting CD4 T cells, monocytes and macrophages, and dendritic cells.

HIV infect cells mainly through two mechanisms. One is cell-free transmission and the other one is cell-to-cell transmission. In cell-free transmission, virus floats in plasma and infects T cells it encounters. In the cell-to-cell transmission, the virus is exchanged by direct cell contact between infected T cells and uninfected T cell.

In the first 24 hours after infection, HIV infects dendritic cells within the mucous membranes and skin. Within five days, HIV infects dendritic cells and makes their way to the lymph nodes as well as peripheral blood where spreading viral replication ensues. In response to the viral antigen, CD4+ T lymphocytes are then recruited and migrate to lymph nodes where they become activated and proliferate with the help of pro-inflammatory cytokines (16). As the consequence, a suitable environment for viral replication is created (17).

HIV infected cells have a shortened life span as a result of the virus infection (18) and immune system destruction occurs concomitantly. On the other hand, HIV infected monocytes are more resistant to the toxicity of HIV (19). Thus, monocyte-macrophages act as reservoirs of HIV and effectors of tissue damage in organs such as the lung and brain.

1.4. The immune response to HIV

HIV infection leads to abnormality of immune system. Recent studies revealed immune responses may control HIV infection, although this defensive effect is mostly transient. These responses include humoral immune response, in which cytokines and antibodies are produced to prevent HIV infection, and cellular immune response, in which T cells are activated to enhance their cytotoxicity. Details are shown below.

Cellular immune responses: At the early stage of HIV infection, CD4+ T cells decrease dramatically while CD8 T cells are activated and expanded up to 20 times higher. Activated CD4+ T cells promote maturation of CD8+ T cells, which possess specific and effective anti-HIV toxicity. A number of cytokines are secreted to enhance this cellular immune responses, such as interleukin-2 and interferon gamma. CD8+ T cells can also secrete chemokines to block the entry of HIV virus to host cells, such as CCR5 ligands RANTES (regulated on activation, normal T cell expressed and secreted), MIP-1 and CXCR4 ligand SDF-1. Notably, a clinical study identified a reverse correlation between level of these cytokines and HIV disease progression (20).

Humoral responses: The humoral immunity includes B cells and their production of antibodies. Four to eight weeks after HIV infection, anti-HIV antibodies start to be generated. These antibodies mainly target viral envelope proteins. Thus cell-free virions are their main targets, although some antibodies may also destroy HIV-infected cells. Most antibodies cannot prevent cell to cell transmission of HIV.

As mentioned above, although immune response provide transient defensive mechanisms to control HIV infection, HIV may develop strategy to escape from these defensive immune response, such as antigenic variation (21) (22), decreasing surface MHC molecules expression as well as depleting CD8+ T cells, etc. (23). Another limitation of anti-HIV antibody is that virus is able to mutate their envelop protein to evade attack of antibodies and B-cells are not able to keep up with HIV antigens mutations speed.

As more CD4 + T cells are eliminated with the infection progress, the CD4 T cell count keeps dropping. When it reaches below 200 cells/mm^3 blood, the patient develop AIDS (24) (25). To obtain a better picture of disease progression, CD4/CD8 cell ratio should be monitored which has a normal ratio of about 1 to 1.5. If the disease is progressing, the CD4/CD8 ratio will be <1, indicating disease progression.

1.5. Antiretroviral therapy

ART consists of a combination of drugs targeting the human HIV life cycle and act on different viral life cycle targets. It has led to profound decreases in morbidity and mortality rates in AIDS patient. It also provides effective treatment to prevent transmission from male to females and in men who have sex with men (26, 27). Inhibitors of HIV-1 reverse transcriptase and the viral protease, when used together, cause dramatic reductions in viremia. For many treated patients, plasma levels of HIV-1 RNA drop to less than the limits of detection as a result of ART treatment.

ART fall into five classes: 1) nucleoside reverse transcriptase inhibitors (NRTI) and nucleotide reverse transcriptase inhibitors (NtRTI), 2) non-nucleoside reverse transcriptase inhibitors (NNRTIs), 3) protease inhibitors, 4) entry inhibitors and 5) integrase inhibitors.

Seven nucleoside/nucleotide analogs are Food and Drug Administration (FDA) approved HIV-1 drugs. NRTIs were the first medicines to be approved for the treatment of HIV. It stop HIV from replicating within cells by inhibiting the reverse transcriptase. NRTIs are analogues of the deoxynucleotides needed to synthesize the viral DNA. They compete with the natural deoxynucleotides for incorporation into the growing viral DNA chain. Once incorporated, these analogs stop following incorporation of deoxynucleotides into the DNA chain because of the absence of a 3’ OH group. The next incoming deoxynucleotide cannot form the next 5’ – 3’ phosphodiester bond needed to extend the DNA chain. Thus, when an NRTI or NtRTI is incorporated, viral DNA synthesis is halted (28).

While only one NtRTI, Tenofovir is currently approved at this time, they act very much the same way as NRTI (29). Nucleoside analogs are converted into nucleotide by undergo phosphorylation to become active by the body. Nucleotide analogues bypass this step, given that they are already chemically activated.

Five NNRTIs are available on the market. The first NNRTIs was approved in 1996. It stop HIV replicating within cells by interfering with HIV's reverse transcriptase. Unlike NRTIs, NNRTIs are not incorporated into the viral DNA. Instead it inhibits reverse transcriptase by binding to an allosteric site of the enzyme (30). Since NNRTI-resistance mutations can emerge relatively quickly (31) (32), an NNRTI is generally used in combination with NRTIs.

There are two types of entry inhibitor, Enfuvirtide and Maraviroc. Binding of viral envelope to its primary receptor CD4 is mediated by gp120, the surface subunit of the envelope. In its native form, the envelope glycoprotein is a heterotrimer of three gp120 molecules and three molecules of gp41 (33) (34). Binding to CD4 conformational changes gp120 and enable its binding to one of two chemokine receptors, CCR5 or CXCR4. Co-receptor binding allows the fusion peptide of the gp41 to insert into the target cell membrane, resulting in fusion of virus with the cell membrane (35). Maraviroc works by targeting CCR5 which located on human helper T-cells. The drug binds to CCR5, thereby blocking the HIV protein gp120 from associating with the receptor. Enfuvirtide is a peptide drug which must be injected to give. It acts by interacting with the N-terminal heptad repeat of gp41 of HIV to form an inactive hetero six-helix bundle, therefore preventing fusion of the virus with the host membrane (36).

Currently, there are three integrase inhibitors. Integrase facilitates the interaction between viral DNA and a number of cellular cofactors which is indispensable for establishing the pre-integration complex (PIC) (37) (38). Upon the formation of the PIC, integrase remove a nucleotide from viral DNA exposes hydroxyl groups of its 3’ terminal. Subsequently, PIC enters the host nucleus and creates binding sites on host DNA by exposing its 5’ phosphate groups. This allows the viral DNA integrates into host DNA, which is also called strand transfer and is facilitated by integrase, followed by gaps repair (39). Integrase inhibitors disturb strand transfer process and therefore preventing the viral DNA from integrating into host DNA.

FDA also approved 8 protease inhibitors. When cells are infected by HIV, they produce viral proteins for viral packaging. However, newly synthesized viral protein are not infectious unless they are cleaved by the vial protease. Protease inhibitors target viral protease and therefore block viral precursor from maturation. Notably, protease inhibitors are frequently used in combination with other categories of ART drugs to effectively treat HIV infection.

ART is now recommended for all adults with HIV infection. Recommended initial regimens include 2 NRTIs (abacavir/lamivudine (3TC) or tenofovir (TDF) disoproxil fumarate/emtricitabine (FTC)) and a third single or boosted drug, which should be an integrase inhibitor (dolutegravir, elvitegravir, or raltegravir), a NNRTIs (efavirenz (EFV) or rilpivirine) or a boosted protease inhibitor (darunavir or atazanavir) (40).

The World Health Organization (WHO) published the leading recommendations for antiretroviral treatment in 2013. The favored recommendation is a fixed-dose combination of TDF; 3TC or FTC and EFV.

It had been shown that the concentration of HIV-1 in plasma drops by impressive ~99% in the first two weeks of ART treatment (41). New drugs with high potency, low toxicity and tolerability increase the feasibility of early initiated lifelong treatment.

However, even with current ART regimens, HIV is not completely eradicated and virus is able to remain as a life-long infection due to its ability to stay hidden in restricted manner within infected blood cells. It is becoming clear that the viral reservoirs present a major obstacle to clear infection.

1.6. HIV reservoir

Many viruses have established mechanisms to escape from host immune surveillance through the process of natural selection (42). This persistence always involves viral reservoirs, on both cellular and anatomical level. In the mid-1990s, a series of reports showed the existence of provirus within latently infected resting life-long memory CD4+ T lymphocytes (2, 43) and these virus reservoirs, even after successful administration of ART, can produce infectious virus following cellular activation (44-46). Therefore HIV is able to remain a chronic life-long infection due to its ability to stay hidden in cellular reservoirs. These reservoir cells contain the genetic code of HIV. Anatomical reservoirs of HIV are located throughout the body including the brain, lymphoid tissue, bone marrow, and the genital tract.

In patients receiving ART, latent replication-competent HIV-1 provirus has been demonstrated in resting memory CD4$^+$ T lymphocytes while low levels of virus can also be found in resting naïve CD4$^+$ T cells (47). This latent reservoir, drives viral rebound once ART is stopped. It is established soon after primary HIV-1 infection (48) and can be activated by pro-inflammatory cytokines (49). The presence of HIV-1 in peripheral blood monocytes of patients with current ART treatment has also been demonstrated (50).

1.7. Macrophage viral reservoir

In addition to HIV-1–infected CD4+ T cells, monocyte-macrophages may also be a key source of the viral reservoir in HIV-1–infected people. Macrophages are referred to as mononuclear phagocytes (MP) cells derived from circulating monocytes, and are terminally differentiated, non-dividing cells (51). They can be found in various tissues using different names (e.g. microglia in the brain, alveolar macrophages in the lung, or Kupffer cells in the liver) (51). MP are well known to phagocytose cellular debris and pathogens and act as antigen presenting cells (52). The life spans of the MP vary. Inflammatory macrophages die after a few days (53), whereas microglia or alveolar macrophages can live from several weeks up to years. MP are widely distributed in many different tissues and are able to infiltrate virtually all organs especially the brain, this make them a critically contributor to the spread of HIV in human body (54, 55).

HIV in infected MP are more resistant to lentiviral replication’s cytopathic effects when compared with activated CD4+ T lymphocytes (56). Second, HIV has evolved sophisticated mechanisms to prolong the life span of infected MP (57, 58). Therefore long-lived MP may harbor the virus for long period of time, thus constituting HIV reservoirs and posing a major obstacle to virus eradication from infected individuals. Mature HIV-1 can be found in intracellular vesicles of MP, suggesting macrophages' ability to store HIV particles (59). Research showed that MP could store infectious HIV for weeks (60).

Also, it has been shown that high molecular weight substances, including broadly neutralizing antibodies are excluded from the virus storing compartments (61, 62). HIV particles harboring in compartments like exosomes and microvesicles can also be released to facilitate and increase HIV dissemination (63). This may also contribute to HIV rapidly transfer from MP internal compartments to adjacent CD4+ T cells and uninfected monocyte-derived macrophage (MDM) (64, 65). In summary, MP make a prefect hideout for HIV particles, and growing evidence suggesting an important role of macrophages in the failure of the immune system to achieve HIV clearance within the acute and chronic phases of infection (Figure 2). Therefore, targeting delivery ART to monocytes/macrophages should be a powerful means to eliminate not only HIV but an opportunity to use the very mechanisms the virus uses to escape destruction. In this manner depots within MP can be ensured for drug depot and delivery.

1.8. ART MP delivery schemes

MP are widely distributed in many tissues to recognize and clear altered and senescent cells, invading particulates, as well as macromolecular ligands via a multitude of receptors (66). This endocytosis/phagocytosis tendency of MP of foreign particles has provided an opportunity for the efficient delivery of therapeutic agents to these cells with the aid of carefully designed colloidal drug delivery systems.

To further take advantage of this property, nanoparticles have been designed to maximize macrophages uptake by altering nanoparticles physicochemical properties, which play a major role in its interaction with serum proteins and MP, as well as adding targeting ligands to the cell surface. The rate and the site of the uptake of the nanoparticles by MP are also influenced by the injected dose, blood flow and local tissue damage (67).

Physicochemical properties of nanoparticle including size, charge, and shape which can have a very significant effect on the nanoparticles' efficiency to target MP. In addition to controlling the physicochemical properties of nanoparticle to facilitate macrophages targeting, ligands can be incorporated into nanoparticle to specifically target monocytes and macrophages.

Using a ligand targeting strategy has advantages of potentially increasing target specificity and avoiding the need for cationic lipids to trigger intracellular delivery. Successful homing of drugs to the target would help the nanoparticles to preserve its integrity, avoid interception by normal cells, penetrate interposing membranes, and reduce the drug dose and potential to diminish the side effects.

In this section we highlight some approaches researchers have used to target MP for drug delivery and treat HIV disease. Identifying molecular targets within this cell population will help in creating new therapeutic solutions. A variety of ligands for macrophage targeting have been studied including peptides, antibodies, proteins, polysaccharides, glycolipids, glycoproteins, and lectins, which make use of mononuclear phagocytes characteristic receptor expression and phagocytic innate processes.

1.8.1. Peptides

Cell targeting peptides and cell penetrating peptides have been used to achieve cell specific targeting and improve cell uptake. Tuftsin is a natural macrophage activator tetrapeptide (Thr–Lys–Pro–Arg) which is a part of the Fc-portion of the heavy chain of the leukophilic immunoglobulin G. This tetrapeptide is released after enzymatic cleavage as the free peptide fragment (68). Tuftsin is known to not only bind specifically to monocytes, macrophages and polymorphonuclear leukocytes, but also enhances their natural killer activity (69). These include potentiation of various cell functions, such as phagocytosis, pinocytosis, motility, immunogenic response, bactericidal and tumoricidal activities (69). Conjugating tuftsin onto the nanoparticles can not only homing the drug to macrophages but also to stimulate these cells non-specifically against infections (70). In one study, tuftsin were grafted on the surface of the drug-loaded liposomes which were given to Mycobacterium tuberculosis (MTB) infected animals twice weekly. Rifampin, an anti-MTB drug delivered for 2 weeks in tuftsin-bearing liposomes was at least 2,000 times more effective than the free drug in lowering the load of lung bacilli in infected animals (71).

A short nicotinic acetylcholine receptor (AchR)-binding peptide (YTIWMPENPRPGTPCDIFTNSRGKRASNG) derived from the rabies virus glycoprotein (RVG) was used to target AchR expressed on macrophage/microglia surface. This peptide was fused to nona-D-arginine residues (RVG-9dR) to enable siRNA binding (72). SiRNA bond to RVG-9dR was able to induce gene silencing in wild type macrophages and microglia, but not in cells from AchR-deficient mice, confirming targeting specificity (72). Intravenous injection with RVG-9dR-complexed siRNA in mice reduced the lipopolysaccharide (LPS) induced TNF-α levels in blood as well as in the brain, leading to a significant reduction in neuronal apoptosis (72). These results demonstrate that macrophages targeting peptide RVG-9dR provides a platform for siRNA delivery to macrophages and across blood brain barrier to microglia and that suppression of TNF-α can potentially be used to suppress neuroinflammation in vivo.

Arginine-glycine-aspartic acid (RGD)-peptide has also been used to target integrin receptors expressed by monocytes (73). The interaction between the RGD domain on the integrin molecule and the integrin receptor on leukocytes stimulates phagocytosis by polymorphnuclear leukocyte (e.g.neutrophils) (74). In an *ex vivo* experiment using negatively charged uncoated and RGD-coated liposomes, amount of drug recovered from monocytes/neutrophils was 57.8±4.1% and 73.5±5.8% respectively (75). Also, RGD-coated magnetic liposomes brain levels of the drug was 1.5-fold compared to uncoated magnetic liposomes and 9.1-fold compared to free drug solution. Results clearly showed better localization of RGD-coated vesicles within these cells (75).

1.8.2. Mannose

C-type lectin receptors (CLRs) are pattern recognition receptors which are expressed by macrophages and dendritic cells, with highly conserved carbohydrate-recognition domains that bind sugar moieties (e.g., mannose, fucose, and glucan) on the surface of certain pathogens (76). The C-type designation is from their requirement for calcium for binding. Ligand recognition by CLRs leads to pathogen internalization via receptor mediated endocytosis. The pathogen is subsequently digested and presented as antigen to T cells in the context of major histocompatibility complex (MHC) class I or MHC II, or both. These receptors play numerous roles in immune function including antigenic recognition, endocytosis, antigen presentation and immune responses.

The mannose receptor (MR) is a 175-kD C-type lectin type I transmembrane protein (77). Immune cells including alveolar macrophages, peritoneal macrophages, monocyte-derived dendritic cells, and Kupffer cells constitutively express high levels of the MR. Macrophages and DCs can therefore be targeted via mannosylated nanoparticles which have been shown to preferentially target CLRs on macrophages and DCs repeatedly, resulting enhanced cellular uptake in vitro and in vivo. Mannosylation has been achieved by the incorporation of various ligands. A novel mannosylated cholesterol derivatives, cholesten-5-yloxy-*N*-(4-((1-imino-2-d-thiomannosylethyl)amino)butyl)formamide (Man-C4-Chol), as a ligand for mannose receptors was studied by several groups (78-80). Hasida and colleagues tried to deliver dexamethasone palmitate to alveolar macrophages with selective targeting of mannosylated liposomes via mannose receptor-mediated endocytosis after intratracheal administration. Dexamethasone palmitate incorporated in mannosylated liposomes (DPML) was extensively retained in alveolar macrophages compared with free drug ($P < 0.001$) and dexamethasone palmitate containing bare liposomes in LPS induced lung inflammation in rats. The anti-inflammatory effects of DPML in rats showed significantly inhibited tumor necrosis factor α, interleukin-1β etc in the lung (78).

4-aminophenyl-α-d-mannopyranoside was conjugate to liposomes to deliver drugs to alveolar macrophages to study biodistribution (81) or to treat respiratory intracellular parasitic infections (82). The pulmonary administration and antibacterial activity of ciprofloxacin-loaded mannosylated liposomes against the intracellular bacteria were assessed. The antibacterial activity against various intracellular bacteria such as *Chlamydophila pneumonia*, *Legionella pneumophila*, *Listeria monocytogenes* and *Francisella tularensis* as estimated by pharmacokinetic (PK) and pharmacodynamic (PD) analyses was higher using liposomal systems (82). However, efficacy studies using the pathogens need to be performed to support the results.

Other mannose ligands used to target macrophages including alkylmannosides (83), Mann-His-C4-Chol (84) and Man2DOG (85).

1.8.3. Antibody

Antibody therapy has received wide attention due to its ability to selectively target cells through receptor-specific interactions (86). Antibody–nanoparticle conjugates have the potential to elicit effective active targeting and release of therapeutic targets at the disease site, while minimizing off-target side effects caused by dosing of normal tissues.

Class II human leukocyte antigens (HLA) present antigenic peptides to regulatory T cells. Follicular dendritic cells (FDC), B lymphocytes, activated CD4+ T-cells and antigen presenting cells like macrophages are abundant in lymphoid tissues and all express substantial levels of the HLA-DR. Liposomes bearing surface-attached anti-HLA-DR antibodies make an interesting approach to target specifically HIV reservoirs as well as free HIV particles trapped in the FDC network. In one study, the ability of liposomes bearing anti-HLA-DR fragments at the end termini of PEG chains to target HLA-DR expressing cells was evaluated. Study showed that anti-HLA-DR bearing liposomes accumulated better in brachial and cervical lymph nodes than that of conventional liposomes upon a single subcutaneous injection. In contrast, other organs like liver did not show especially higher levels when compared to the unmodified liposomes (87).

Growth factors produced by injured endothelial cells induce expression of vascular cell adhesion molecule-1 (VCAM-1) in monocytes/macrophages. Antiproliferative cyclopentenone prostaglandins (CP-PGs) are powerful anti-inflammatory agents, with the help of VCAM-1 antibody, one group developed a negatively charged liposome-based pharmaceutical formulation (LipoCardium) which direct CP-PGs towards the injured arterial wall cells of atherosclerotic mice. After 4 months in a high-lipid diet, all low-density lipoprotein receptor-deficient control mice died from myocardium infarction or stroke in less than 2 weeks, whereas LipoCardium-treated mice even though still under high-lipid diet completely recovered from vascular injuries (88).

1.8.4. Folic acid

A vitamin, folic acid has recently emerged as a prominent targeting moiety capable of specific interaction with cells expressing the folate receptor (FR). FR consists of a high affinity ($K_d \sim 10^{-9}$ - 10^{-10}) folate binding protein attached to the membrane through a glycosylphosphatidyl-inositol anchor (89). Following binding of folate acid, rapid endocytosis delivers a fraction of the receptors into the cell (90). Importantly, covalent conjugation of protein, small molecules or even liposomes to folic acid does not alter its ability to bind the FR and undergo endocytosis (91); therefore, this makes folate acid a good targeting ligand to use to help drug enter cells by receptor-mediated endocytosis.

FR expression is restricted to few cell types, including kidney and placenta, while normal tissues express low or undetectable levels of FR (92). There are three major forms of the FR, FR-α, FR-β, and FR-γ. The FR-α isoform is present primarily in placenta, kidney, malignant tumors and various cancer cell lines (89). FR-β is expressed in the placenta, monocytic and myelocytic lineages of hematopoietic cells and certain leukemias while there is negligible expression of this molecule on other blood cells such as lymphocytes, granulocytes, or erythrocytes (89). In contrast, it is difficult to find FR-γ, which is primarily a secreted isoform of hematopoietic origin under normal conditions (93).

The feasibility of using FRβ to mediate the specific delivery of molecules is based on several unique biologic characteristics of the FR. Interestingly, very little folate conjugate is detected in blood cells or bone marrow after intravenous administration, cause FR-β has been found to be functionally inactive although they can be easily detected by anti-FR-β antibodies (94). Recently, it has been reported that activated but not resting macrophages, possess a functionally active FR-β, thus FR as a marker of macrophage activation enables the facile labeling, isolation, and treatment of these inflammatory cells with folate conjugates (95).

FR has been actively pursued to target nanocarriers to the site of inflammation for improved delivery and efficacy in arthritis and atherosclerosis (96, 97). In one study FA conjugated dendrimers was used to target macrophages and deliver methotrexate (MTX) as an antiinflammatory agent in a collagen-induced arthritis model in rats. The administration of FA- and MTX-conjugated dendrimer yields significant and beneficial protection from the inflammatory characteristics of collagen-induced arthritis (96).

Anti-FRβ antibody was also used to target FRβ+ macrophages. A recombinant immunotoxin consisting of the truncated Pseudomonas exotoxin A conjugated to an anti-FRβ antibody has been reported to reduce the progression of atherosclerotic lesions in younger and older individuals (97).

1.8.5. Other

Acetylated low-density lipoprotein (AcLDL) is taken up by macrophages via scavenger receptors. One study investigated the delivery of AZT, an anti-HIV agent, to macrophages using AcLDL (98). Since the incorporation of AZT into AcLDL was found to be low, a prodrug was synthesized. Two cell lines expressing scavenger receptors were used to evaluate cellular uptake: J774.A (mouse macrophage) and U937 (human monocyte). A 10-fold increase was found with the AcLDL/prodrug as compared to the free drug. Moreover, addition of a 30-fold excess of AcLDL to the culture medium inhibited the uptake, confirming the specificity of the mechanism. The presence of excess

AcLDL was found to inhibit the cellular uptake of AcLDL/prodrug by macrophages while excess high density lipoprotein or low density lipoprotein was found to have little effect, suggesting that the AcLDL/prodrug complex is taken up into macrophages via the scavenger receptor (98).

A more indigenous approach to macrophage targeting was adapted recently where the glucan shell of baker's yeast was used as a delivery vector to successfully ferry the cargo to the macrophages (99). The β1,3-D-glucan shells loaded with siRNA were successfully taken up by macrophages through dectin-1 receptor or other glucan receptor-mediated pathways upon oral delivery of nanoparticles containing as little as 20 μg kg^{-1} siRNA directed against tumour necrosis factor α (Tnf-α). Its messenger RNA was depleted in macrophages recovered from the peritoneum, spleen, liver and lung, and lowered serum Tnf-α levels (99).

1.9. Inorganic nanoparticles

In biomedical applications, progress in utilizing inorganic nanoparticles has advanced rapidly due to the extensive amount of work done in the synthesis and modification of the materials (100-103). The reasons being those inorganic nanoparticles provide a robust framework in which two or more components can be combined to give multifunctional capabilities. An example can be seen in polymer-coated superparamagnetic iron oxide nanoparticles. By conjugating multiple components such as drugs (104), tissue or cell targeting moieties, or siRNA (105) to the polymeric coating, not only can these multifunctional nanoparticles deliver drug to specific site, they can also be imaged inside the body by both magnetic resonance and fluorescence imaging, by conjugating fluorescent molecules.

Magnetic resonance imaging (MRI) is a powerful and non-invasive diagnostic techniques for living organisms based on the interaction of protons with the surrounding molecules of tissues. The current MRI contrast agents are in the form of either paramagnetic complexes like gadolinium (Gd^{3+}) or manganese (Mn^{2+}) chelates (106) or superparamagnetic iron oxide (SPIO) particles which exhibits superparamagnetic property (107). These contrast agents are used to increase the sensitivity of MRI for detecting various pathological processes.

Paramagnetic complexes accelerate the longitudinal (T_1) relaxation of water protons and therefore exhibit bright contrast in in T_1 weighted MRI. Gadolinium diethylenetriaminepentaacetate has been the most widely used T_1 contrast agent. In contrast, SPIO nanoparticles accelerate the transverse (T_2) relaxation of water protons and exhibit dark contrast.

To synthesize SPIO, several methods had been explored such as co-precipitation, microemulsion, thermal decomposition, and hydrothermal synthesis (108). Commercially used T_2 contrast agents, such as Ferridex and Combidex, are synthesized via co-precipitation method, which involves the simultaneous precipitation of Fe^{2+} and Fe^{3+} species in aqueous media, and stabilized with hydrophilic polymers, such as dextran. SPIO synthesized by co-precipitation method are generally coated with hydrophilic polymers, making them highly stable under physiological conditions. However, they are generally polydisperse, poorly crystalline and limited in their capacity of drug loading and the drug dissociates rapidly after administration intravenously.

Recently, SPIO synthesized by the thermal decomposition method have been extensively studied, as they are highly uniform, crystalline and size-controllable (109). These high quality hydrophobic iron oxide nanoparticles have been transferred to the aqueous phase using amphiphilic polymers, phospholipids, and silica shells.

1.10. Multifunctional Magnetic Nanoparticles

Recently, techniques and procedures for producing monodispersed and size-controllable magnetic nanoparticles have advanced considerably which leads to very active explorations of the applications of magnetic nanoparticles, including biomedicine. Because of the potential benefits of multimodal functionality in biomedical applications, magnetic nanoparticles have been used to design and fabricate multifunctional nanoparticles.

Currently, there are two strategies to fabricate magnetic nanoparticle-based multifunctional nanostructures (Figure 3). The first strategy, single magnetic nanoparticle functionalization, involves attaching drugs, antibodies, proteins and dyes to the surface of magnetic nanoparticles. The other method integrates the magnetic nanoparticles as well as other functional nanocomponents into polymer based nanoparticles, to achieve better stability and more functions. Because they can exhibit several features synergistically and achieve more than one function simultaneously, such multifunctional magnetic nanoparticles could have unique advantages in biomedical applications.

For the application of the first strategy, Vancomycin-conjugated monodisperse iron-platinum (FePt) nanoparticles (FePt@Van conjugates) were manufactured. Bacteria at low concentrations are hard to detect and usually require long induction times before further analysis. FePt@Van conjugates can detect Gram-positive bacteria at exceptional low concentrations $\sim 10^1$ cfu/mL via polyvalent ligand−receptor interactions (110). After mixing of FePt@Van conjugates with a solution of bacteria, the aggregation of bacteria can be observed by electron micrograph when external magnetic field applied in a very small area. The detection limit of this method is comparable to that of assays based on polymerase chain reaction (PCR), but this method is faster than when the bacterium count is low and is particularly useful when PCR is inapplicable.

Protein, genetic materials, organelles, and cells separation and purification is another way to use single multifunctional magnetic particles (111, 112). For example, using dopamine as a robust anchor, the successful synthesis of nitriloacetic acid (NTA)-terminated magnetic nanoparticles offers a simple and versatile platform for separating six histidine-tagged protein (113, 114). The target proteins cover the surface of the nanoparticles effectively and quickly, reducing the overall unoccupied surface area for nonspecific absorption of proteins thus achieving higher specificity than microparticles. Moreover, NTA-terminated magnetic nanoparticles can be used without pretreatment of the cell lysate and these nanoparticles are reusable without losing efficiency.

For the application of the second strategy, in one study, drug delivery, cell targeting, magnetic manipulation, MRI and fluorescence imaging are simultaneously achieved using a multifunctional mesoporous silica nanoparticle (115). Mesostructured silica spheres were labeled with fluorescent dye and coated with hydrophilic groups to prevent aggregation. Water-insoluble anticancer drugs and SPIO were encapsulated inside and cancer-specific targeting agents were conjugated to the particle's surface (115). The targeting ligand modification increased the drug payload delivery into human cancer cells relative to that into non-cancerous cells. The potential to simultaneously monitor and deliver molecules to the targeted tissue region will be highly beneficial for both imaging and therapeutic purposes.

Hyeon and co-workers have manufactured a combination of magnetic nanoparticles and gold nanoshells to develop a novel nanomedical platform for diagnostic MRI and simultaneous photothermal therapy (116). Magnetic gold nanoshells (Mag-GNS) consisting of gold nanoshells embedded with magnetic Fe_3O_4 nanoparticles was fabricated (Figure 4). Amino-modified silica spheres were used to covalently attach Fe_3O_4 nanoparticles stabilized with 2-bromo-2-methylpropionic acid through a direct nucleophilic substitution reaction between the bromo groups and the amino groups. Then gold nanoparticles were attached to silica spheres through residual amino groups. Eventually, gold nanoshells with embedded Fe_3O_4 nanoparticles were formed around the silica spheres, Anti-HER2/neu was also linked on the surface of the Mag-GNS resulting in the formation of the cancer cell targeting Mag-GNS. SKBR3 breast cancer cells targeted by these Mag-GNS were able to be detected by a clinical MRI system and selectively killed by near infrared (NIR) radiation. Especially, the targeted cancer cells were rapidly destroyed upon their short exposure to femtosecond laser pulses with an NIR wavelength and a low power compared to the use of a continuous laser (116).

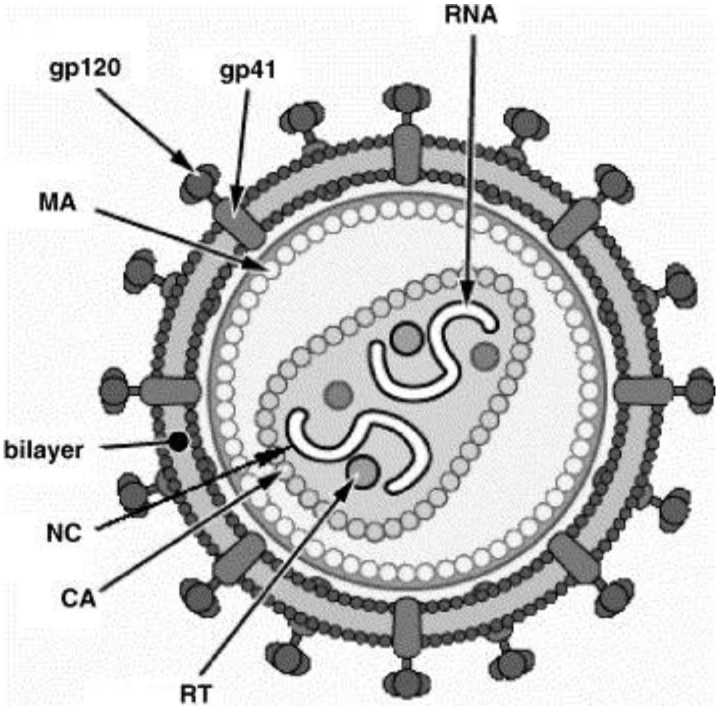
RNA
gp120
gp41
MA
bilayer
NC
CA
RT

FIGURE 1 DIAGRAM OF HIV MATURE VIRIONS

The lipid bilayer is of cellular origin and includes aproximately 72 spikes of the viral Env glycoproteins and some cellular proteins. The principal structural proteins forming the core are p17, p24 and p7 (Figure is adapted from Sierra S *et al*, *J Clin Virol*. 2005 Dec;34(4):233-44)

Drug Class	Generic Name (acronyms)
➢ **Nucleoside Reverse transcriptase Inhibitors (NRTIs)**	
NRTIs block reverse transcriptase, an enzyme HIV needs to make copies of itself.	• Abacavir (abacavir sulfate, ABC) • Didanosine (delayed-release didanosine, ddI) • Emtricitabine (FTC) • Lamivudine (3TC) • Stavudine (d4T) • Tenofovir disoproxil fumarate (tenofovir DF, TDF) • Zidovudine (azidothymidine, AZT, ZDV)
➢ **Non-Nucleoside Reverse Transcriptase Inhibitors (NNRTIs)**	
NNRTIs bind to and later alter reverse transcriptase	• Delavirdine (delavirdine mesylate, DLV) • Efavirenz (EFV) • Etravirine (ETR) • Nevirapine (extended-release nevirapine, NVP) • Rilpivirine (rilpivirine hydrochloride, RPV)
➢ **Protease Inhibitors (PIs)**	
PIs block HIV protease, an enzyme HIV needs to make functional viral proteins	• Atazanavir (atazanavir sulfate, ATV) • Darunavir (darunavir ethanolate, DRV) • Fosamprenavir (fosamprenavir calcium, FPV) • Indinavir (indinavir sulfate, IDV) • Nelfinavir (nelfinavir mesylate, NFV) • Ritonavir (RTV) • Saquinavir (saquinavir mesylate, SQV) • Tipranavir (TPV)
➢ **Integrase Inhibitors**	
Integrase inhibitors block HIV integrase, an enzyme HIV used to integrate its genome to host genome.	• Dolutegravir (DTG) • Elvitegravir (EVG) • Raltegravir (raltegravir potassium, RAL)
➢ **Entry Inhibitors**	
Entry inhibitors block HIV from entering CD4 cells.	• Enfuvirtide (T-20) • Maraviroc (MVC)

TABLE 1 SUMMARY OF ART APPROVED BY FDA

(Data is from www.aidsinfo.nih.gov)

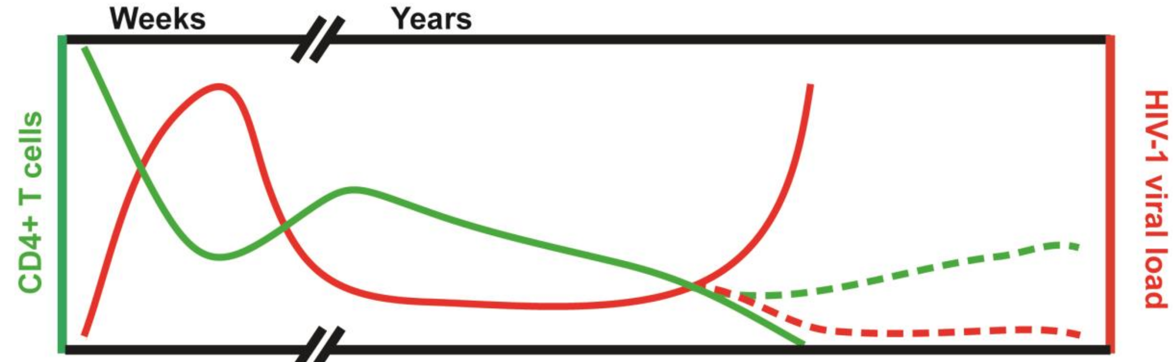

Acute	Chronic	AIDS	ART
Establishment of infection at the mucosa	HIV evasion from neutralizing antibodies	Virus production, T cell apoptosis	Persistently and latently infected HIV-1 reservoirs
Dissemination of HIV, CNS infiltration and crossing of the BBB	Ongoing organ and CNS infiltration, neuroinflammation	Development of HIV associated dementia	Neurological disorders despite ART
Innate and adaptive immune response	Participation in the adaptive immunity	Macrophage damage enhances risk for OI	Ongoing low levels of HIV-1 production

FIGURE 2 ROLE OF MACROPHAGES IN HIV-1 INFECTION AND DISEASE PROGRESSION

The number of CD4+ T cells and viral genome copies in plasma during the different phases of HIV-1 infection are presented in a schematic drawing. The dotted lines indicate the effects of antiretroviral therapy. The contribution of macrophages to each phase of HIV-1 infection is indicated below the scheme. (Figure is adapted from Koppensteiner *et al. Retrovirology.* 2012 Oct 4;9:82)

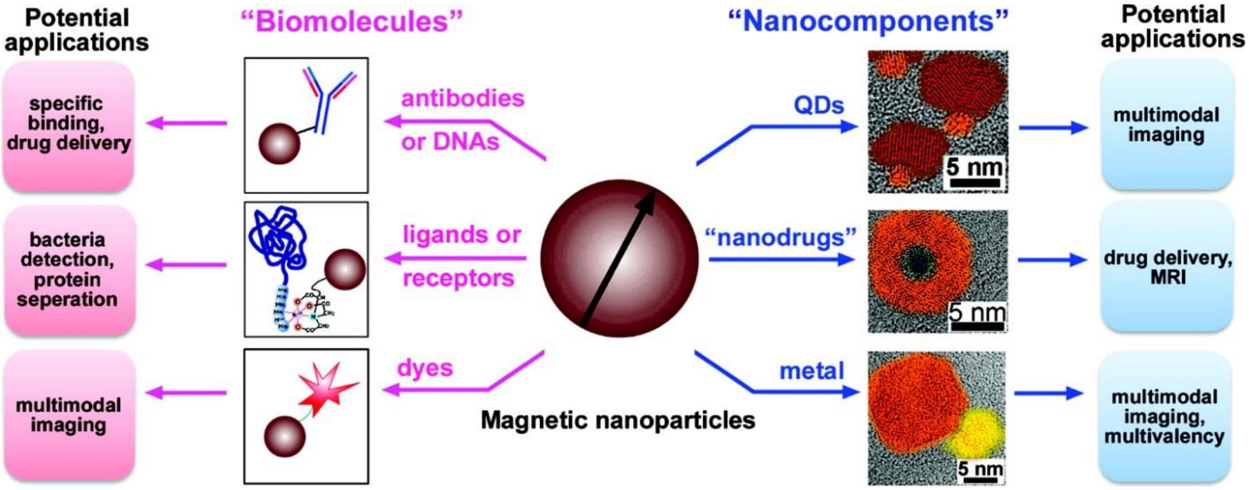
Potential applications
"Biomolecules"
"Nanocomponents"
Potential applications
specific binding, drug delivery
antibodies or DNAs
QDs
5 nm
multimodal imaging
bacteria detection, protein seperation
ligands or receptors
"nanodrugs"
5 nm
drug delivery, MRI
multimodal imaging
dyes
Magnetic nanoparticles
metal
5 nm
multimodal imaging, multivalency

FIGURE 3 TWO STRATEGIES TO FABRICATE MULTIFUNCTIONAL MAGNETIC NANOPARTICLES AND THEIR POTENTIAL APPLICATIONS

(Figure is adapted from Gao J *et al. Acc Chem Res.* 2009 Aug 18;42(8):1097-107.)

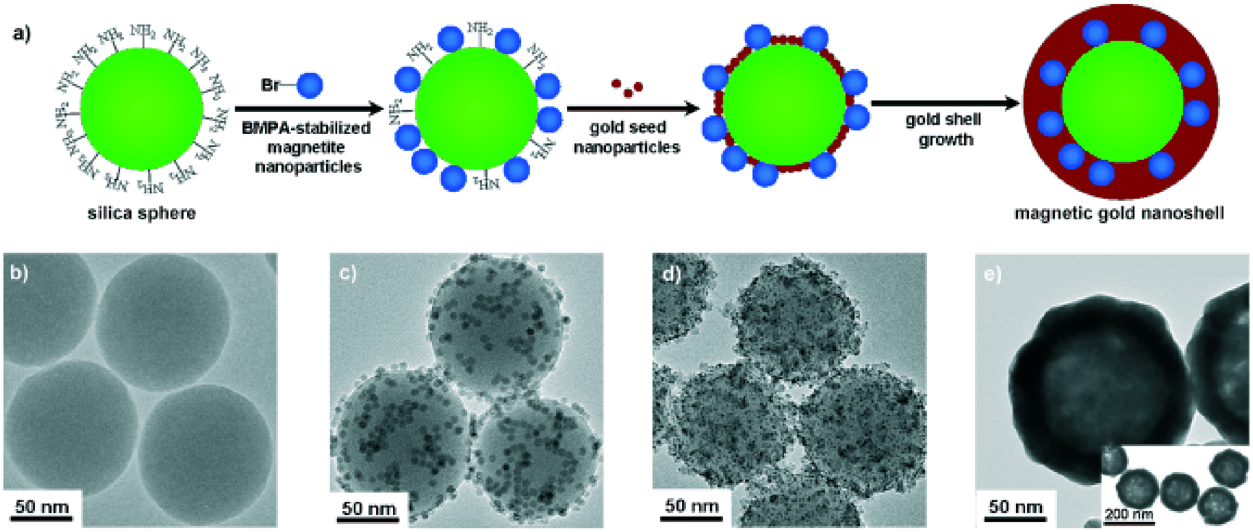
a)
silica sphere
NH_2
Br
BMPA-stabilized magnetite nanoparticles
gold seed nanoparticles
gold shell growth
magnetic gold nanoshell
b)
50 nm
c)
50 nm
d)
50 nm
e)
50 nm
200 nm

FIGURE 4 THE SYNTHETIC APPROACH AND TEM IMAGES OF THE PRODUCTS IN EACH STEP

a) Synthesis of the magnetic gold nanoshells (Mag-GNS). Transmission electron microscopy images of b) amino-modified silica spheres, c) silica spheres with Fe_3O_4 nanoparticles immobilized on their surfaces, d) silica spheres with Fe_3O_4 and gold nanoparticles immobilized on their surfaces, and e) the Mag-GNS. (Figure is adapted from Kim J *et al. Angew Chem Int Ed Engl*. 2006 Nov 27;45(46):7754-8.)

2. Chapter II. SMART particle manufacture and characterization

2.1. Abstract

Pharmacokinetics and pharmacodynamics study are the major factors that limiting the investigation of new nanoformulations. Multifunctional magnetite nanocarriers that integrate therapeutic agents into a single system have attracted considerable interest in theranostics integrating drug delivery and drug biodistribution. Using MRI to guide nanomaterial development can improve formulation development efficacy. To this end small magnetite ART (SMART) particle for treatment of HIV and simultaneously pharmacokinetics monitor were developed. We describe the fabrication of polymer nanocarriers co-encapsulating atazanavir (ATV), an HIV protease inhibitor, and magnetite nanoparticles which were synthesized by thermal decomposition method. Morphology of the SMART particles was studied by TEM. Drug loading were measured by high performance liquid chromatography (HPLC) and magnetite levels were measured by inductively coupled plasma mass spectrometry (ICP-MS). MDM uptake of SMART and ATV release of SMART from MDM was determined. Relaxivity of SMART in phosphate-buffered saline (PBS) and MDM was measured to make sure it is an efficient contrast agent for MRI. The relaxivity of SMART was found to be r2 = 6200.2 (s^{-1} ml mg^{-1}) in MDM and r2 = 7052.1 (s^{-1} ml mg^{-1}) in PBS.

2.2. Introduction

Treatment for HIV is arduous due to its long duration and multidrug regimens. Eradication of the HIV-1 in its infected human host will necessitate antiretroviral drug delivery to viral sanctuaries with the secondary elimination of latent or restricted infections (117). Therefore, there is an increasing demand for the development of new compounds and screening of targeted formulation aiming at virus harboring cells. Among the virus harboring cells, we are particularly interested in macrophages, not only because it is one of the major virus reservoirs, also because macrophage can serve as “Trojan horse” to store and deliver antiretrovius drug to other infected cells when treated with right particles. The right particles are the particles with size, shape and targeting ligand that macrophages prefers.

Paul Ehrlich’s “magic bullet” concept reveals the possibility that targeted delivery of drug with the help of ligand having well defined affinity for specific cells. Normally drug delivery systems targeting cell type other than mononuclear phagocyte system are modified to prevent from phagocytosis. Numerous formulations have been developed to study and optimize their ability to escape monocyte/macrophage clearance. However as the role of monocytes and macrophages in infectious disease, inflammatory diseases and cancer is better understood, there is a growing interest in targeting these cell for therapeutically benefit. People gradually realized that phagocytosis process can be harnessed for targeting drug delivery and greater knowledge of the mechanisms of binding and uptake has been learned recently. This idea is especially valuable in treatment of HIV given the fact that macrophages harbor the virus. Macrophages express a wide range of receptors including FR, scavenger receptors, mannose receptors and Fc-receptors can be targeted using ligands appending particles.

Targeting nanoparticles can facilitate drug delivery but, to achieve its potential, would require improved virus-target tissue drug bioavailability. Therefore, rapid noninvasive determination of targeted antiretroviral drug biodistribution is needed to study the targeting efficacy of targeting ligand in animal. One major hurdle towards achieving this goal is the dearth of any means to measure antiretroviral therapy distribution outside of plasma drug levels (118).

Liposomes and polymer nanoparticles are the two major types of nanoparticles that have been developed and evaluated for diagnostic and therapeutic purposes. Liposomes composed of natural lipids are attractive drug delivery systems because of their high biocompatibility, low immunogenicity, long systemic circulation and favorable pharmacokinetic profile. Specific targeted delivery can easily be achieved by conjugating a targeting ligand to the lipid molecule (119-121). Liposomal formulations including Doxil and DaunoXome are approved by FDA for clinical applications (120, 121). However, the possible intrinsic low drug loading capacity, fast release profiles of hydrophobic drugs and physical instability of liposomes limit their clinical applications of different drugs (122). Polymeric nanoparticles composed of synthetic polylactic-co-glycolic acid (PLGA) are another widely developed/studied drug delivery platform because of their high stability, relatively high drug loading capacity of all kinds of drugs, biodegradability, low toxicity, and controlled/sustained drug release profiles. Depending on particle composition, the drug release profiles of PLGA nanoparticles can be modulated to be within days, weeks or even months (123-125). However, the biocompatibility/immunogenicity of nanoparticles composed of synthetic polymers including PLGA is not as high as liposomes. Without further chemical modification, PLGA nanoparticles are rapidly removed from circulation by the MPS, resulting in short systemic circulation (122). In summary, both liposomes and PLGA nanoparticles are not independently structurally robust platforms. Thus, lipid-coated polymer nanoparticles, formed by combining synthetic polymers and natural lipids, have been developed as robust drug delivery platform to combine the advantages and avoid the disadvantages of liposomes and polymer nanoparticles (126).

We theorized that one way to achieve this is by combinations of imaging agent and ART in a single nanoparticle. If realized, such multicomponent nanoparticle could permit rapid pharmacokinetic and pharmacodynamics evaluations of ART in virus-target tissues, such as the lymph nodes and brain. Recent years, SPIO nanoparticles also referred to as magnetite have gained large attention due to its minimal toxicity profile and intrinsic superparamagnetic properties. The superparamagnetism magnetite exhibits make them respond to external magnetic field, which allow noninvasive tracking through MRI. Therefore we combined small magnetite and ART into a single nanoparticle and made SMART particle. By using the SMART particle, ART drug biodistribution would readily be quantitated by a conventional MRI scan. Such an approach would also provide the potential of delivering packaged medicines to sites of limited viral growth and serve, in part, to eliminate the viral reservoir. The approach was previously used for magnetically targeted cancer drug delivery utilizing T_2- or T_2^*-quantification by MRI (127-130).

To perform proof-of-concept studies we placed magnetite into lipid-coated PLGA nanoparticles with a commonly used antiretroviral protease inhibitor, ATV. The versatility of PLGA systems in terms of vesicle size, shape, composition and bilayer fluidity render them ability to incorporate a wide range of drugs and contrast agents like magnetite, and ability to carry cell-specific ligands (131). By combining PLGA, drug and magnetite, organic/inorganic hybrid composite biomaterials allowed drug distribution assessments with therapeutic ART delivery through a single MRI scan (132). SMART nanoparticles were screened for optimal uptake and retention in MDMs. This facilitated studies investigating the dynamics of in vivo drug tissue distribution. Collectively, the work provides the groundwork for the implementation of SMART systems for noninvasive drug PK for the inevitable goal of viral elimination.

2.3. Experimental Procedure

2.3.1. Synthesis Of SPIO

The magnetite particles were synthesized as follows: 6 mmol tris(acetylacetonato) iron(III) was mixed with 30 mmol 1,2-hexadecanediol, 18 mmol oleic acid, 18 mmol olylamine and 60 mL benzyl ether in a three-neck round-bottomed flask equipped with condenser, magnetic stirrer, thermograph and heating mantle and stirred under nitrogen. The mixture was slowly heated to 110^{o}C and kept at that temperature for 1 hour, then slowly heated to 200^{o}C. Reflux was kept after it reached 200^{o}C for 2 hours, then slowly heated to 298^{o}C and kept at reflux for another 1.5 hours. After cooling to room temperature, a dark homogeneous colloidal suspension was obtained. The suspension was precipitated in ethanol with a magnetic field. The black precipitate was dissolved in hexane with the presence of oleic acid and oleylamine and the solution was centrifuged at 3,800 x g for 10 min to remove any undispersed residue. The black solution was re-precipitated in ethanol and centrifuged at 10,000 x g for 30 min. Solid products were obtained by drying the precipitate under vacuum, generating the final dry particles.

2.3.2. Preparation of SMART particle

Preparation of the drug loaded 1,2-Distearoyl-sn-glycero-3-phosphorylcholine (DSPC) /mPEG-DSPE shell and PLGA core particle was as follows. First, a weighed amount of PLGA, ATV and magnetite were dissolved in chloroform (oil phase) with a weight ratio of magnetite to ATV of 1:3. Second, the aqueous phase was prepared by hydration of DSPC and mPEG-DSPE films. The oil phase was added to the DSPC and mPEG-DSPE aqueous solution drop-by-drop with constant stirring then sonicated for 60 seconds followed by a 20 second break under an ice bath. This procedure was repeated for three cycles. Chloroform was then removed by stirring overnight. Third, the particle suspension was centrifuged at 500 x g for 5 min. The supernatant fluids were collected to remove the aggregated nanoparticles. A high speed 50,000 x g centrifugation for 20 min was used to collect the nanoparticles. After washing twice with PBS, the nanoparticles were resuspended.

2.3.3. SMART size, surface charge and size distribution

SMART size and size distribution were measured by dynamic light scattering (DLS, 90Plus, Brookhaven Instruments Co. USA).The surface charge of the SMART particles was determined by ZetaPlus, a zeta-potential analyzer (Brookhaven Instruments Co. USA). The pH value and concentration of the particles dispersion were fixed before measurements of zeta potentials.

2.3.4. Morphology of the SMART particles

The shape and surface morphology of the SMART particles were investigated by transmission electron microscopy (TEM) performed as previously described (133). Samples were prepared from dilutions in distilled water of particle suspensions and dropped onto stubs. After air drying the particles were coated with a thin layer of gold then examined by TEM. The magnetic properties were determined by a Physical Property Measurement System.

2.3.5. SMART particle stability and release of drug in isotonic solution

SMART particles were dispersed in PBS and placed into a 10 k dialysis tube in 2 L PBS under stirring at 37°C. At 30 min and 1, 2, 3, 4, 6, 8 and 10 days, 100 µl of the suspension was collected. The supernatant was dissolved in 100 µl tetrahydrofuran (THF)/methanol (volume ratio 1:10) mixture. The amount of ATV and magnetite was measured by high-performance liquid chromatography (HPLC) and ICP-MS, respectively (133, 134).

2.3.6. Human monocyte isolation and cultivation

Human peripheral blood monocytes were obtained by leukapheresis from HIV-1 and hepatitis seronegative donors and purified by counter-current centrifugal elutriation (135). The cells were cultured at a concentration of 1×10^6 cells/ml at 37°C in a humidified atmosphere (5% CO2) in DMEM supplemented with 10% heat-inactivated pooled human serum, 1% glutamine, 50 µg/ml gentamicin, 10 µg/ml ciprofloxacin and 1000 U/ml recombinant human MCSF for 7 to 10 days until differentiation into macrophages occurred.

2.3.7. SMART uptake and retention by MDM

After differentiation, MDM were treated with 100 µM SMART particles, based upon ATV content. Uptake of SMART particles was assessed without medium change for 8 hours. Adherent MDM were collected by scraping into PBS, at 1, 2, 4 and 8 hours after treatment. Cells were pelleted by centrifugation at 500 x g for 8 min at 4°C. Cell pellets were briefly sonicated in 200 µl of methanol/acetonitrile (1:1) and centrifuged at 20,000 x g for 10 min at 4°C. To determine cell retention of SMART particles, MDM were exposed to 100 μM SMART particles for 8 hours, washed 3x with PBS, and fresh media without particles was added. MDM were cultured for an additional 15 days with half medium exchanges every other day. On days 1, 5, 10 and 15 after SMART treatment, MDM were collected as described for cell uptake. Cell extracts were stored at -80°C until HPLC and ICP-MS analysis (133).

2.3.8. Prussian blue staining of MDM retained SMART particles

MDM were treated with 100 μM SMART particles for 24 hours. Adherent MDM were washed 3x with PBS. Cells were fixed with 2% formalin/2.5% glutaraldehyde in PBS for 10 min then washed 2x with PBS. Fixed macrophages were treated with 5% potassium ferrocyanide/5% hydrochloric acid (1:1) for 10 min at room temperature. Following solution aspiration the cells were washed 2x with PBS. Stained cells were examined by light microscopy.

2.3.9. MRI phantoms and relaxivity measures

After differentiation, MDM were treated with 100 μM SMART particles, based upon ATV content. Twenty-four hours later the treatment medium was removed and the cells were washed 3× with 1 ml PBS. Cells were collected and suspended at different cell concentrations (0-5 x 10^6 cells/ml) in 1% agar gel. T_2-relaxtivity was measured by MRI. Magnetite content in the cells was quantitated by ICP-MS.

2.4. Results

2.4.1. Manufacture and characterization of SMART

SMART were composed of a hydrophobic PLGA/ATV/magnetite core and an amphiphilic DSPC and DSPE-PEG2k lipid shell (Figure 5A). DSPC and DSPE-PEG2k increased SMART stability and facilitated increased systemic formulation circulation times. Both ATV and magnetite are distributed homogeneously within the core of the particle. SMART was made using a single oil-in-water emulsion with lipid surfactants. After sonication amphiphilic lipids self-assembled to the monolayer surrounding PLGA/ATV/magnetite containing oil droplets, achieved through hydrophobic interactions. Evaporation of chloroform under continuous magnetic stirring allowed for the formation of lipid-coated solid PLGA/ATV/magnetite core. SMART was then purified by ultracentrifugation before further characterization. DLS results showed that the average size of the particles is 268 nm with a polydispersity index (PDI) of 0.2. TEM was employed to obtain the image that best reflects SMART particle morphology (Figure 5B, right panel). This illustrated that the particles were spherical in shape with narrow size distributions. A representative particle is shown by TEM, showing the SPIO contained within the particle’s core. Our preliminary in vitro results showed that SMART is very stable and ATV can slowly release from SMART up to 10 days.

2.4.2. SMART uptake, antiretroviral drug release and Prussian blue staining

After SMART particle characterizations were completed, the in vitro kinetics of MDM uptake and retention were determined. Our previous studies of nanoformulated ART (nanoART) uptake in MDM showed that > 95% of total uptake occurs by 8 hours for ATV nanoART (136-138). Up to 2 μg of ATV/ 10^6 cells was recorded in MDM at 8 hours with magnetite uptake reflective of particle composition (Figure 5C). The majority of the cells took up the magnetite as observed through Prussian blue staining (Figure 5D). Indeed, such staining demonstrated that magnetite-containing particles were readily incorporated in macrophages by 8 hours. The controlled and sustained release profile or ATV facilitates the application of the SMART particles for the delivery of antiretroviral drugs.

2.4.3. Measures of SMART particle relaxivity

Presence of SMART particles causing increased relaxivity (R_2 (s^{-1})) in tissue as a function of concentration (expressed as mg/ml magnetite). Concentration dependent relaxivity [r_2 (s^{-1} ml mg^{-1})] were determined using phantoms consisting of both free SMART particles (Figure 6A) and SMART particles taken up by MDM (Figure 6B). The magnetite concentrations in mg/ml contained by SMART in 1% agar gels were plotted against R_2 as measured by MRI. The relationship between R_2 and magnetite concentration of SMART in phantoms was linear within the range of the measured magnetite concentrations. The concentration dependent relaxivity of SMART was found to be r2 = 6200.2 (s^{-1} ml mg^{-1}) in MDM and r2 = 7052.1 (s^{-1} ml mg^{-1}) in PBS. The r_2 of SMART in MDM was used for noninvasive in vivo quantitation of magnetite concentration due to SMART influx using MRI in next chapter.

2.5. Discussion

The principle goal in developing this polymer system rests in the ability to utilize MRI scans to rapidly assess cell and tissue drug biodistribution. The idea is that the polymer-encased dual magnetite and drug particle would permit a clear determination of drug levels in virus-target tissues in a very short time interval. However, a hybrid particle is hard to manufacture due to the different nature of the components. So it is important to find the right composition. More magnetite will interfere with the incorporation of the ART drug, on the other hand, less magnetite will cause inefficient MRI signal. After testing different condition for drug release and relaxivity, we identified that the best drug vs magnetite ratio is 3:1, in which particles has slow drug release while has adequate magnetite to generate MRI signal.

Our DLS results showed that the average size of the particles is 268 nm with a PDI of 0.2. The narrow size distribution is linked to the DSPC, which serves to stabilize the polymeric SMART in the aqueous phase. The zeta potential of the particles is -45.2 mV, which provides its stability when suspended in aqueous media. Although DSPC is neutral when it is used as a particle coat it exhibits non-zero mobility in an external electric field. This may result in a higher negative charge since some anions bind to the neutral lipids making the surface more negatively charged.

The magnetite showed as a solid black dot on TEM picture of the SMART particles (Fig.4 B). Not only it can be found inside the SMART, but also small amount of magnetite attached to the surface of the SMART particles. It may be free magnetite that were trapped in between the polymer.

The relaxivity is an important factor to study a MRI contrast agent. Concentration dependent relaxivity of SMART in PBS and MDM showed slightly different result (7052 s^{-1} ml mg^{-1} vs 6200 s^{-1} ml mg^{-1}). It may be caused by the oxidization of magnetite during the 24 hours incubation with MDM. The regression of relaxivity in PBS is better than that in MDM (0.998 vs 0.961). It’s possible that it’s hard for the cell to reach homogeneous suspension in 1% agar gel.

The cell-based carriage and delivery of antiretroviral drugs to sites of active HIV-1 replication can facilitate slow release of drug for time periods measured in weeks or perhaps months. As the monocyte-macrophage is a cell target for HIV growth, the added benefit rests in the abilities to bring ART to subcellular sites of viral assembly. The next step would be to evaluate the correlation between magnetite and ATV after injected to the mice.

A

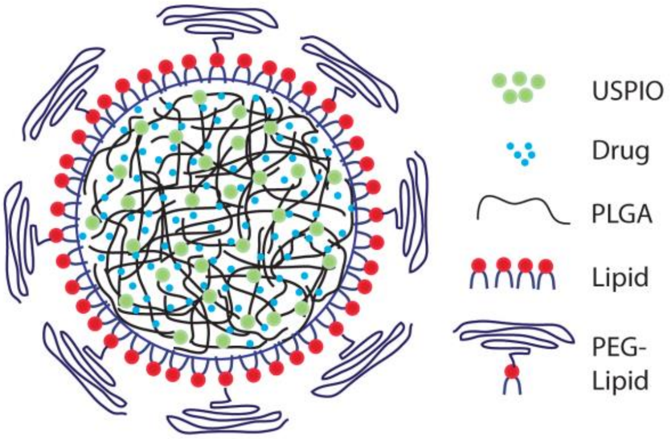

B

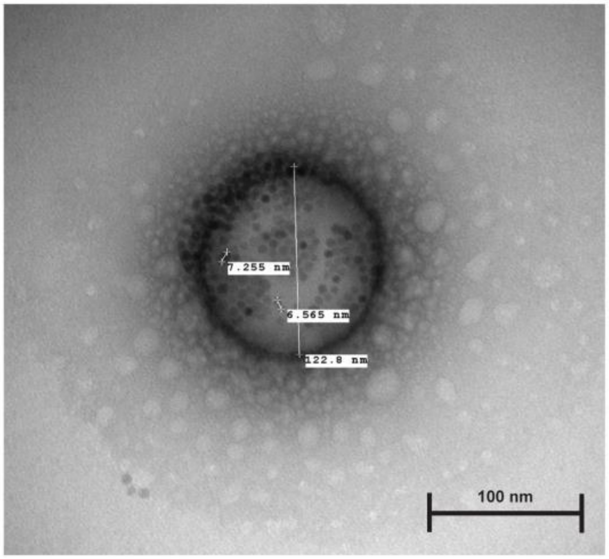

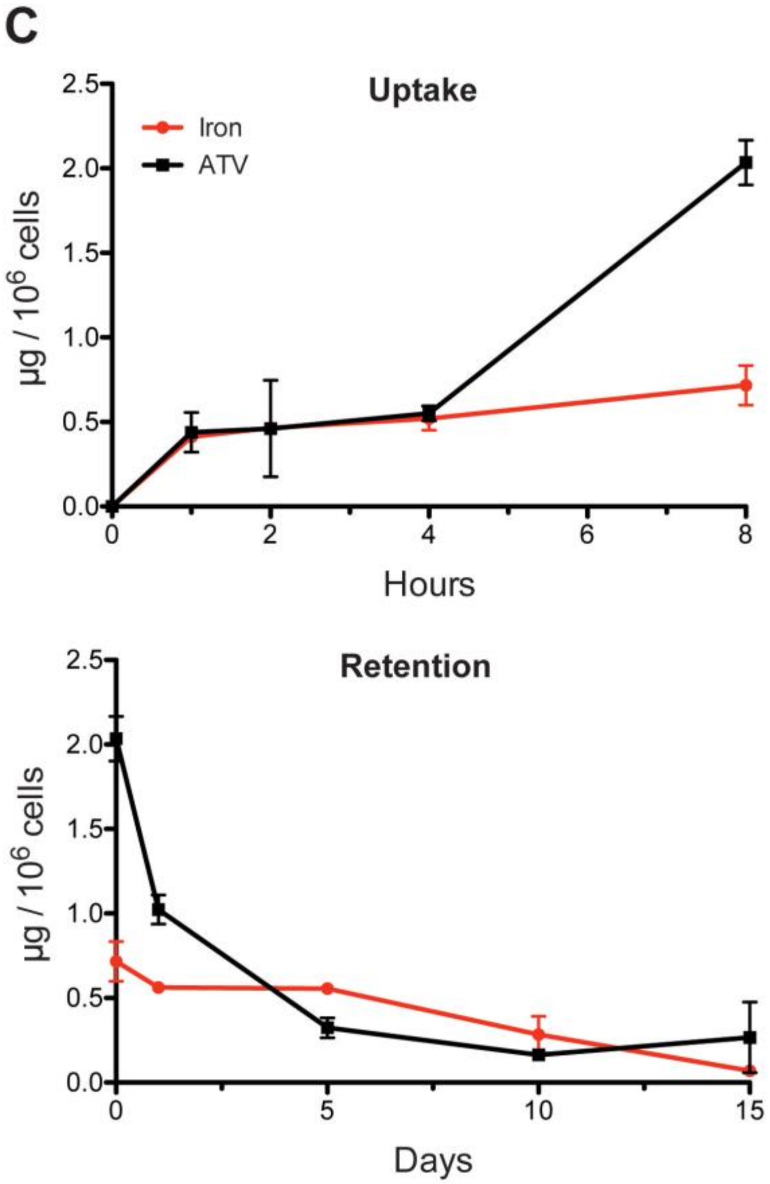
C
Uptake
Iron
ATV
2.5
2.0
1.5
1.0
0.5
0.0
µg / 10^6 cells
0
2
4
6
8
Hours
Retention
2.5
2.0
1.5
1.0
0.5
0.0
µg / 10^6 cells
0
5
10
15
Days

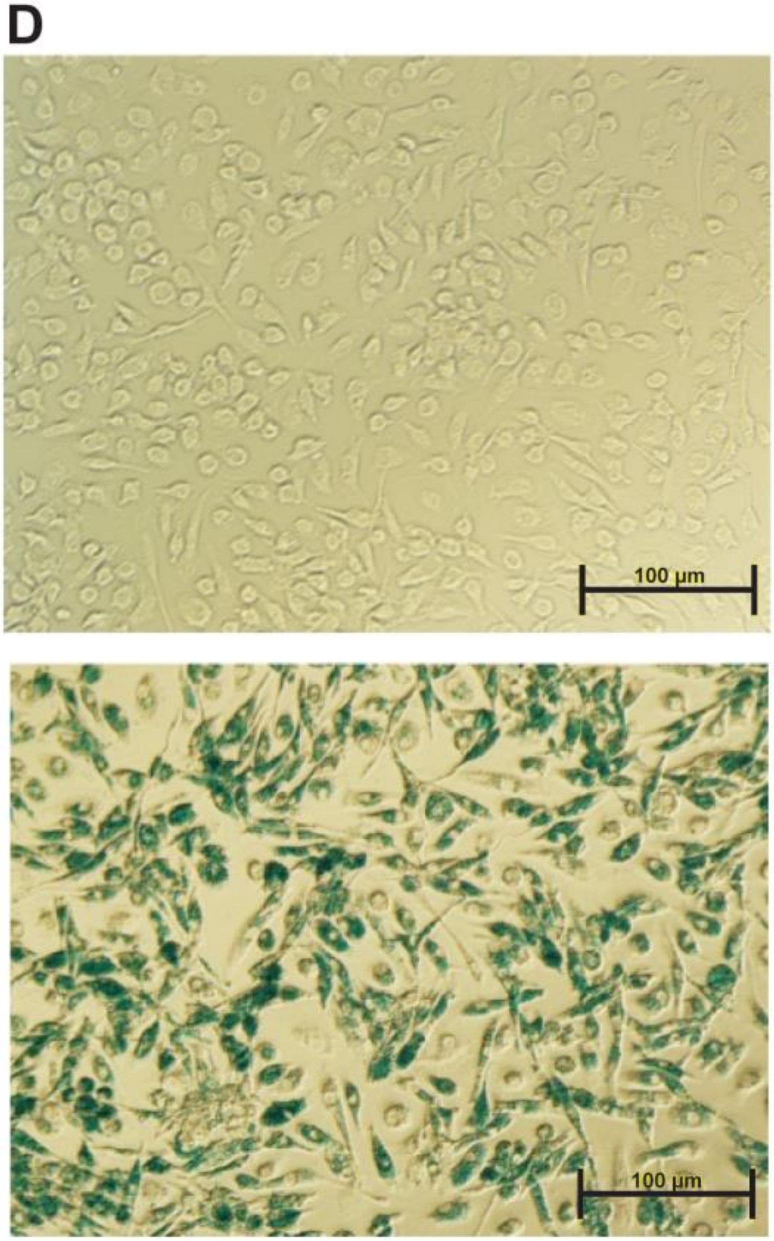
D
100 µm
100 µm

FIGURE 5 DEVELOPMENT OF SMART NANOPARTICLES

(A) The schematic structure of lipid-coated PLGA SMART. ATV and SPIO are well distributed within the PLGA matrix to form the core of SMART. The PLGA core is coated with lipid monolayer to form the shell of SMART. (B) Representative TEM of a single SMART particle. (C) Time course of uptake (upper panel) and retention (lower panel) of SMART in MDM., MDM were treated with 100 µM SMART (based on ATV content) for 1, 2, 4 and 8 hour uptake studies. For cell retention MDM were treated with 100 µM SMART for 8 hours, cell culture media was changed and cells were cultured for an additional 15 days. The cell lysates at indicated times were analyzed by HPLC and ICP-MS for ATV and magnetite quantification, respectively. Data represent the mean ± SEM, n = 3, for each time point. (D) Prussian blue staining of MDM. MDM were treated with PBS (negative control, upper panel) or 100 µM SMART (lower panel) for 24 hours, and then fixed with 2% formalin/2.5% glutaraldehyde and stained with 5% potassium ferrocyanide/5% hydrochloric acid (1:1).

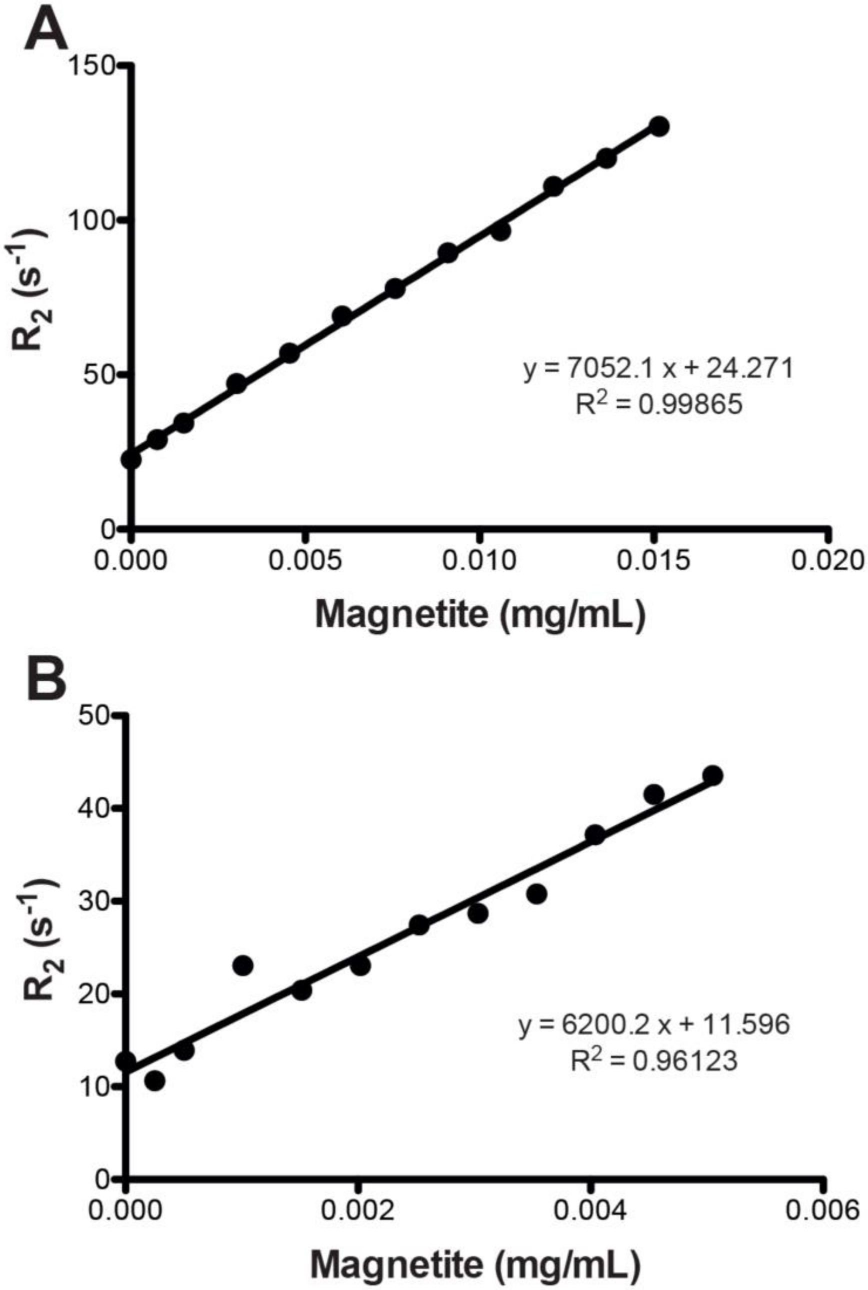
A
150
100
50
0
R_2 (s^{-1})
y = 7052.1 x + 24.271
R^2 = 0.99865
0.000
0.005
0.010
0.015
0.020
Magnetite (mg/mL)
B
50
40
30
20
10
0
R_2 (s^{-1})
y = 6200.2 x + 11.596
R^2 = 0.96123
0.000
0.002
0.004
0.006
Magnetite (mg/mL)

FIGURE 6 CONCENTRATION DEPENDENCE OF RELAXIVITY OF SMART

Concentration dependence of relaxivity (r_2) of SMART in (A) PBS and (B) MDM. MDM were incubated with 100 µM SMART (based on ATV content) for 24 hours. Collected MDM and SMART were suspended in 1% agar gel. T_2 was measured by MRI and magnetite content by ICP-MS

3. Chapter III SMART: MRI-assayed drug and magnetite biodistribution

3.1. Abstract

The feasibility of imaging SMART biodistribution in vivo using MRI was investigated in this chapter. In this proof-of-concept study, the jugular vein was used for the intravenous injections of SMART and ensures uniform drug and magnetite distribution, minimizes standard deviation within groups and provides rapid particle distribution. The relationship between magnetite concentration and ATV concentration in different organs in different time points was evaluated. We demonstrated reduction of T_2* caused by magnetite's presence in tissues correlates with the drug content.

The magnetite concentration was quantified from the change in T_2 weighted relaxivity (ΔR_2 = $1/T_{2preinjection}$ - $1/T_{2postinjection}$) and the per milligram magnetite relaxivity (r2) determined as the slope of magnetite concentration versus R_2 in phantom studies. ATV concentrations was quantified by ultra performance liquid chromatography tandem mass spectrometry (UPLC-MS/MS) following the MRI scan.

Our immunohistochemical analysis further demonstrates that SMART particles are taken up by liver and spleen macrophages. These cells serve as the reservoir of SMART particles, as well as the major targets of HIV. The advantages of using SMART rests as a cassette system for testing nanoparticles that direct nanoART to tissue viral reservoirs.

3.2. Introduction

The visualization of cellular function in living organisms is not a new modality (139, 140). Optical, X-ray, nuclear, MRI and ultrasound allows three-dimensional whole-body scans at high spatial resolution and are adept at morphological and functional evaluations. The data obtained can be enhanced by magnetite and improved image resolution. By immobilizing a specific target molecule on the surface of a magnetic particle, the molecule inherits its magnetic property. Magnetic tissue targeting using multifunctional carrier particles can also facilitate effective treatments by enabling site-directed therapeutic outcomes.

Our current work sought to use lipid coated PLGA SMART to encase magnetite and antiretroviral therapy to facilitate MDM uptake of drug and its subsequent slow release. In the last chapter we discussed the synthesis of SMART to facilitate drug screening for specific targeting ligands or sugars. In this chapter we are going to study the biodistribution of SMART and correlation between drug and magnetite concentration. A summary cartoon of the experiment scheme can be seen in Figure 7. We also stained the paraffin embedded tissue with Iba-1 antibody to label macrophages and Prussian blue to reveal iron in liver and spleen.

3.3. Experimental Procedures

3.3.1. SMART biodistribution

Biodistribution of SMART particles was determined in male Balb/cJ mice (Jackson Labs, Bar Harbor, ME). SMART particles at a dose of 30 mg/kg ATV were injected via a jugular vein cannula in a total volume of 100 μl for each mouse. The mice were scanned two hours before injection then continuously at 0.25, 1, 2 and 4 hours or at 24 hours after SMART administration. Tissues were collected following the final MRI scan. Tissue drug levels were quantitated by UPLC-MS/MS (141) and magnetite levels were determined by ICP-MS as previously described (134).

3.3.2. MRI acquisition

MRI was acquired using a 7T/16cm Bruker (Ettlingen, Germany) Pharmascan MRI/MRS scanner and a commercial mouse body resonator. SMART detection by MRI was done using T_2 mapping for quantitation and T_2^* weighted high resolution imaging for detection of biodistribution throughout the body. The sequence used for T_2 mapping was a Carr-Purcell-Meiboom-Gill (CPMG) phase cycled multislice multiecho sequence. Forty-one 0.5 mm thick contiguous interleaved coronal images were acquired with an acquisition matrix of 256 x 192, 40 mm field of view, 12 echoes at 10 ms first echo time and 10 ms echo spacing, repetition time of 4680 ms, three averages, for a total acquisition time of 30 min. T_2^* weighted MRI was acquired using a 3D spoiled gradient recalled echo sequence with echo time = 3 ms, repetition time = 10 ms, 15 degree pulse angle, 50 x 40 x 30 mm FOV, 256 x 196 x 128 acquisition matrix, six averages, for a total scan time of 25min.

3.3.3. MRI analyses

T_2 maps were reconstructed using custom programs written in Interactive Data Language (IDL; Exelis Visual Information Solutions, McLean, VA). Preinjection and 24 hour postinjection maps were constructed using the even-echo images from the CPMG phase cycled imaging data set. Mean tissue T_2 was determined using region of interest (ROI) analyses before and after SMART injection for the 24 hour results. Magnetite concentration was then determined from the change in relaxivity ($\Delta R_2 = 1/T_{2preinjection} - 1/T_{2postinjection}$) and the per milligram magnetite of SMART particle relaxivity (r_2) determined as the slope of magnetite concentration versus R_2 in phantom studies.

Acute (0-4 hour) data were acquired with in-magnet jugular vein injection, allowing sequential T_2 mapping to be acquired with a T_2^* weighted fast low angle shot (FLASH) image acquired at the end of a four-hour period. The natural coregistration of these data allowed development of magnetite concentration maps based on relaxivity changes using custom programs written in IDL for the acute scanning session. The ROI analyses were performed using ImageJ (http://imagej.nih.gov/lj) software. For analysis of the acute study, the windows synchronize option was used to simultaneously draw ROIs at same locations on all concentration maps at different time points.

3.3.4. Immunohistochemical identification of cell-SMART uptake

To determine cell localization of SMART spleen and liver were collected after the final MRI scan and fixed in 10% neutral buffered formalin. Tissues were paraffin embedded and sectioned at 5 µm. To identify macrophages, sections were incubated with antibody to ionized calcium binding adaptor molecule 1 (Iba-1, Wako Chemicals USA, Inc., Richmond, VA). The polymer-based HRP-conjugated anti-mouse and anti-rabbit Dako EnVision were used as secondary detection reagents and color developed with 3,3'-diaminobenzidine (DAB). All paraffin-embedded sections were stained with Prussian blue to identify magnetite content. Slides were imaged using a Nuance light microscopy system for brightfield imaging.

3.4. Results

3.4.1. Real time SMART biodistribution and pharmacokinetics

Magnetite labeling allowed the distribution of SMART particles to be quantified over time in live animals (Figure 8). Figure 8A shows examples of magnetite concentration from magnetite in SMART, constructed from MRI T_2 maps measured before and continuously every 30 minutes for four hours after SMART injection. ROI analyses of these data from six animals are shown in Figure 8B. A significant amount of the SMART is still within the vasculature, largely leading to the intensity in the kidney, as kidney shows very little uptake by 24 hours. This reflects the measured concentration in kidney reducing over the first four hours while in liver and spleen, organs where SMART accumulates, the mean signal is relatively constant or increases as the particles redistribute from the blood to the tissue. Significant accumulation of SMART was found in liver and spleen at 4 hours as can be appreciated in Figure 9.

Figure 9 displays two of the 0.128 mm thick T_2* weighted high-resolution 3D FLASH images of the same mouse before and 4 hours after injection of SMART. Presence of magnetite in tissue causes a reduction of T_2* to the point of complete signal loss at TE = 3 ms in the liver, spleen, and some abdominal regions. This method is not quantitative, however it does allow ready identification of the presence of magnetite throughout the body, which can be used to guide quantitative ROI analyses using T_2 maps.

3.4.2. Correlation between magnetite and drug tissue content

Figure 10 shows the relationship between magnetite concentration and ATV concentration of liver, spleen and kidney in four animals 24 hours after injection. It can be appreciated that there is a significant positive correlation (Pearson Correlation, r=0.786, p=0.0008). These results demonstrate the capability of MRI to be used for monitoring nanoART distribution.

3.4.3. Identification of magnetite-ART relationships in systemic tissues

We reasoned that cellular biodistribution of SMART was concordant with our prior results with nanoART (142). To prove this theory we next studied the relationships between SMART particle biodistribution and macrophages in mice following parenteral SMART injections. Animals were sacrificed 24 hours after injection and tissues were collected. Dual Iba-1 for macrophages and Prussian blue staining for magnetite were performed and evaluated by bright field microscopic imaging. Prussian blue staining was nearly exclusively in tissue cells identified as macrophages in liver. Spleen from mice without SMART treatment showed Prussian blue staining but staining increased when compared with mice received SMART treatment. As shown in Figure 11, Iba-1 positive macrophages were readily seen in both liver and spleen in parallel to distribution of Prussian blue. The dual staining pictures showed that the SMART particles were retained in tissue macrophages.

3.5. Discussion

The overarching idea of this chapter is to use SMART as a cassette system for testing ligands conjugated to particles for improved targeting of viral reservoirs such as the lymph nodes and brain. To this end, we selected DSPC and DSPE-PEG2k as the shell and PLGA as the core of SMART system. DSPC is used to increase the biocompatibility of SMART, and DSPE-PEG2k is used to build a sterically repulsive shield around SMART that reduces opsonization, prevents interactions with the MPS, escape renal exclusion, and increases systemic circulation. To the best of our knowledge, this is the first attempt to develop lipid-coated PLGA nanoparticles for HIV therapeutics.

After pre-scan, mice were scanned by MRI continuously at 30 minute intervals up to 4 hours after SMART administration. Magnetite levels in kidney, spleen and liver were similar in the first half hour due to the magnetite is still circulating in the blood stream following SMART administration (Figure 8B). Yet as magnetite started to distribute over time, a higher amount stayed in liver and spleen after 4 hours of injection, correlated with higher concentration of magnetite in these organs at 24 hours as shown by the MRI scans. Our in vivo MRI results also showed that the concentrations of magnetite and ATV in mouse tissues, such as liver, spleen and kidney, correlate with one another at 24 h after injection.

The results support the idea that SMART technology facilitates the noninvasive evaluation of drug PK and biodistribution in virus target tissues by MRI. These results demonstrate the capability of MRI to be used for monitoring ATV distribution by tracking the presence of magnetite in tissue, which causes a reduction of T_2*. Our in vivo MRI results clearly demonstrated that SMART could facilitate the noninvasive evaluation of drug PK and biodistribution in different tissues and provide rapid assessments for the next generation cell and tissue ligand decorated particles.

Erythrocyte hemoglobin and its breakdown products are a substantive source of iron. These are degraded after the lifespan of the erythrocyte (143). This occurs predominantly in the spleen with iron transferred back into the blood. The highly vascularized spleen contains easily seen red blood cell breakdown products including iron that are phagocytized by macrophages (144). Thus, the total iron content in the spleen is readily visualized by Prussian blue staining but substantively increased after SMART treatments (Figure 11 G and H). The iron content in spleen also changed from 228 µg/g before treatment to 356 µg/g after treatment, measured by ICP-MS.

Notably, there is a considerable focus amongst HIV/AIDS researchers towards the development of reliable methods to bring drugs to reservoir sites with the explicit goal of eliminating virus. Targeted drug when combined with suitable imaging techniques like

SMART particles could facilitate this goal by providing a “go/no go” for treatment success. This technology clearly opens new opportunities to develop platforms that would accelerate elimination of viral infections.

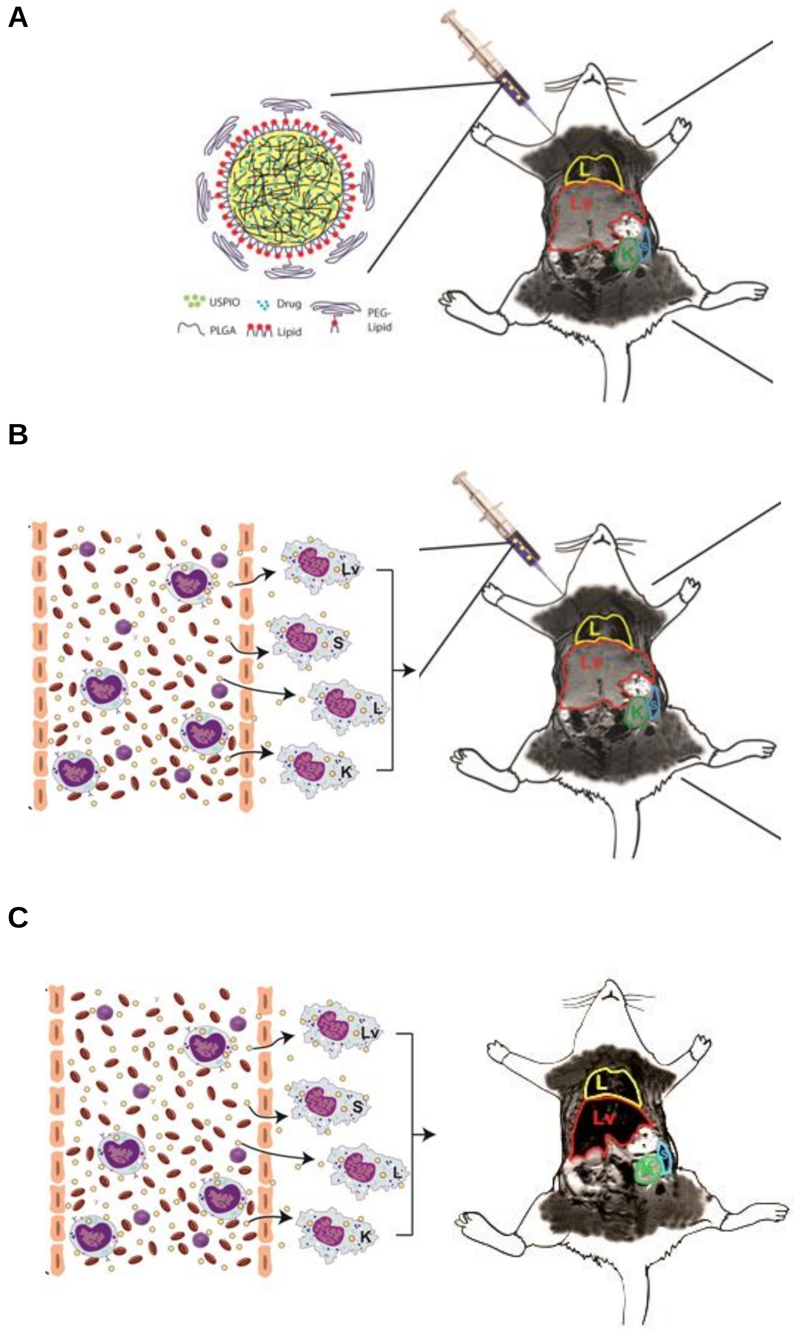
A
USPIO
Drug
PLGA
Lipid
PEG-
Lipid
L
Lv
S
K
B
Lv
S
L
K
L
Lv
S
K
C
Lv
S
L
K
L
Lv
S
K

Figure 7 Cartoons of SMART injection and biodistribution

(A) MRI of mice were obtained and SMART was injected to mice through jugular vein. (B) SMART was taken up by MDM in vivo. (C) 24 hours later, MRI of mice were obtained.

A

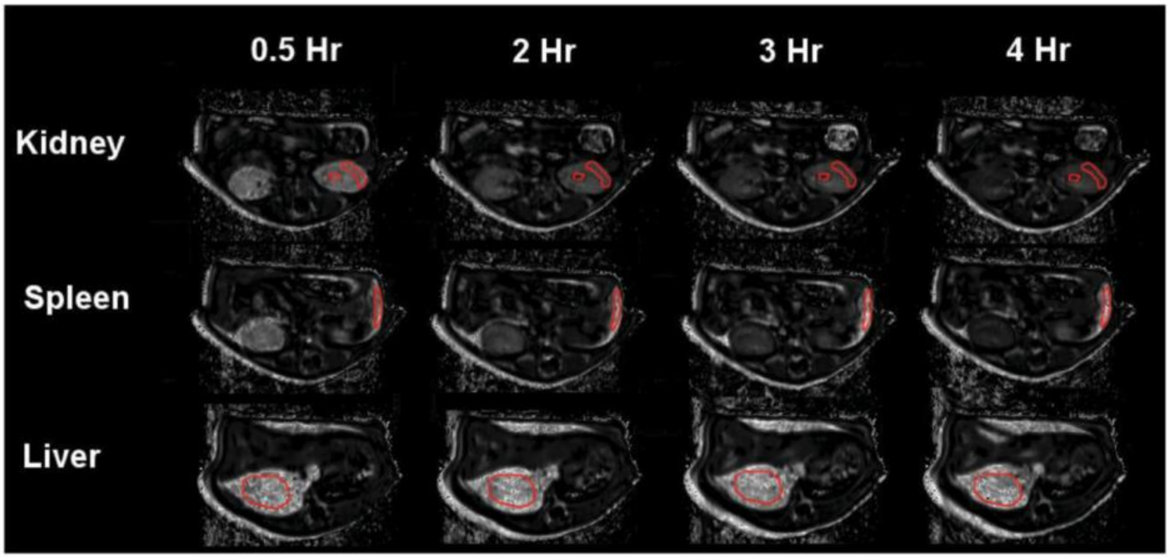

B

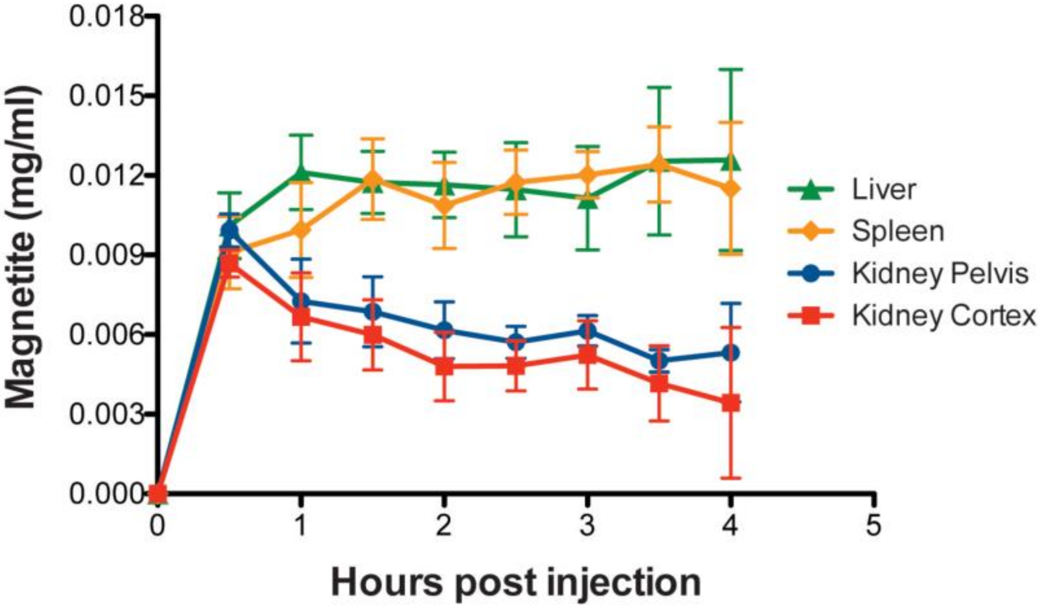
0.018
0.015
0.012
0.009
0.006
0.003
0.000
Magnetite (mg/ml)
0
1
2
3
4
5
Hours post injection
Liver
Spleen
Kidney Pelvis
Kidney Cortex

FIGURE 8 MRI ASSESSMENTS OF THE TISSUE DRUG BIODISTRIBUTION AND PHARMACOKINETICS BY SMART PARTICLES

MRI assessments of the tissue drug biodistribution and pharmacokinetics by SMART particles. After pre-MRI scan, mice were injected with SMART through a jugular vein cannula, and then scanned by MRI at continuously at 30 minute intervals up to 4 hours after SMART administration. Mean tissue SMART content was determined as detailed in Materials and Methods. Immediately after the final scan, mice were euthanized and tissues were collected for ATV quantification by UPLC-MS/MS. (A) MRI based images of magnetite concentration in kidney, spleen and liver from 0.5 h to 4 h following SMART administration. (B) Mean ± SEM (n=6) of magnetite levels in kidney, spleen and liver over 4h following SMART administration.

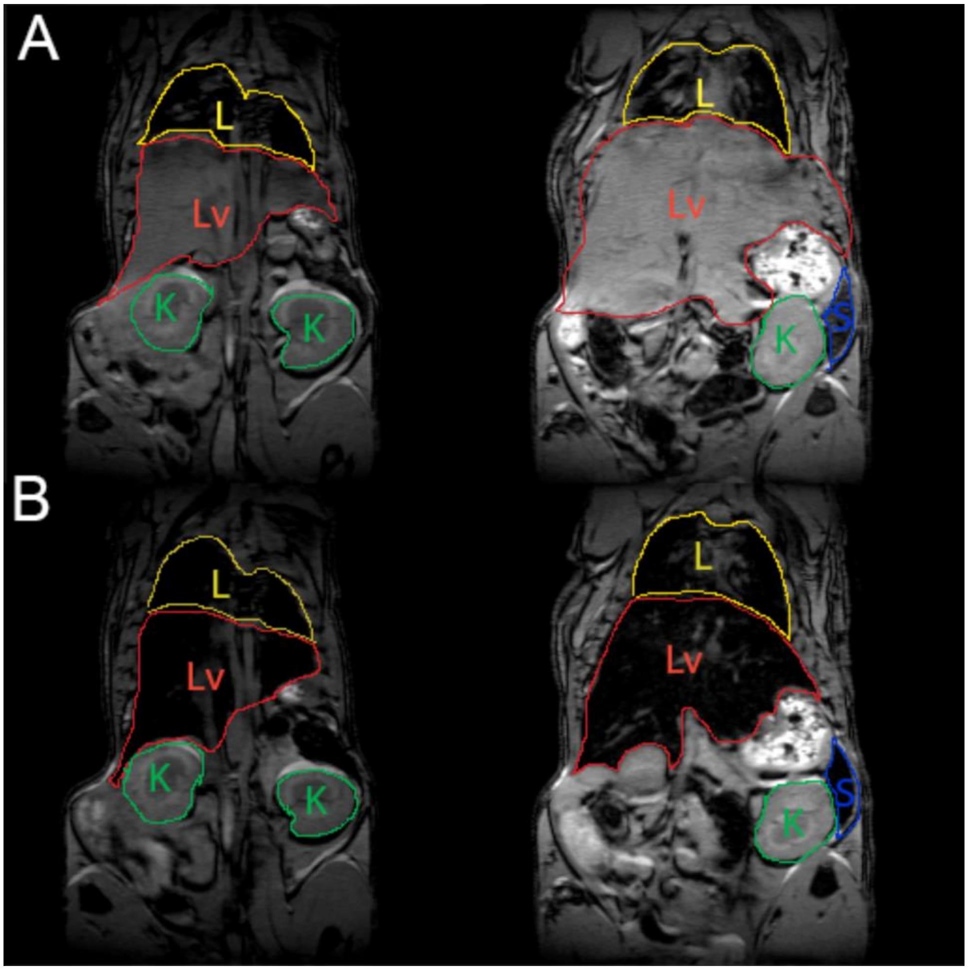
A
L
Lv
K
K
L
Lv
K
S
B
L
Lv
K
K
L
Lv
K
S

FIGURE 9 3D GRADIENT RECALLED ECHO IMAGES OF THE SAME MOUSE BEFORE AND AFTER INJECTION OF SMART

3D gradient recalled echo images of the same mouse before (A) and 4 hours after (B) injection of SMART. It can be appreciated that the signal from the liver is completely eliminated due to the accumulation of magnetite loaded SMART (L=lung, Lv=liver, K=kidney and S=spleen).

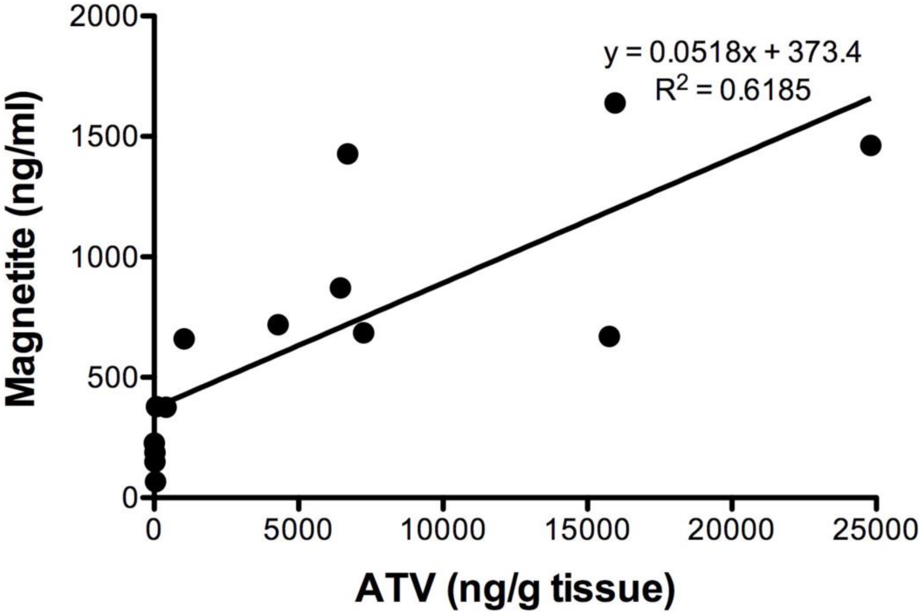
y = 0.0518x + 373.4
R^2 = 0.6185
Magnetite (ng/ml)
2000
1500
1000
500
0
0
5000
10000
15000
20000
25000
ATV (ng/g tissue)

FIGURE 10 CORRELATION OF SMART-ASSOCIATED MAGNETITE AND ATV IN TISSUES 24 HOURS AFTER ADMINISTRATION

The magnetite concentration was quantified from the change in T_2 weighted relaxivity ($\Delta R_2 = 1/T_{2preinjection} - 1/T_{2postinjection}$) and the per milligram magnetite relaxivity (r_2) determined as the slope of magnetite concentration versus R_2 in SMART phantom studies. ATV concentrations were quantified by UPLC-MS/MS following the final 24 hour MRI scan.

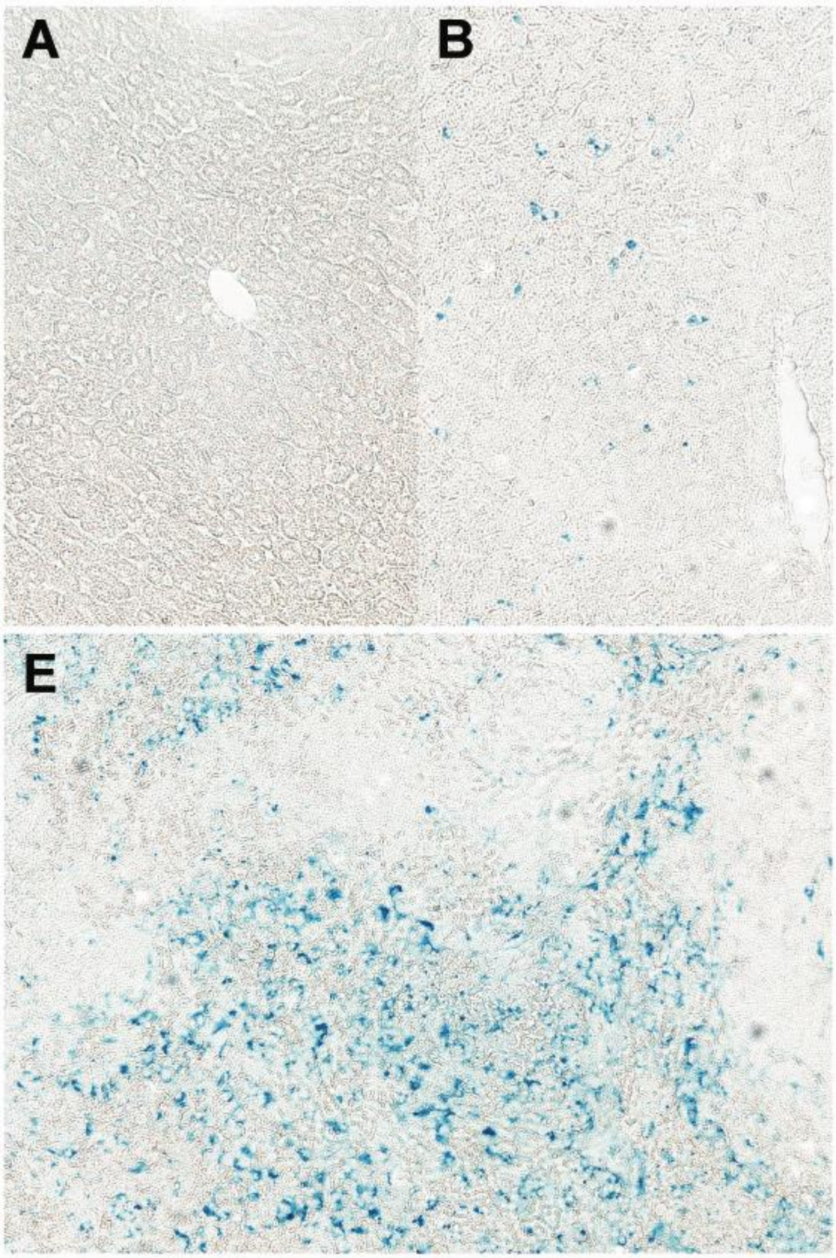
A
B
E

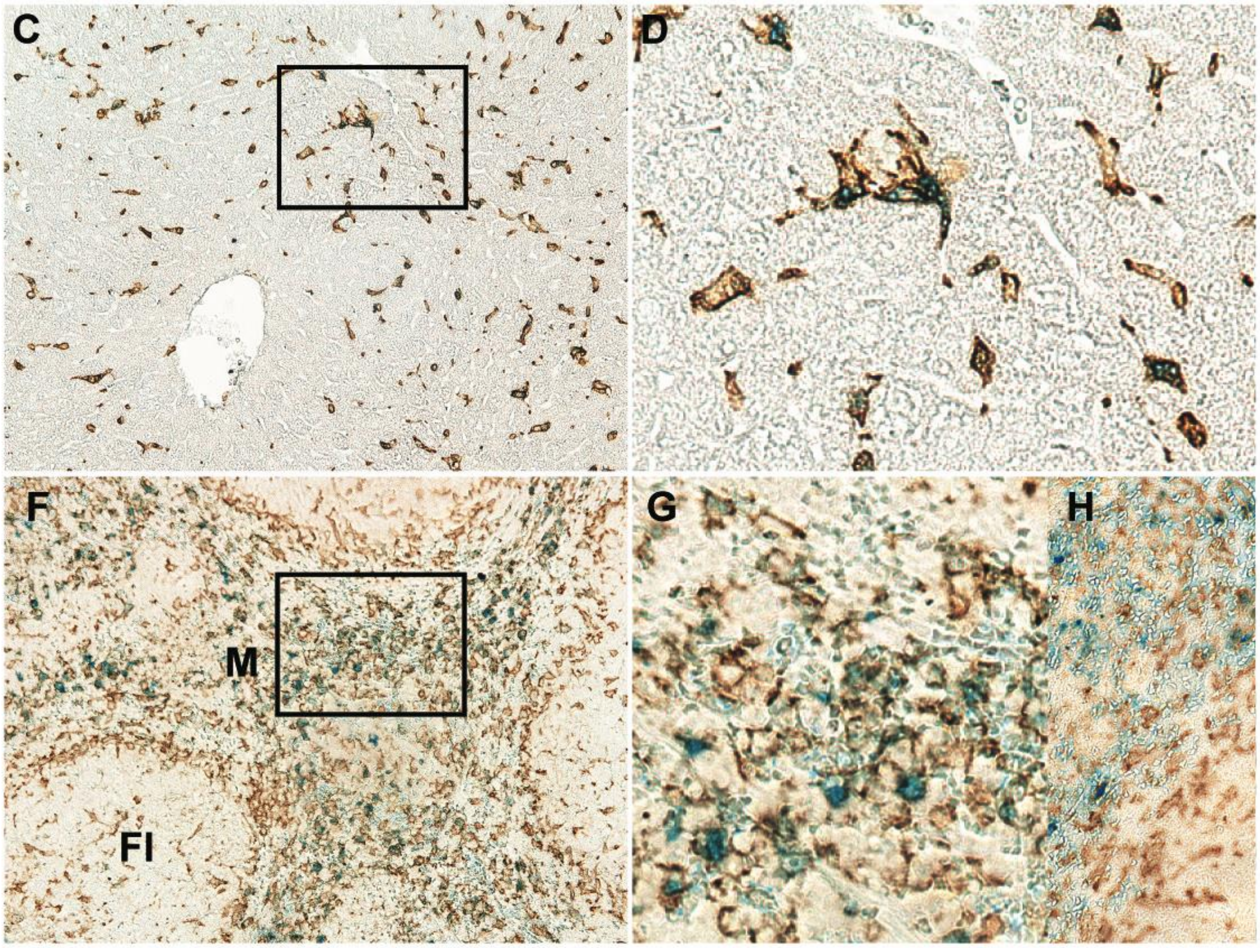
C
D
F
M
FI
G
H

FIGURE 11 IMMUNOHISTOLOGY OF IBA-1 STAINING AND PRUSSIAN BLUE STAINING

Immunohistology of Iba-1 staining and Prussian blue staining of (A) Liver from control mice with Prussian blue (200×). (B) Liver from SMART treated mice with Prussian blue (200×). (C) Liver from SMART treated mice with Prussian blue and Iba-1 (200×). (D) Enlargement from indicated section in C. (E) Spleen from SMART treated mice with Prussian blue (200×). (F) Spleen from SMART treated mice with Prussian blue and Iba-1 (200×). (G) Enlargement from indicated section in F. (H) Spleen from control mice with Prussian blue and Iba-1 (400×). Livers and spleens were fixed with 10% formalin, paraffin embedded and sectioned for immunohistological analysis after the final MRI scan. Macrophages were identified by Iba1 stains (brown) and magnetite identified by Prussian blue. Fl=lymphoid follicle, M=marginal zone.

4. Chapter IV APM and FAPM manufacture and characterization

4.1. Abstract

Dextran-based SPIO nanoparticles have been extensively used clinically as MRI contrast agents. These dextran-based SPIO nanoparticles are taken up by phagocytic cells and accumulate in the reticuloendothelial system. These nanoparticles can be utilized for multifunctional biomedical applications with simultaneous drug-delivery and imaging capabilities. However, dextran coating is not strongly associated with SPIO nanoparticles and can be readily detached, leading to SPIO aggregation and precipitation under physiological conditions (145). Also, the lack of functional groups on the surface of PLGA nanoparticles for covalent modification has limited their potential for surface tethering targeting ligands (146). Additionally, these dextran-based SPIO nanoparticles are limited in their capacity of drug loading and the drug dissociates rapidly after administration intravenously (147).

In this study, we describe the development of single magnetite nanoparticles with strong polymer coating for MRI. The developed nanoparticles are composed of a hydrophobic 10 nm magnetite core and a PEG coating, anchored with a bisphosphate drug, Alendronate (ALN). The study was designed to investigate the characteristics and biodistribution of the developed SPIO. Size, shape, charge, morphology, relaxivity and stability of ALN-PEG coated magnetite (APM) and ALN-PEG-folate coated magnetite (FAPM) were evaluated.

4.2. Introduction

Significant reductions of residual HIV from its cell and tissue reservoirs in brain, lymphoid tissues, bone marrow, gastrointestinal and the genital tracts can be achieved by chemical or immunological means. One way to achieve this goal is through viral reservoir-targeted long-acting antiretroviral nanoparticles by monocyte-macrophage drug targeting (148). To facilitate such an end, a number of ligands for macrophage targeting are being developed and include peptides (68), antibodies (87), proteins and sugars (78) that make use of cell-specific receptor expression or by enabling phagocytosis. An additional hurdle towards achieving this goal is the dearth of ways to measure ART distribution outside of plasma drug levels (118).

In particular pharmacokinetic and pharmacodynamics studies have recently demonstrated the benefit of such targeting strategies; although assessments of such drug biodistribution improvements have entailed intensive tissue analyses (149). We posit that such processes can be improved further by targeting ligand testing of linked magnetic nanoparticles and parallel MRI evaluation of particle distribution. Moreover, we theorize that such results would closely mimic drug tissue biodistribution.

Prior magnetite platforms have been developed for this purpose (150-152). Among them, polysaccharides are the most widely studied coating materials for magnetite (153-155). However, the potential *in vivo* coating disassociation and bare magnetic particle exposure causing cellular toxicity are of significant concern (156). Another limitation of current coating materials for magnetite is the complicated conjugation strategies or limited appreciated functional groups for specific ligand decoration in magnetite. Substantive efforts have been made to resolve these issues. ALN is a bisphosphonate drug, which is clinically used to treat osteoporosis. The P-C-P structure of bisphosphonates is known for its ability to bind divalent metal ions, such as Ca^{2+} (157).

Taking advantages of this metal binding ability, we successfully conjugated ALN into polymers for stable magnetic particle coating. FA is a targeting ligand of FR, which expression is restricted to few cell types including macrophages. FA was successfully decorated to the exterior coating of magnetite to allow comparisons of magnetite biodistribution with and without targeting.

4.3. Experimental Procedures

4.3.1. Synthesis of magnetite

The magnetite particles were synthesized as follows: 6 mmol tris(acetylacetonato) iron(III) was mixed with 30 mmol 1,2-hexadecanediol, 18 mmol oleic acid, 18 mmol olylamine and 60 ml benzyl ether in a three-neck round-bottomed flask equipped with condenser, magnetic stirrer, thermograph and heating mantle and stirred under nitrogen. The mixture was slowly heated to 110^{o}C and kept at that temperature for 1 hour, then gradually heated to 200^{o}C. Reflux was kept after it reached 200^{o}C for 2 hours, then slowly heated to 298^{o}C and kept at reflux for another 1.5 hours. After cooling to room temperature, a dark homogeneous colloidal suspension was obtained. The suspension was precipitated in ethanol with a magnetic field. The black precipitate was dissolved in hexane with the presence of oleic acid and oleylamine and the solution was centrifuged at 3,800 x g for 10 min to remove any undispersed residue. The black solution was re-precipitated in ethanol and centrifuged at 10,000 x g for 30 min. Solid products were obtained by drying the precipitate under vacuum, generating the final dry particles.

4.3.2. Synthesis of alendronate conjugated polyethylene glycol (ALN-PEG)

Polyethylene glycol monomethyl ether 5,000 (mPEG5k) (1 g, 0.2 mmol) was dissolved in anhydrous dichloromethane (5 mL) together with 4-dimethylaminopyridine (12 mg, 0.1 mmol) and triethylamine (101 mg, 1 mmol). The mixture was cooled to 0°C, and p-toluenesulfonyl chloride (Tos-Cl) (0.191 g, 1 mmol) was added. Next, the mixture was incubated overnight at room temperature and the mixture precipitated in ether. The precipitate (crude product) was purified using a LH-20 column with methanol as the eluent. The yield of p-toluenesulfonyl-terminated mPEG5k (Tos-PEG) was 65%. Tos-PEG (0.52 g, 0.1 mmol) was dissolved in dimethylformamide (5 mL). Sodium azide (65 mg, 1 mmol) was then added. The reaction proceeded with stirring at 100°C for 1 day. After filtration and solvent removal, the crude product was dissolved in dichloromethane and precipitated into ether. The precipitate (crude product) was further purified using a LH-20 column with methanol as the eluent. The yield of azide-terminated PEG5k (azido-PEG) was 70%.

Azido-PEG (0.25 g, 0.05 mmol) and 1-hydroxy-4-pent-4-ynamidobutane-1, 1-diyldiphosphonic acid (40 mg, 0.1 mmol) were dissolved in an ethanol-H2O solution (1/1 v/v, 2 mL). Sodium ascorbate (19.8 g, 0.1 mmol) and copper sulfide pentahydrate (2.5 mg, 10 μmol) were then added separately under argon. The reaction mixture was stirred for 3 days at room temperature. After removal of the solvent, the crude product was acidified and purified using a LH-20 column with methanol as the eluent. The yield of the ALN conjugated polyethylene glycol (ALN-PEG) was 70%.

4.3.3. Synthesis of FA conjugated ALN-PEG (ALN-PEG-FA)

Alendronate sodium trihydrate (1g, 3 mmol) was dissolved into 5 ml water, the pH was adjusted to around 8.0 with NaOH, Fmoc-PEG5k-N-hydroxysuccinimide (NHS) (0.5 g, ~ 1 mmol) was then slowly added into ALN solution. The reaction solution was stirred overnight at room temperature, and then dialyzed to remove excess ALN. After lyophilization, the resulting ALN-PEG-Fmoc powder (0.35 g) was directly dissolved in 20% piperidine in THF and reacted at room temperature for 2 hours to deprotect Fmoc. The solvent was concentrated using rotavapor under vacuum, and precipitated into ether. The resulting precipitate (ALN-PEG-NH2) was further purified with dialysis and lyophilization.

FA (110 mg, 0.25 mmol) was dissolved in 2 ml DMSO plus 50 ul of triethylamine. A 1.1 molar ratio of NHS (31 mg) and N,N’-dicyclohexylcarbodiimide (DCC; 57 mg) was added. The mixture was stirred 4 hours at room temperature in the dark. The by-product, dicyclohexylurea, was removed by filtration. ALN-PEG-NH2 (0.25 g) was then added into the NHS-folate solution for overnight conjugation at room temperature in the dark. The crude product was precipitated with diethylether, and further purified by dialysis.

CF633-NHS (1umol) and ALN-PEG-NH2 (10 mg) were dissolved in 0.5 ml dimethylsulfoxide (DMSO), and then reacted overnight in dark at room temperature. The resulting CF633-labeled ALN-PEG was purified using a LH-20 column with methanol as the eluent.

4.3.4. Coating of ALN-PEG and ALN-PEG-FA onto magnetite (APM and FAPM)

To synthesize APM, various amount of ALN-PEG polymer (5, 10, 20, 50 mg) was dissolved in 0.5 ml deionized water separately; 5 mg magnetite was dissolved in 10 ml

THF. Polymer solution was added slowly to magnetite THF dispersion with stirring. The mixture was stirred overnight, and then THF was removed using rotary evaporator. The crude product was dissolved in 5 ml deionized water, and then centrifuged at 500 x g for 10 min to remove uncoated magnetite. Non-coated polymer was removed by dialysis using 25k dialysis tubing overnight. After dialysis, the dispersion was lyophilized to obtain APM. The mass ratios between magnetite and coating materials were measured using thermal gravimetric analysis (TGA).

To synthesize FAPM, 16 mg ALN-PEG polymer and 4 mg ALN-PEG-Folate were dissolved in 0.5 ml deionized water and 5 mg magnetite was dispersed in 10 ml THF. Polymer solution was added slowly to the magnetite THF dispersion with stirring in the dark. The mixture was stirred overnight, and then THF was removed using a rotary evaporator. The crude product was dissolved in 5 ml deionized water, and then centrifuged at 500 x g for 10 min to remove uncoated magnetite. Non-coated polymers were removed by dialysis using 25k dialysis tubing overnight in dark. After dialysis the dispersion was lyophilized to get FAPM powder.

CF633-labeled APM and FAPM were synthesized using the same procedure with 2 mg CF633-labeled ALN-PEG dissolved in the polymer solution.

4.3.5. Physicochemical and stability characterization of APM and FAPM

Particles size and size distribution were measured by DLS using a Malvern Zetasizer Nano-ZS instrument (Malvern Instruments Inc., Westborough, MA, USA). The pH value and concentration of the particles dispersion were fixed before measurements of particles size and size distribution. All measurements were performed at 25°C. The shape and surface morphology of the APM and FAPM particles were investigated by TEM performed as previously described (158). Samples were prepared from dilutions in distilled water of particle suspensions and dropped onto stubs. After air-drying the particles were then examined by TEM. The stability of APM was studied in NaCl solutions (1M and 2M) and buffer solutions with pH 2, 4, 6, 7.4, 8, 10, 12 that were determined by DLS and TEM. Concentration dependent relaxivity (r_2 s^{-1} ml mg^{-1}) was measured by MRI of APM or FAPM dispersion in concentrations ranging from 0 µg/ml to 40 µg/ml.

4.3.6. Statistical analyses

The data are presented as mean ± SEM. Statistical significance between groups was assessed using Student’s t-test by Graph-Pad® Prism unless specified. The data were considered statistically significant if P<0.05.

4.4. Results

4.4.1. Synthesis of ALN conjugated polyethylene glycol (ALN-PEG) and FA conjugated ALN-PEG (ALN-PEG-FA)

As an initial step towards securing this end, we manufactured ALN-PEG and ALN-PEG-FA polymers. These were synthesized for magnetite coating. In order to efficiently conjugate hydrophilic ALN to PEG polymer, the versatile click reaction was used (Figure 12A).

mPEG was first tosylated with toluenesulfonyl chloride, then converted to azido-mPEG under reflux using excess sodium azide. To introduce an acetylene group onto ALN, N-(3-Dimethylaminopropyl)-N′-ethylcarbodiimide hydrochloride/NHS was used to conjugate ALN and pentynoic acid. Finally, these two fragments were successfully conjugated together through copper (I)-catalyzed Huisgen 1, 3-dipolar cycloaddition between the azide and alkyne with high yield at room temperature. ALN-PEG-FA was synthesized using amidation strategy (Figure 12B). First, ALN was incorporated into PEG by reaction with Fmoc-PEG-NHS, and the Fmoc was then deprotected with piperidine to synthesize amine functionalized ALN-PEG (NH2-PEG-ALN) for ligand conjugation, which is one of the most attractive properties of ALN-PEG polymers. For folate conjugation, NHS-activated folate was reacted with NH2-PEG-ALN to synthesize the targeted ALN-PEG-FA with high yield. From 1H NMR spectrum, emergence of the singlet peak of 1,2,3-triazole at 8.32 ppm verified the successful conjugation of ALN to PEG polymer (Figure 12C)

4.4.2. Manufacture of APM and FAPM

To confirm the strong coating ability of ALN-PEG polymer to magnetite, oleic acid (OA) coated magnetite synthesized by thermal decomposition method with an average size in 10 nm were selected for replacement coating. The OA coating material is hydrophobic and relatively weakly bound to the core of magnetite. OA-coated magnetite was dispersed into THF, then ALN-PEG was added into this solution for replacement coating overnight at room temperature and turned the magnetite from hydrophobic to hydrophilic. At the end of replacement, THF was evaporated and magnetite particles were redispersed in water and dialyzed. After dialysis, the dispersed solution was lyophilized. The structure of APM and FAPM is demonstrated in Figure 13.

Benefitting from its high coating efficacy, ALN-PEG was coated onto magnetite in a programmable and reproducible manner. Up to 100% of the ALN-PEG was coated onto magnetite as measured by TGA (Figure 14C). We chose magnetite with 20% wt magnetite and 80% wt polymer for further evaluation due to its outstanding stability and ability to conjugate sufficient number of ligand molecules.

To demonstrate the potential of APM as one novel nanomedicine platform for targeting ligand evaluation and optimization, FA was selected to conjugate to the ALN-PEG polymer (ALN-PEG-Folate) using amidation strategy (Figure 12Figure 12). For the preparation of folate-decorated magnetite, OA-coated magnetite was dispersed into THF, and then ALN-PEG and ALN-PEG-Folate (weight ratio 4:1) were added into this solution for OA replacement overnight at room temperature. The purification procedures were same to preparation of APM.

4.4.3. Physicochemical and stability characterization of APM and FAPM

The lyophilized particles are easily dispersed in water and the nanoparticles are very stable in biological buffers such as PBS. Under an external magnetic field, APM retained its dispersion stability in PBS while OA-coated magnetite in PBS were colloidally unstable, precipitated, and were attracted towards a magnetic field within minutes (Figure 14A). To study the stability of APM, we tested its size and PDI in acidic, basic and high ironic strength conditions. APM nanoparticles were very stable in various conditions, and there was no significant increase in size and PDI of APM within the 2 weeks' timeframe of the study (Figure 15A). After one month storage on the shelf, APM solutions were clear and no nanoparticles precipitate out (Figure 15B). The TEM pictures of APM nanoparticles also confirmed this result (Figure 15C). After two month storage, all APM solutions remained clear expect APM nanoparticles in NaCl 2M solution precipitated out slightly (Figure 15B), which was easy to form stable dispersion again with gentle shaking.

The structure of FAPM is illustrated in Figure 13B. The size of APM and FAPM nanoparticles was assessed by TEM showing that the iron oxide core is morphologically indistinguishable from each other, with a mean particle size of 10 nm (Figure 14B).

Concentration dependent relaxivity [r_2 (s^{-1} ml mg^{-1})] causing increased relaxivity (R_2 (s^{-1})) in tissue as a function of concentration (expressed as mg/ml magnetite) of APM and FAPM is an important parameter. To investigate the MR signal enhancement effects, the relaxivity of aqueous magnetite particles at different magnetite concentrations was determined using a 7T MRI scanner. The magnetite concentrations in mg/ml were plotted against R_2. As shown in Figure 14D, the relaxivity of both APM and FAPM varied linearly with the magnetite concentration. The relaxivity of FAPM was found to be $r_2 = 582$ (s^{-1} ml mg^{-1}) and of APM $r_2 = 638$ (s^{-1} ml mg^{-1}) (Figure 14D). The r_2 values of these particles were used for noninvasive in vivo quantitation of magnetite concentration using MRI.

CF633-labeled APM and FAPM were synthesized successfully, SPIO coated with CF633 conjugated ALN-PEG polymer, with CF633 conjugated ALN-PEG and ALN-PEG-Folate polymer and with oleic acid visualized by UV light (254 nm) exposure (Figure 16). Only the SPIO with CF633 label showed fluorescence suggesting a successful dye conjugation.

4.5. Discussion

HIV-1 infected memory effector CD4+ T cells and in more limited numbers, tissue macrophages, are targets for persistent low-level infection (56, 159). Both are refractory to immune and chemical elimination and are resistant to virus-associated cytopathicity (56). HIV-1 has evolved mechanisms to prolong the life span of infected cells (57, 58). Virus is present for long periods of time in gut, lymphoid and brain reservoirs thus constituting obstacles for viral eradication within infected individuals (160). One way to reduce residual virus in its reservoirs is by targeted antiretroviral nanotherapy (136, 149, 161). Nonetheless, adequate targeting schemes have not yet been achieved and current methods to develop them are commonly slow and cumbersome. To such ends our own works have centered on ways to bridge classic PK evaluation with MRI assessment of particle distributions (158).

FA has emerged as an important targeting moiety capable of specific interaction with cells expressing the FR. Its expression is restricted to a few cell types, including mononuclear phagocytes lineage and is regulated by cell activation that is initiated by the particle itself. Specific drug targeting can thus parallel tissue sites of infection and consequent inflammation along with the reticuloendothelial system. MP and reticuloendothelial cells would then serve as drug storage depots (136, 137). This, notably, makes FA conjugation specifically for antiretroviral therapeutic nanoparticles of particular benefit for treatment of HIV infection (162).

In this study, FA was successfully conjugated to the ALN-PEG polymer, which has high metal binding affinity. Magnetite with ALN-PEG coating or ALN-PEG and ALN-PEG-Folate coating showed similar size, shape and relaxivity (Figure 15) which demonstrates that conjugation of FA doesn't compromise the stability of the nanoparticle. Relaxivity of both particles had an excellent regression, and the similar result (582 s^{-1} ml mg^{-1} vs 638 s^{-1} ml mg^{-1}) is critical to make the magnetite concentration comparable.

APM demonstrated excellent stability in various buffers (Figure 15A, B, C), no nanoparticles precipitate out after one month storage on the shelf. After 2 months of storage, all APM dispersions remained stable except APM nanoparticles in the 2 M NaCl solution where some precipitation was observed which can be reversed with gentle shaking. The strong binding ability of ALN polymer contribute significantly to the prolonged shelf life.

We have manufactured a single magnetite particle that is easy to conjugate targeting ligands, the other potential targeting ligands includes mannose, antibody and peptides. We posit that the targeting ability of different ligands can be studied further by targeting ligand testing of linked magnetic nanoparticles and parallel MRI evaluation of particle distribution. Moreover, we theorize that such results would closely mimic drug tissue biodistribution with the same targeting ligands.

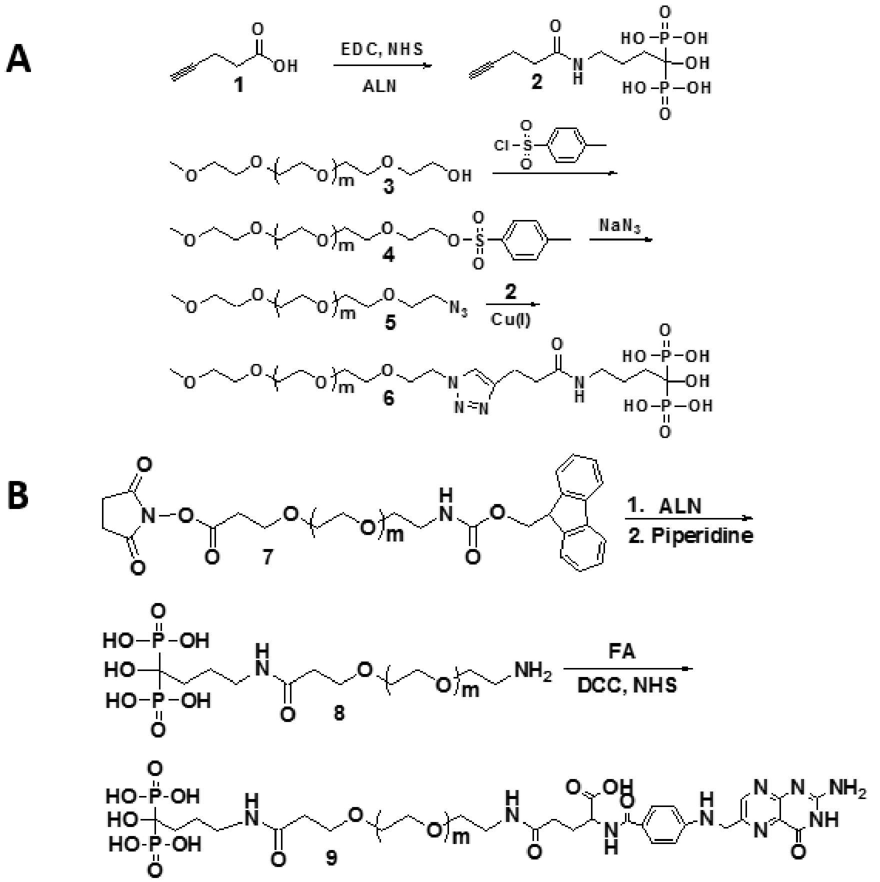
A
1
EDC, NHS
ALN
2
3
4
NaN$_3$
5
2
Cu(I)
6
B
7
1. ALN
2. Piperidine
8
FA
DCC, NHS
9

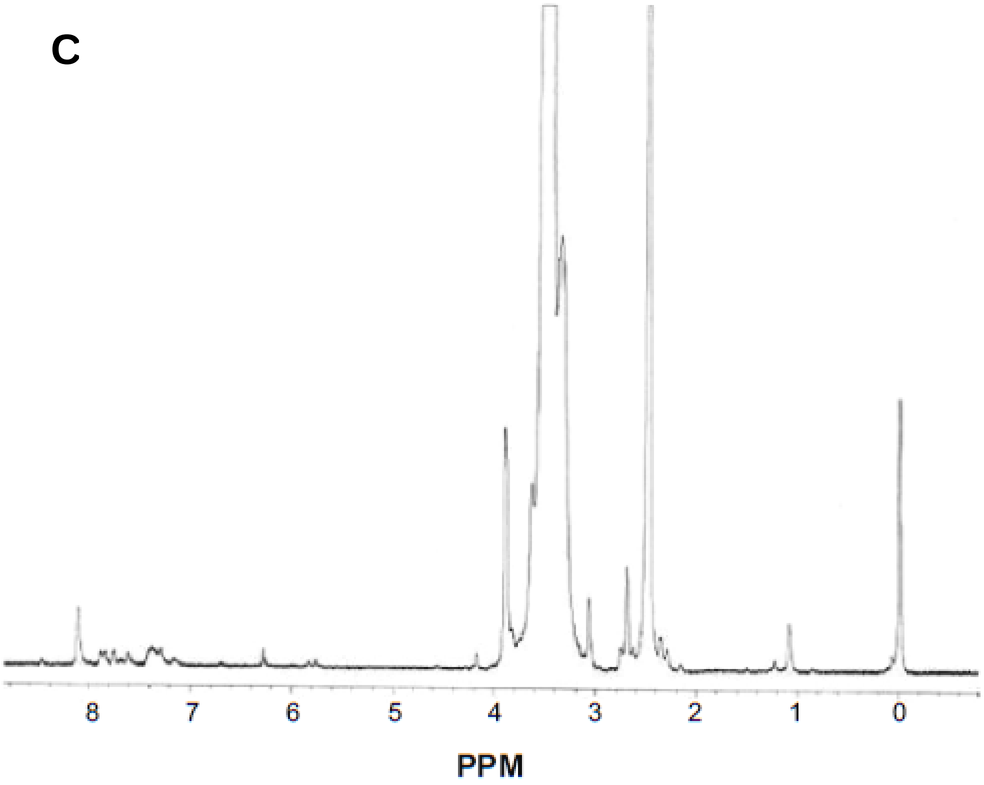
C
8
7
6
5
4
3
2
1
0
PPM

FIGURE 12 ALN-PEG AND ALN-PEG-FOLATE POLYMER SYNTHESIS

(A) Synthesis of ALN-PEG polymer. (B) Synthesis of ALN-PEG-Folate polymer. (C) ^{1}H NMR spectrum of ALN-PEG polymer.

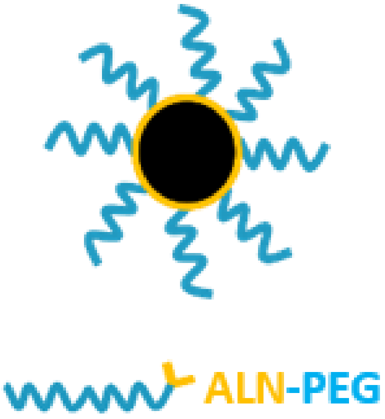

ALN-PEG coated
magnetite (APM)

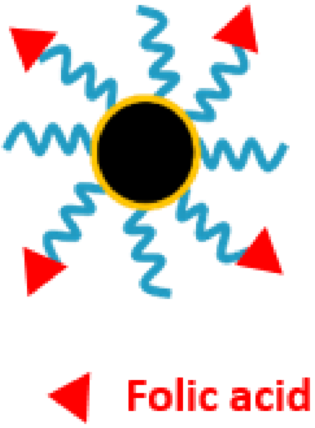

ALN-PEG-folate
magnetite (FAPM)

Figure 13 The schematic structure of APM and FAPM

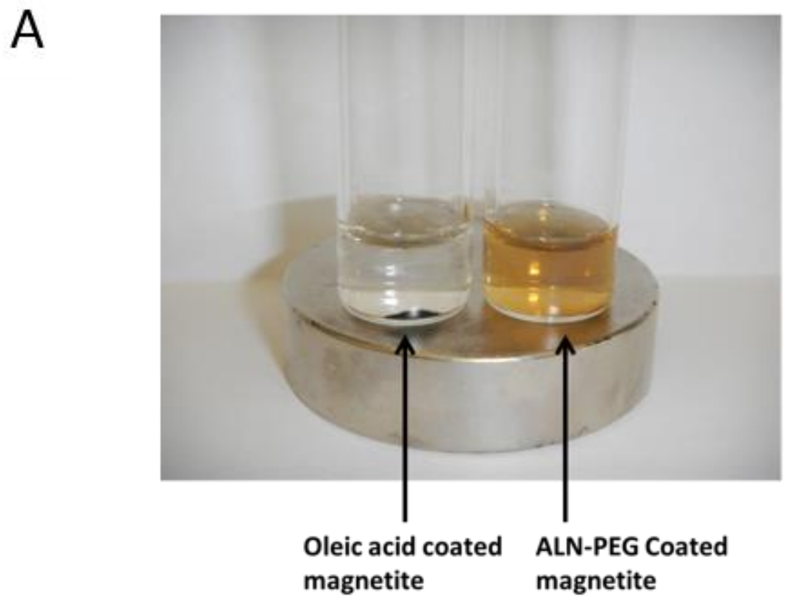
A
Oleic acid coated magnetite
ALN-PEG Coated magnetite

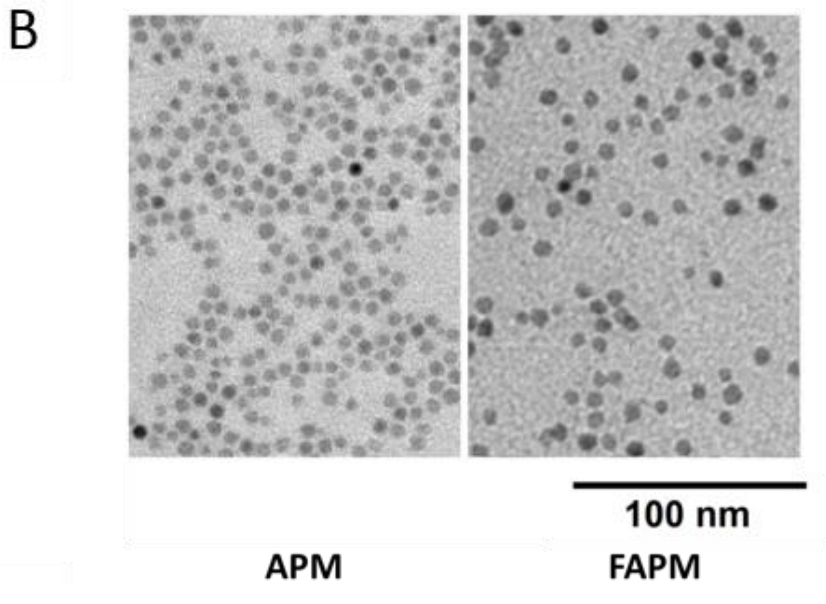
B
100 nm
APM
FAPM

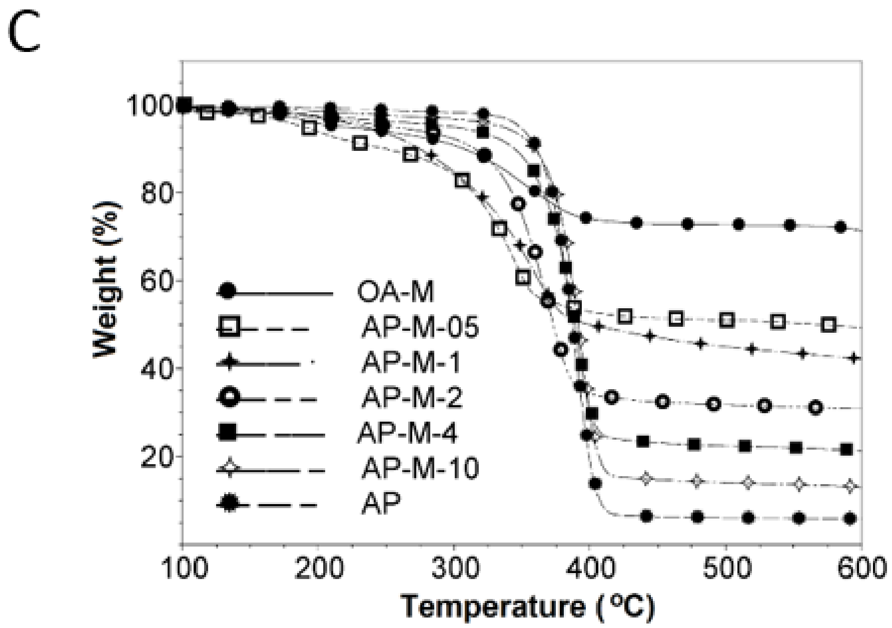
C
Weight (%)
100
80
60
40
20
100
200
300
400
500
600
Temperature (°C)
OA-M
AP-M-05
AP-M-1
AP-M-2
AP-M-4
AP-M-10
AP

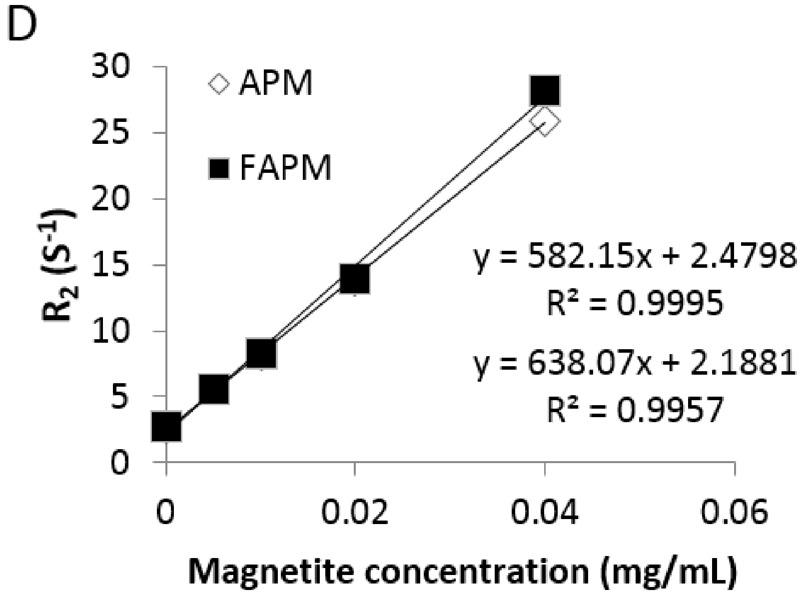
D
APM
FAPM
y = 582.15x + 2.4798
R² = 0.9995
y = 638.07x + 2.1881
R² = 0.9957
R2 (S-1)
30
25
20
15
10
5
0
0
0.02
0.04
0.06
Magnetite concentration (mg/mL)

FIGURE 14 APM AND FAPM CHARACTERIZATION

(A) APM and OA coated magnetite under external magnetic field. (B) TEM of APM and FAPM in PH=7.4 solution. (C) TGA analysis of magnetite with various polymer coatings. (D) Relaxivity of APM and FAPM.

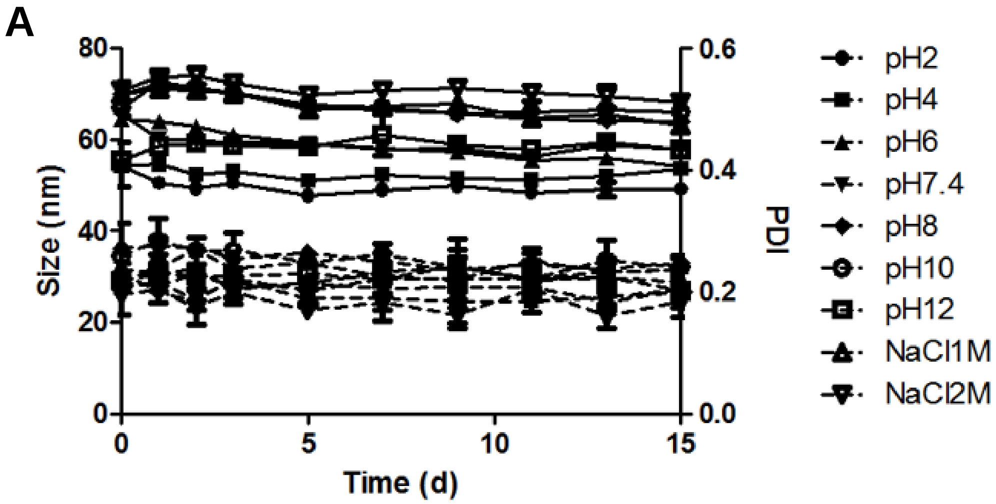
A
Size (nm)
PDI
Time (d)
0
20
40
60
80
0.0
0.2
0.4
0.6
0
5
10
15
pH2
pH4
pH6
pH7.4
pH8
pH10
pH12
NaCl1M
NaCl2M

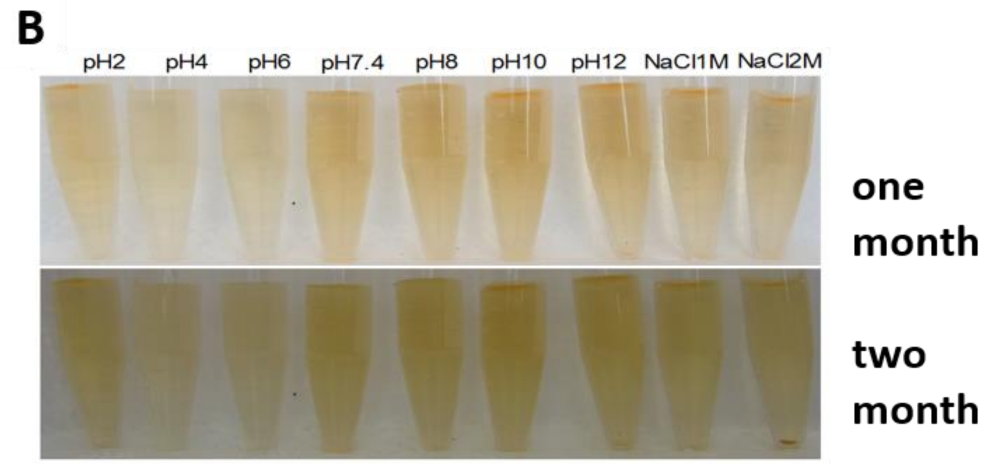
B
pH2
pH4
pH6
pH7.4
pH8
pH10
pH12
NaCl1M
NaCl2M
one month
two month

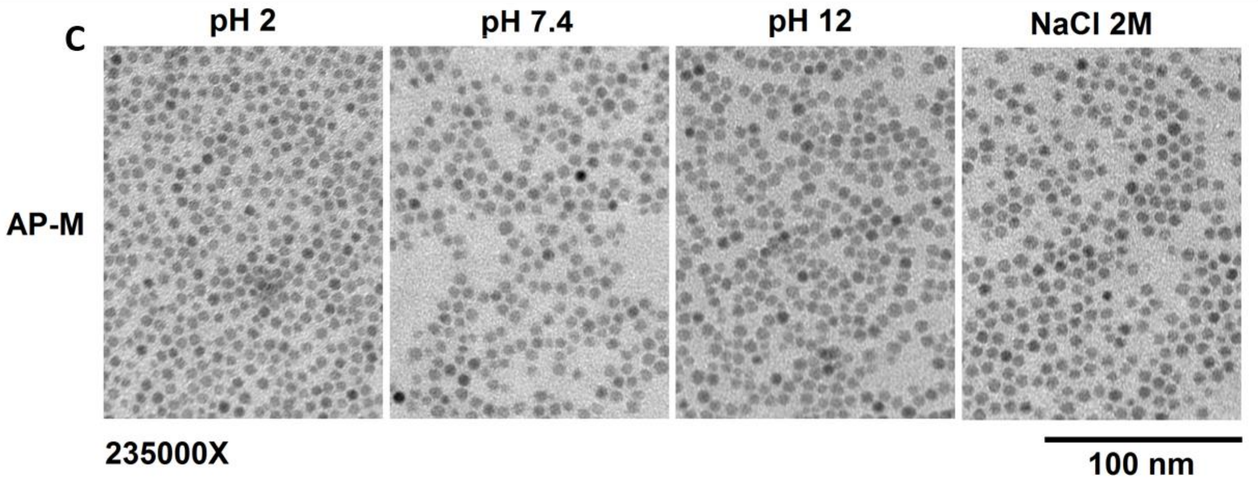

S

FIGURE 15 APM STABILITY

(A) Size and PDI of APM in various conditions for 14 days. (B) APM in various conditions after one or two month storage. (C) TEM of APM in various conditions after one month storage.

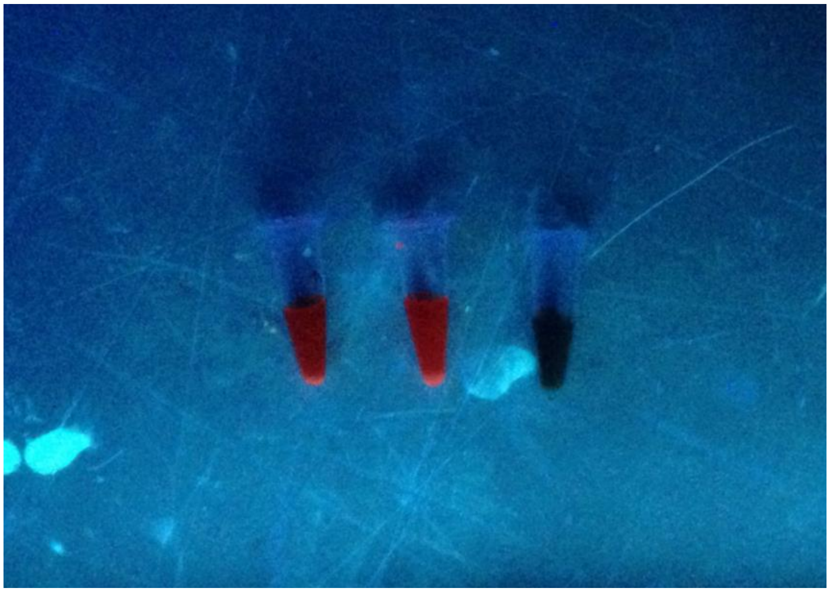

FIGURE 16 SPIO COATED WITH DIFFERENT VISUALIZED BY UV LIGHT EXPOSURE

SPIO coated with CF633 conjugated ALN-PEG polymer (left), CF633 conjugated ALN-PEG and ALN-PEG-Folate polymer (middle) and oleic acid (right) visualized by UV light (254nm) exposure

5. Chapter V APM and FAPM biodistribution analyzed by MRI

5.1. Abstract

In this proof-of-concept study, biodistribution of APM and FAPM in male Balb/cJ mice were evaluated. The magnetite concentration was quantified from the change in T_2 weighted relaxivity ($\Delta R_2 = 1/T_{2preinjection} - 1/T_{2postinjection}$) and the per milligram magnetite relaxivity (r_2) determined as the slope of magnetite concentration versus R_2 in relaxivity studies.

To this end, we made SMART nanoparticles to rapidly assess ART tissue biodistribution. SMART testing previously demonstrated near equivalence in drug biodistribution and PK amongst MRI and drug tissue measurements. Herein, we have taken this work a step further by demonstrating the utility of FA decoration to facilitate ART targeting. FAPM improved entry and particle retention to the reticuloendothelial system over replicate untargeted formulations. The feasibility of imaging APM and FAPM biodistribution in vivo using MRI was investigated in this chapter. We posit that MRI testing can predict drug biodistribution, and that the value of targeted magnetite is of immediate benefit towards the rapid assessment of biodistribution for enhanced drug tissue concentrations in viral reservoirs in the quest for chemical eradication of HIV infection.

Our immunohistochemical analysis further demonstrates that APM and FAPM particles are taken up by liver and spleen macrophages which serve as the reservoir of these particles, as well as the major targets of HIV.

5.2. Introduction

Regimen adherence, systemic toxicities and limited drug penetrance to viral reservoirs are obstacles limiting the effectiveness of long-term antiretroviral therapy. The development of monocyte-macrophage-targeted nanoART, while providing opportunities to simplify drug dosing regimens, has proved more limited for its abilities to improve drug penetrance into viral cell and tissue reservoirs. Research progress was slowed by the extensive time needed to complete pharmacokinetic, pharmacodynamics and biodistribution testing of nanoART efficacy. We have developed APM and FAPM platform (158). Their biodistribution would readily be quantitated by a conventional MRI scan to reflect the targeting ability of the ligand (127, 163).

Our previous studies demonstrated that FR are expressed in differentiated macrophages, as cell lysates were probed with antibodies to FR1 and FR2 (FRβ) and showed that FRβ but not FR1 is expressed and localized to the cell membrane. Engagement of the FR receptor in enhancing FA-coated nanoART uptake was demonstrated by the ability of free FA to block enhanced FA-nanoART uptake. Our in vitro studies have demonstrated that the administration of nanoART stimulated the expression in the FR receptor in macrophages (164).

NanoART with or without the FA targeting ligand were injected into mice to confirm the usefulness of magnetite to assess ART biodistribution. Such a system can provide a relevant screening platform and could be used to investigate a broader range of targeting systems for delivery of nanoART to reservoir sites of viral infection.

5.3. Experimental Procedures

5.3.1. Manufacture and characterization of FA-P407-ATV/r

Manufacture of nanoATV/r was prepared as described before (165). FA-P407 was synthesized and used to manufacture FA-nanoATV/r (149). For preparation of FA-P407 ATV and FA-P407-RTV, FA-P407 (0.2% w/v) and P407 (0.3% w/v) were mixed in 10 mm HEPES to generate micelles; 1% (w/v) drug was added and mixed overnight. For preparation of P407-ATV and P407-RTV, 0.5% (w/v) P407 was mixed with 1% drug. The suspensions were homogenized at 20,000 PSI using an Avestin Emulsiflex C3 homogenizer (Avestin Inc, Ottawa, ON, Canada) until the desired particle size (300–400 nm) was reached. Free polymers and non-encapsulated drug particles were removed by centrifugation; the nanoparticles were resuspended in 0.2% P407. The resulting nanosuspension was lyophilized and stored in a desiccator protected from light. Drug loading was determined using reversed phase HPLC and UPLC-MS/MS as described. Particle size, PDI and zeta potential for the nanoformulations were determined by dynamic light scattering using a Malvern Zetasizer Nano-ZS instrument (Malvern Instruments Inc., Westborough, MA, USA).

5.3.2. Biodistribution of APM and FAPM

Biodistribution of APM and FAPM was determined in male Balb/cJ mice (Jackson Labs, Bar Harbor, ME) after 2 weeks on folate deficient diet (Harlan Teklad TD.00434, Harlan Laboratories, Indianapolis, IN). Twenty-four hours before administration of magnetite particles, mice were injected with LPS (Sigma-Aldrich St. Louis, MO) at 2 mg/kg dose intraperitoneally, or injected with 100 mg/kg nanoparticle-based RTV boosted ATV coated with poloxamer 407 (nanoATV/r), intramuscularly. APM or FAPM (2 mg iron/kg wt) were injected intravenously in a total volume of 100 µl for each mouse. The mice were scanned by MRI before and 24 hours after APM or FAPM injection.

5.3.3. MRI acquisition and analyses

MRI was acquired using a 7T/16cm Bruker Pharmascan MRI/MRS scanner (Ettlingen, Germany) and a commercial mouse body resonator. Magnetite detection by MRI was done using T_2 mapping for quantitation and T_2^* weighted high resolution imaging for detection of biodistribution throughout the body. The sequence used for T_2 mapping was a CPMG phase cycled multislice multiecho sequence. Forty-one 0.5 mm thick contiguous interleaved coronal images were acquired with an acquisition matrix of 256 x 192, 40 mm field of view, 12 echoes at 10 ms first echo time and 10 ms echo spacing, repetition time of 4680 ms, three averages, for a total acquisition time of 30 min. T_2^* weighted MRI was acquired using a 3D spoiled gradient recalled echo sequence with echo time = 3 ms, repetition time = 10 ms, 15 degree pulse angle, 50 x 40 x 30 mm FOV, 256 x 196 x 128 acquisition matrix, six averages, for a total scan time of 25min.

T_2 maps were reconstructed using custom programs written in Interactive Data Language (IDL; Exelis Visual Information Solutions, McLean, VA). Preinjection and 24 hour postinjection maps were constructed using the even-echo images from the CPMG phase cycled imaging data set. Mean tissue T_2 was determined using ROI analyses before and after magnetite injection for the 24 hour results. Magnetite concentration was then determined from the change in relaxivity ($\Delta R_2 = 1/T_{2preinjection} - 1/T_{2postinjection}$) and the per milligram magnetite particle relaxivity (r_2) determined as the slope of magnetite concentration versus R_2 in phantom studies. The ROI analyses were performed using ImageJ (http://imagej.nih.gov/Ij) software.

5.3.4. PK of FA-nanoATV/r

Male Balb/cJ mice (Jackson Labs), 4-6 weeks old, were maintained on folate-deficient diet for 2 weeks then injected with 50 mg/kg of nanoATV/r or FA conjugated nanoATV/r (FA-nanoATV/r). The mice were sacrificed on day 7. Mice with LPS treatment received LPS (2 mg/kg) 24 hours before receiving drug and were sacrificed on day 14. The mice were injected with either 50 mg/kg of nanoATV/r or FA-nanoATV/r. Tissues were collected and stored at -80^{o}C. Tissue drug levels were determined using UPLC-MS/MS as previously described (166).

5.3.5. Immunofluorescence

Immunofluorescence staining of magnetite particles was determined in male Balb/cJ mice (Jackson Labs) after 2 weeks on folate deficient diet. Twenty-four hours before administration of magnetite particles, mice were injected intraperitoneally with LPS at 2 mg/kg, or injected with 100 mg/kg nanoATV/r, intramuscularly. CF633-labeled APM or CF633-labeled FAPM (2 mg iron/kg wt) was injected intravenously in a total volume of 100 µl for each mouse. After 24 hours, tissues were collected following the MRI scan for immunofluorescence staining.

Preparations of whole-mount tissues and frozen sections: tissues were collected after whole mouse perfusion with PBS and fixed in 10% neutral buffered formalin for 24 hours, then incubated in 15% and 30% sucrose for cryoprotection and embedded in optical cutting temperature compound (OCT) (Tissue-Tek) at −20 °C. For whole-mount staining, tissues were cut to 20 µm on a cryostat. Tissues were carefully harvested from melting OCT. Immunofluorescence staining of frozen sections: sections were blocked/permeabilized in Tris Buffered Saline with Tween (TBBS) containing 10% normal goat serum, and stained with rabbit monoclonal antibody against Iba-1 (1:500; Wako Chemicals, USA) and mouse monoclonal antibody against FRβ (a generous gift of Dmitry Dmitrov, National Cancer Institute, Bethesday, MD) (1:200) for 1 hour at room temperature. Primary antibodies were labeled with secondary goat anti-mouse for FRβ antibody and anti-rabbit antibodies for Iba-1 conjugated to the fluorescent probes Alexa Fluor 488 and Alexa Fluor 594, and nuclei were labeled with 4′,6-diamidino-2-phenylindole (DAPI). Images were acquired with a Nikon swept field confocal microscope (Nikon).

5.3.6. Statistical analyses

The data are presented as mean ± SEM. Statistical significance between groups was assessed using Student's T-test by Graph-Pad® Prism unless specified. The data were considered statistically significant if $P < 0.05$.

5.4. Result

5.4.1. MRI acquisition and analyses

Our previous studies showed that administration of nanoART activated macrophages and stimulated the overexpression of FR *in vivo* (149). For the evaluation of the biodistribution of non-targeted APM and macrophage-targeted FAPM, and their localization within macrophages in mice, the immune system of mice was first activated with LPS or nanoATV/r, and then APM or FAPM were administered via intravenous injection. The APM and FAPM biodistribution were determined by MRI. Figure 17A displays 0.128 mm thick T_2* weighted high-resolution 3D FLASH images of the same mouse before and 24 hours after injection of APM or FAPM. Presence of magnetite in tissue causes a reduction of T_2* causing signal loss in proportion to concentration at TE = 3 ms in the liver, spleen, and some abdominal regions.

5.4.2. Biodistribution of APM and FAPM

APM (n=6) and FAPM (n=6) biodistribution in LPS or nanoATV/r treated mice were quantified from regions of interest in MRI T_2 maps (Figure 17B and C). It can be appreciated that in animals treated with LPS, FAPM showed a higher accumulation in various tissues compared to APM (2.49 vs 0 µg/ml for renal pelvis, 5.49 vs 0 µg/ml for renal cortex, 10.94 vs 2 µg/ml for spleen and 26.26 vs 10.48 µg/ml for liver) (Figure 17B) In animals treated with nanoATV/r, FAPM also showed more accumulation in various tissues compared to APM (1.02 vs 0 µg/ml for renal pelvis, 0.69 vs 0 µg/ml for renal cortex, 13.07 vs 5.79 µg/ml for spleen and 17.27 vs 7.53 µg/ml for liver) (Figure 17C). FAPM accumulated more in various tissues, which demonstrated its targeting ability to FR on activated tissue macrophages, and showed the potential of APM and FAPM for assessing image-guided drug PK and BD.

To further confirm this concept, biodistribution of nanoATV/r or FA-nanoATV/r was evaluated in Balb/cJ mice with or without LPS activation. The mice were injected with either 50 mg/kg of nanoATV/r or FA-nanoATV/r, and the drug concentrations in different tissues were quantified by UPLC/MS-MS. The tissue ATV concentrations following treatment with FA-nanoATV/r were significantly higher than with nanoATV/r and were found to be dose dependent. A 50 mg/kg FA-nanoATV/r dose gave 1.82 µg/g and 208 ng/g ATV concentrations in liver and spleen, respectively, compared to 439 ng/g and 145 ng/g in liver and spleen following nanoATV/r treatment in LPS-treated mice (Figure 18 A). Alternately, the ATV tissue concentrations following FA-nanoATV/r were 2.93 µg/g and

86.3 ng/g compared to 146 ng/g and 2.36 ng/g for nanoATV/r in liver and spleen, respectively in mice treated only with nanoATV/r (Figure 18 B).

5.4.3. Immunofluorescence

To confirm the *in vivo* FR-targeting ability of FAPM, the colocalizaiton of magnetite particle and FR was also studied by administration of CF633-labeled APM and FAPM (CF633-APM and CF633-FAPM) to mice. Mouse FRβ antibody and Iba-1 antibody were used to determine colocalization. These were used to detect FR and macrophages. Results obtained by immunofluorescent staining clearly showed co-localization of FRβ FRβ and Iba1 in spleen from mice injected with LPS and nanoATV/r, in agreement with the hypothesis that activated macrophages express FRβ. In addition, CF633-labeled FAPM were mainly detected in Iba-1+/FR+ cells (Figure 19A and B).

5.5. Discussion

Figure 17A displays 0.128 mm thick T_2* weighted high-resolution 3D FLASH images of the same mouse before and 24 hours after injection of APM or FAPM. Presence of magnetite in tissue causes a reduction of T_2* causing signal loss in proportion to concentration at TE = 3 ms in the liver, spleen, and some abdominal regions. The shortening in the T_2* value correlates with the signal intensity decrease as a result of the strong magnetite susceptibility effects. As a result, tissues containing magnetite appear darker in post scans demonstrating higher accumulation of FAPM systemically in both LPS and nanoATV/r pre-treated mice. This method is semi-quantitative, however it does allow ready identification of the presence of magnetite throughout the body, which can be used to guide quantitative ROI analyses using T_2 maps.

Prussian blue staining of tissue sections was also performed in liver and spleens of FAPM treated animals, but showed discordant results. One potential confounding factor is that the oxidation of magnetite during perfusion and tissue processing could prevent the success of Prussian blue staining. It is also possible that the ultra small size of the magnetite results in staining that is undetectable.

In conclusion, we observed parallel patterns of tissue biodistribution between nanoATV/r or FA-nanoATV/r and APM and FAPM in treated mice. Notably, these comparable distributions of ATV and magnetite concentrations confirmed the ability of our ALN-PEG coated magnetite system to be used as a targeting ligand approach to predict actual drug PK and tissue BD. Future direction includes replacing FA with other macrophages targeting ligands. Cancer targeting ligands can also be tested in this platform.

A

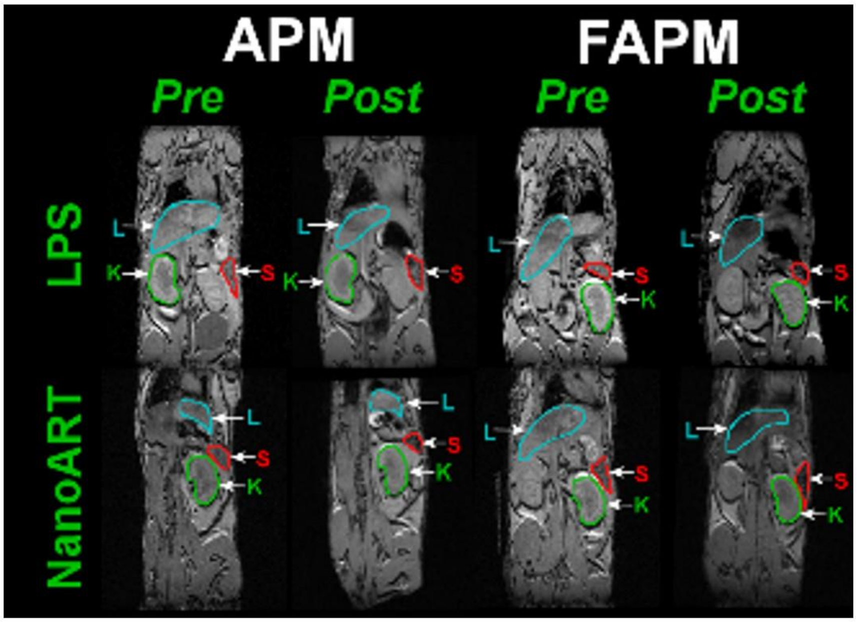

B

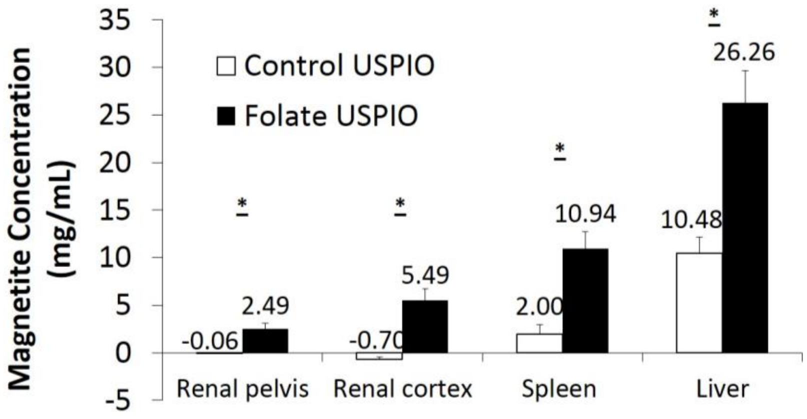
35
30
25
20
15
10
5
0
-5
Magnetite Concentration (mg/mL)
☐ Control USPIO
■ Folate USPIO
*
*
*
*
-0.06
2.49
-0.70
5.49
2.00
10.94
10.48
26.26
Renal pelvis
Renal cortex
Spleen
Liver

C

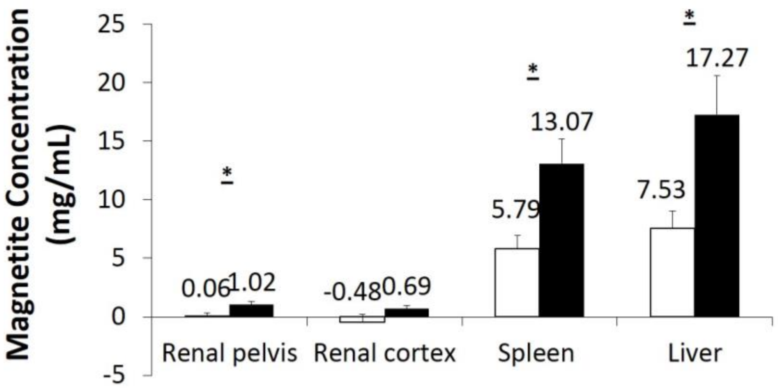
25
20
15
10
5
0
-5
Magnetite Concentration (mg/mL)
*
*
*
0.06
1.02
-0.48
0.69
5.79
13.07
7.53
17.27
Renal pelvis
Renal cortex
Spleen
Liver

FIGURE 17 APM AND FAPM BIODISTRIBUTION

(A) 3D gradient recalled echo images of the same mouse before (pre) and 24 hours after (post) injection of APM or FAPM. APM and FAPM biodistribution in renal pelvis, renal cortex, spleen and liver, quantified by T_2 MRI in (B) LPS or (C) nanoATV/r treated mice. Data are presented as mean±SEM, $*P < 0.05$ considered significant using Student’s t-test.

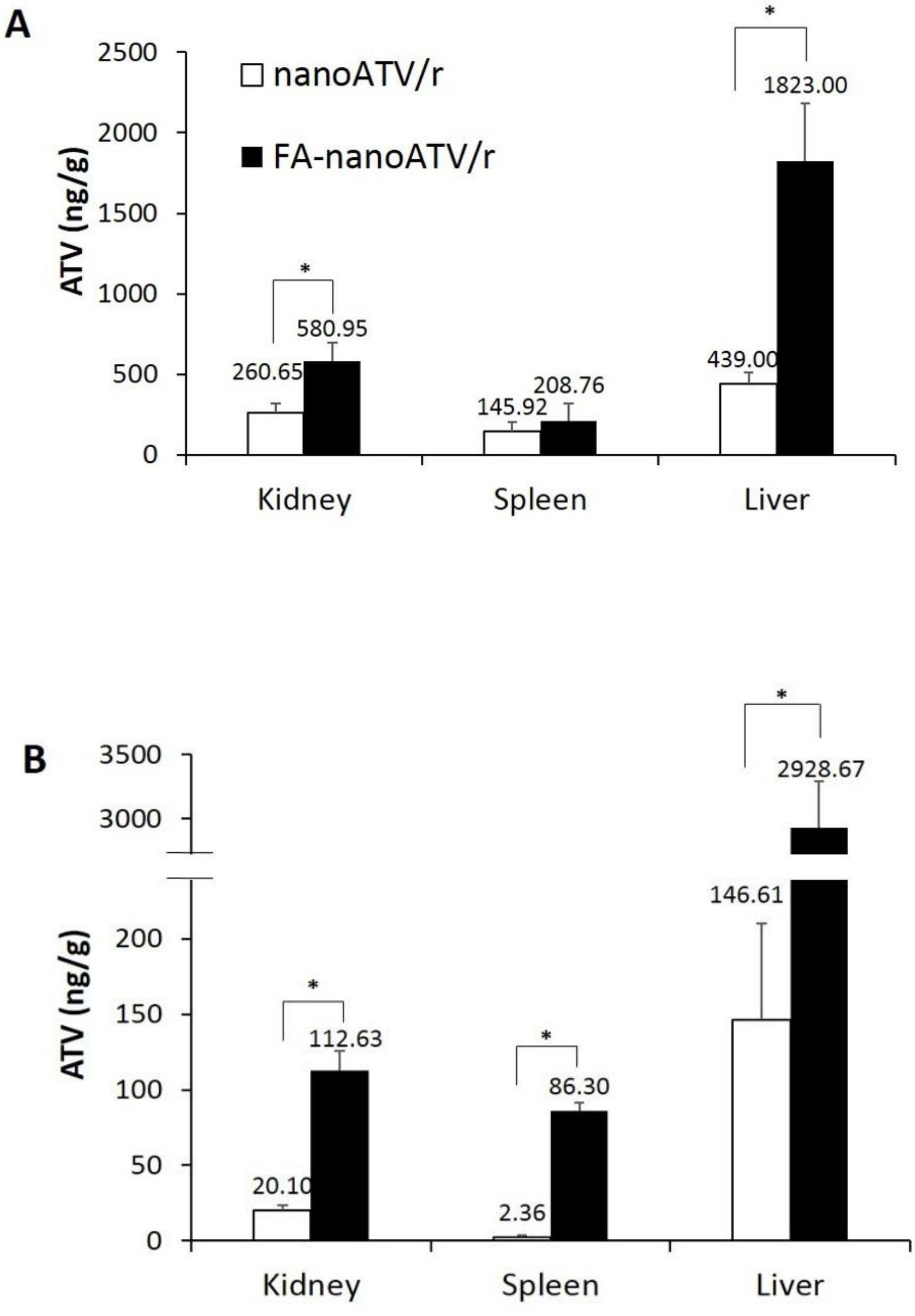
A
2500
2000
1500
1000
500
0
ATV (ng/g)
☐ nanoATV/r
■ FA-nanoATV/r
*
260.65
580.95
145.92
208.76
*
439.00
1823.00
Kidney
Spleen
Liver
B
3500
3000
200
150
100
50
0
ATV (ng/g)
*
20.10
112.63
*
2.36
86.30
*
146.61
2928.67
Kidney
Spleen
Liver

FIGURE 18 NANOATV/R AND FA-NANOATV/R BIODISTRIBUTION IN KIDNEY, SPLEEN AND LIVER AS QUANTIFIED BY UPLC-MS/MS

These are shown for nanoATV/r in (A) LPS and (B) nanoATV/r treated mice. Data are presented as mean±SEM, *$P < 0.05$ considered significant using Student's t-test. Panel A and B are days 7 and 14, respectively.

LPS

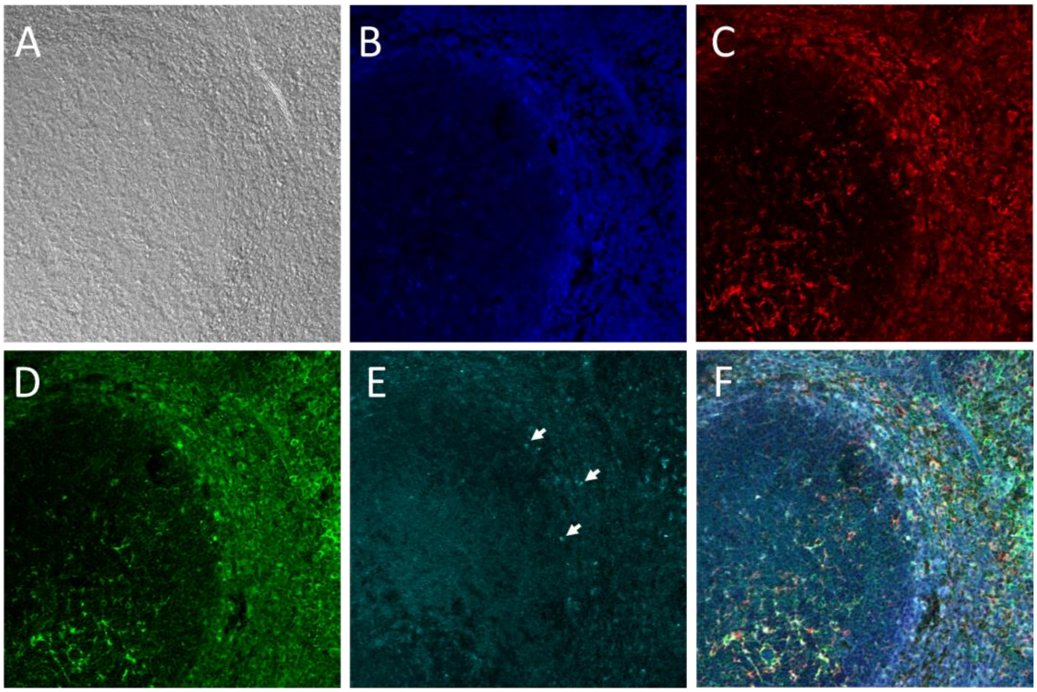

nanoATV/r

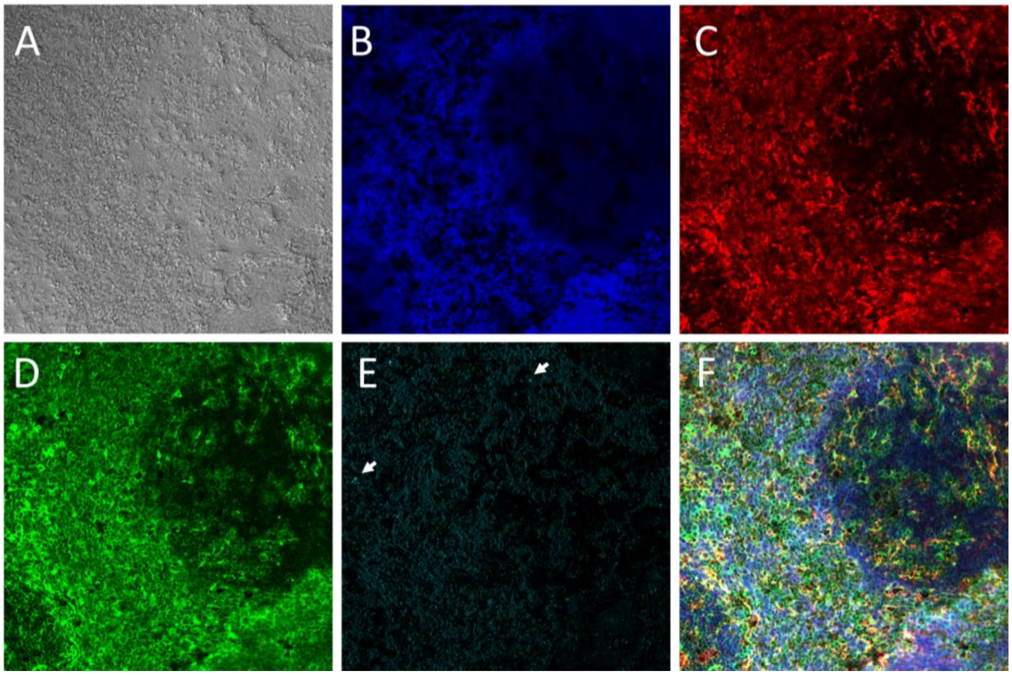

FIGURE 19 IMMUNOFLUORESCENCE STAINING OF FAPM BIODISTRIBUTION

Immunofluorescence staining of FAPM biodistribution in LPS treated mouse spleen (top) or nanoATV/r treated mouse spleen (bottom), 200x. (A) phase contrast, (B) DAPI, (C) IBA-1, (D) folate receptor, (E) magnetite (arrow indicates individual magnetite) and (F) merge.

6. Chapter VI Discussion

There is a considerable focus amongst HIV/AIDS researchers towards the development of reliable methods to bring drugs to reservoir sites with the explicit goal of eliminating virus. HIV-1 is present for long periods of time in gut, lymphoid and brain reservoirs thus constituting obstacles for viral eradication within infected individuals (160). One way to reduce residual virus in its reservoirs is by targeted antiretroviral nanotherapy (136, 149, 161). A hurdle towards achieving this goal is the dearth of ways to measure ART distribution outside of plasma drug levels (118). In addition, adequate targeting schemes have not yet been achieved and current methods to develop them are commonly slow and cumbersome. To such ends our own works have centered on ways to bridge classic PK evaluation with MRI assessment of particle distributions (158).

Taken together, we have developed a polymer system rests in the ability to utilize MRI scans to rapidly assess cell and tissue drug biodistribution. SMART particles is polymer-encased dual magnetite and drug particle which is hard to manufacture due to the different nature of the components. So it is important to find the right composition. More magnetite will interfere with the incorporation of the ART drug, on the other hand, less magnetite will cause inefficient MRI signal. After testing different condition for drug release and relaxivity, we identified that the best drug vs magnetite ratio is 3:1, in which particles has slow drug release while has adequate magnetite to generate MRI signal. To increase the biocompatibility of SMART, we used DSPC and DSPE-PEG2k as the shell of SMART system. To increase drug loading, we used PLGA as the core. To the best of our knowledge, this is the first attempt to develop lipid-coated PLGA nanoparticles for HIV therapeutics.

During the first 30 mins of SMART administration, magnetite levels in kidney, spleen and liver were similar due to the magnetite is still circulating in the blood stream. As magnetite started to distribute, a higher amount stayed in liver and spleen after 4 hours of injection, correlated with higher concentration of magnetite in these organs in 24 hours MRI scan. Our in vivo MRI results also showed that the concentrations of magnetite and ATV in mouse tissues, such as liver, spleen and kidney, correlate with one another at 24 h after injection.

The results support the idea that SMART technology could facilitate the noninvasive evaluation of drug PK and biodistribution in virus target tissues by MRI. Also it demonstrates the capability of MRI to be used for monitoring ATV distribution by tracking the presence of magnetite in tissue which causes a reduction of T_2*. Targeted drug when combined with suitable imaging techniques like SMART particles could facilitate this goal by providing a “go/no go” for treatment success. This technology clearly opens new opportunities to develop platforms that would accelerate elimination of viral infections.

Another polymer based magnetite system (APM) is also developed for non-invasive biodistribution study of targeting ligand conjugated nanoparticle. FA is capable of specific interaction with cells expressing the FR. As FR expression is restricted to a few cell types, including kidney epithelial cells and mononuclear phagocytes lineage (92) and expression is regulated by cell activation as present in disease specific targeting of drug can parallel tissue sites of infection and inflammation along with the reticuloendothelial system which could then act as a drug storage depot (136, 137). This, notably, makes FA conjugation specifically for antiretroviral therapeutic nanoparticles of particular benefit for treatment of HIV infection (162).

We have manufactured a single magnetite particle that is easy to conjugate targeting ligands with, the other potential targeting ligands includes mannose, antibody and peptides. We posit that the targeting ability of different ligands can be studied further by targeting ligand testing of linked magnetic nanoparticles and parallel MRI evaluation of particle distribution. Moreover, we theorize that such results would closely mimic drug tissue biodistribution with the same targeting ligands.

Future direction includes decorating magnetite with other macrophages targeting ligands or even CD4+ T cells ligands. These potential ligands include HIV gp120-derived peptides (e.g. CKGIRIGPGRAVYAAE), CCR5-targeting RANTES fragments, hyaluronic acid, mannose derivatives, and combinations of those ligands.

Targeting ligand with highest accoumlation in viruse reversior found by MRI scanning will be used to conjugate NanoART particles. Currently NanoART is composed of ATV or RTV which is not a WHO recommended first line HIV drug. Usage of the first line HIV treatment for nanoart is promising. NRTIs like 3TC and abacavir, or entry inhibitor maraviroc are good candidates to incorporate into nanoart to extend drug half-life and increase bioavailability. NanoART composed of the novel prodrugs and their combinations can also be prepared using homogenization. Formulations of optimal physical characteristics will be determined from particle size, charge, PDI and drug loading capacity to ensure rapid uptake by targeted cells and drug potency. These nanoART with new drugs can be coated with targeting ligands found by magnetite system to further facilitate immune responses and promote clearance of virus from cellular reservoirs. Targeting formulation vs non-targeting formulation uptake by targeted cells will be tested to evaluate targeting efficiency of the ligand.

References

1. Hammer SM, Squires KE, Hughes MD, Grimes JM, Demeter LM, Currier JS, et al. A controlled trial of two nucleoside analogues plus indinavir in persons with human immunodeficiency virus infection and CD4 cell counts of 200 per cubic millimeter or less. AIDS Clinical Trials Group 320 Study Team. N Engl J Med. 1997 Sep 11;337(11):725-33.

2. Ho DD, Neumann AU, Perelson AS, Chen W, Leonard JM, Markowitz M. Rapid turnover of plasma virions and CD4 lymphocytes in HIV-1 infection. Nature. 1995 Jan 12;373(6510):123-6.

3. Fanales-Belasio E, Raimondo M, Suligoi B, Butto S. HIV virology and pathogenetic mechanisms of infection: a brief overview. Ann Ist Super Sanita. 2010;46(1):5-14.

4. Sierra S, Kupfer B, Kaiser R. Basics of the virology of HIV-1 and its replication. J Clin Virol. 2005 Dec;34(4):233-44.

5. Gelderblom HR, Ozel M, Pauli G. Morphogenesis and morphology of HIV. Structure-function relations. Arch Virol. 1989;106(1-2):1-13.

6. Emerman M, Malim MH. HIV-1 regulatory/accessory genes: keys to unraveling viral and host cell biology. Science. 1998 Jun 19;280(5371):1880-4.

7. Farnet CM, Bushman FD. HIV cDNA integration: molecular biology and inhibitor development. AIDS. 1996;10 Suppl A:S3-11.

8. Altfeld M, Gale M,Jr. Innate immunity against HIV-1 infection. Nat Immunol. 2015 May 19;16(6):554-62.

9. Rustagi A, Gale M,Jr. Innate antiviral immune signaling, viral evasion and modulation by HIV-1. J Mol Biol. 2014 Mar 20;426(6):1161-77.

10. Malim MH, Emerman M. HIV-1 accessory proteins--ensuring viral survival in a hostile environment. Cell Host Microbe. 2008 Jun 12;3(6):388-98.

11. van Montfoort N, Olagnier D, Hiscott J. Unmasking immune sensing of retroviruses: interplay between innate sensors and host effectors. Cytokine Growth Factor Rev. 2014 Dec;25(6):657-68.

12. De Cock KM. Epidemiology and Transmission of HIV-2. JAMA. 1993;270(17):2083.

13. Kanki PJ, Travers KU, Marlink RG, Essex ME, MBoup S, Gueye-NDiaye A, et al. Slower heterosexual spread of HIV-2 than HIV-1. The Lancet. 1994;343(8903):943 <last_page> 946.

14. Marlink R, Kanki P, Thior I, Travers K, Eisen G, Siby T, et al. Reduced rate of disease development after HIV-2 infection as compared to HIV-1. Science. 1994;265(5178):1587 <last_page> 1590.

15. O'Donovan D, Ariyoshi K, Milligan P, Ota M, Yamuah L, Sarge-Njie R, et al. Maternal plasma viral RNA levels determine marked differences in mother-to-child transmission rates ofHIV-1 and HIV-2 in The Gambia. AIDS. 2000;14(4):441 <last_page> 448.

16. Alimonti JB. Mechanisms of CD4+ T lymphocyte cell death in human immunodeficiency virus infection and AIDS. J Gen Virol. 2003;84(7):1649 <last_page> 1661.

17. Douek DC, Roederer M, Koup RA. Emerging concepts in the immunopathogenesis of AIDS. Annu Rev Med. 2009;60:471-84.

18. Wei X, Ghosh SK, Taylor ME, Johnson VA, Emini EA, Deutsch P, et al. Viral dynamics in human immunodeficiency virus type 1 infection. Nature. 1995 Jan 12;373(6510):117-22.

19. Dong C, Kwas C, Wu L. Transcriptional restriction of human immunodeficiency virus type 1 gene expression in undifferentiated primary monocytes. J Virol. 2009 Apr;83(8):3518-27.

20. Ullum H, Cozzi Lepri A, Victor J, Aladdin H, Phillips AN, Gerstoft J, et al. Production of beta-chemokines in human immunodeficiency virus (HIV) infection: evidence that high levels of macrophage inflammatory protein-1beta are associated with a decreased risk of HIV disease progression. J Infect Dis. 1998 Feb;177(2):331-6.

21. Borrow P, Lewicki H, Wei X, Horwitz MS, Peffer N, Meyers H, et al. Antiviral pressure exerted by HIV-1-specific cytotoxic T lymphocytes (CTLs) during primary infection demonstrated by rapid selection of CTL escape virus. Nat Med. 1997 Feb;3(2):205-11.

22. Goulder PJ, Phillips RE, Colbert RA, McAdam S, Ogg G, Nowak MA, et al. Late escape from an immunodominant cytotoxic T-lymphocyte response associated with progression to AIDS. Nat Med. 1997 Feb;3(2):212-7.

23. Pantaleo G, Soudeyns H, Demarest JF, Vaccarezza M, Graziosi C, Paolucci S, et al. Evidence for rapid disappearance of initially expanded HIV-specific CD8+ T cell clones during primary HIV infection. Proc Natl Acad Sci U S A. 1997 Sep 2;94(18):9848-53.

24. Fauci AS, Pantaleo G, Stanley S, Weissman D. Immunopathogenic mechanisms of HIV infection. Ann Intern Med. 1996 Apr 1;124(7):654-63.

25. Grossman Z, Meier-Schellersheim M, Paul WE, Picker LJ. Pathogenesis of HIV infection: what the virus spares is as important as what it destroys. Nat Med. 2006 Mar;12(3):289-95.

26. Cohen MS, Chen YQ, McCauley M, Gamble T, Hosseinipour MC, Kumarasamy N, et al. Prevention of HIV-1 infection with early antiretroviral therapy. N Engl J Med. 2011 Aug 11;365(6):493-505.

27. Tanser F, Barnighausen T, Grapsa E, Zaidi J, Newell ML. High coverage of ART associated with decline in risk of HIV acquisition in rural KwaZulu-Natal, South Africa. Science. 2013 Feb 22;339(6122):966-71.

28. Das K, Arnold E. HIV-1 reverse transcriptase and antiviral drug resistance. Part 1. Curr Opin Virol. 2013 Apr;3(2):111-8.

29. Kabbara WK, Ramadan WH. Emtricitabine/rilpivirine/tenofovir disoproxil fumarate for the treatment of HIV-1 infection in adults. J Infect Public Health. 2015 May 19.

30. De Clercq E. The role of non-nucleoside reverse transcriptase inhibitors (NNRTIs) in the therapy of HIV-1 infection. Antiviral Res. 1998 Jun;38(3):153-79.

31. Conway B, Wainberg MA, Hall D, Harris M, Reiss P, Cooper D, et al. Development of drug resistance in patients receiving combinations of zidovudine, didanosine and nevirapine. AIDS. 2001 Jul 6;15(10):1269-74.

32. Johnson VA, Brun-Vezinet F, Clotet B, Gunthard HF, Kuritzkes DR, Pillay D, et al. Update of the drug resistance mutations in HIV-1: December 2009. Top HIV Med. 2009 Dec;17(5):138-45.

33. Kwong PD, Wyatt R, Sattentau QJ, Sodroski J, Hendrickson WA. Oligomeric modeling and electrostatic analysis of the gp120 envelope glycoprotein of human immunodeficiency virus. J Virol. 2000 Feb;74(4):1961-72.

34. Weiss CD, Levy JA, White JM. Oligomeric organization of gp120 on infectious human immunodeficiency virus type 1 particles. J Virol. 1990 Nov;64(11):5674-7.

35. Chan DC, Fass D, Berger JM, Kim PS. Core structure of gp41 from the HIV envelope glycoprotein. Cell. 1997 Apr 18;89(2):263-73.

36. Wild CT, Shugars DC, Greenwell TK, McDanal CB, Matthews TJ. Peptides corresponding to a predictive alpha-helical domain of human immunodeficiency virus type 1 gp41 are potent inhibitors of virus infection. Proc Natl Acad Sci U S A. 1994 Oct 11;91(21):9770-4.

37. Hazuda DJ, Felock P, Witmer M, Wolfe A, Stillmock K, Grobler JA, et al. Inhibitors of strand transfer that prevent integration and inhibit HIV-1 replication in cells. Science. 2000 Jan 28;287(5453):646-50.

38. Yoder KE, Bushman FD. Repair of gaps in retroviral DNA integration intermediates. J Virol. 2000 Dec;74(23):11191-200.

39. Pommier Y, Johnson AA, Marchand C. Integrase inhibitors to treat HIV/AIDS. Nat Rev Drug Discov. 2005 Mar;4(3):236-48.

40. Gunthard HF, Aberg JA, Eron JJ, Hoy JF, Telenti A, Benson CA, et al. Antiretroviral treatment of adult HIV infection: 2014 recommendations of the International Antiviral Society-USA Panel. JAMA. 2014 Jul 23-30;312(4):410-25.

41. Perelson AS, Essunger P, Cao Y, Vesanen M, Hurley A, Saksela K, et al. Decay characteristics of HIV-1-infected compartments during combination therapy. Nature. 1997 May 8;387(6629):188-91.

42. Lucas M, Karrer U, Lucas A, Klenerman P. Viral escape mechanisms--escapology taught by viruses. Int J Exp Pathol. 2001 Oct;82(5):269-86.

43. Chun TW, Finzi D, Margolick J, Chadwick K, Schwartz D, Siliciano RF. In vivo fate of HIV-1-infected T cells: quantitative analysis of the transition to stable latency. Nat Med. 1995 Dec;1(12):1284-90.

44. Chun T-, Stuyver L, Mizell SB, Ehler LA, Mican JAM, Baseler M, et al. Presence of an inducible HIV-1 latent reservoir during highly active antiretroviral therapy. Proceedings of the National Academy of Sciences. 1997;94(24):13193 <last_page> 13197.

45. Wong JK. Recovery of Replication-Competent HIV Despite Prolonged Suppression of Plasma Viremia. Science. 1997;278(5341):1291 <last_page> 1295.

46. Finzi D. Identification of a Reservoir for HIV-1 in Patients on Highly Active Antiretroviral Therapy. Science. 1997;278(5341):1295 <last_page> 1300.

47. Pierson T, Hoffman TL, Blankson J, Finzi D, Chadwick K, Margolick JB, et al. Characterization of chemokine receptor utilization of viruses in the latent reservoir for human immunodeficiency virus type 1. J Virol. 2000 Sep;74(17):7824-33.

48. Chun TW, Engel D, Berrey MM, Shea T, Corey L, Fauci AS. Early establishment of a pool of latently infected, resting CD4(+) T cells during primary HIV-1 infection. Proc Natl Acad Sci U S A. 1998 Jul 21;95(15):8869-73.

49. Chun TW, Engel D, Mizell SB, Ehler LA, Fauci AS. Induction of HIV-1 replication in latently infected CD4+ T cells using a combination of cytokines. J Exp Med. 1998 Jul 6;188(1):83-91.

50. Sonza S, Mutimer HP, Oelrichs R, Jardine D, Harvey K, Dunne A, et al. Monocytes harbour replication-competent, non-latent HIV-1 in patients on highly active antiretroviral therapy. AIDS. 2001 Jan 5;15(1):17-22.

51. Gordon S, Taylor PR. Monocyte and macrophage heterogeneity. Nat Rev Immunol. 2005 Dec;5(12):953-64.

52. Murray PJ, Wynn TA. Protective and pathogenic functions of macrophage subsets. Nat Rev Immunol. 2011 Oct 14;11(11):723-37.

53. Bellingan GJ, Caldwell H, Howie SE, Dransfield I, Haslett C. In vivo fate of the inflammatory macrophage during the resolution of inflammation: inflammatory macrophages do not die locally, but emigrate to the draining lymph nodes. J Immunol. 1996 Sep 15;157(6):2577-85.

54. Gras G, Kaul M. Molecular mechanisms of neuroinvasion by monocytes-macrophages in HIV-1 infection. Retrovirology. 2010 Apr 7;7:30,4690-7-30.

55. Schnell G, Joseph S, Spudich S, Price RW, Swanstrom R. HIV-1 replication in the central nervous system occurs in two distinct cell types. PLoS Pathog. 2011 Oct;7(10):e1002286.

56. Igarashi T, Brown CR, Endo Y, Buckler-White A, Plishka R, Bischofberger N, et al. Macrophage are the principal reservoir and sustain high virus loads in rhesus macaques after the depletion of CD4+ T cells by a highly pathogenic simian immunodeficiency virus/HIV type 1 chimera (SHIV): Implications for HIV-1 infections of humans. Proc Natl Acad Sci U S A. 2001 Jan 16;98(2):658-63.

57. Swingler S, Mann AM, Zhou J, Swingler C, Stevenson M. Apoptotic killing of HIV-1-infected macrophages is subverted by the viral envelope glycoprotein. PLoS Pathog. 2007 Sep 7;3(9):1281-90.

58. Reynoso R, Wieser M, Ojeda D, Bonisch M, Kuhnel H, Bolcic F, et al. HIV-1 induces telomerase activity in monocyte-derived macrophages, possibly safeguarding one of its reservoirs. J Virol. 2012 Oct;86(19):10327-37.

59. Orenstein JM, Meltzer MS, Phipps T, Gendelman HE. Cytoplasmic assembly and accumulation of human immunodeficiency virus types 1 and 2 in recombinant human colony-stimulating factor-1-treated human monocytes: an ultrastructural study. J Virol. 1988 Aug;62(8):2578-86.

60. Sharova N, Swingler C, Sharkey M, Stevenson M. Macrophages archive HIV-1 virions for dissemination in trans. EMBO J. 2005 Jul 6;24(13):2481-9.

61. Koppensteiner H, Banning C, Schneider C, Hohenberg H, Schindler M. Macrophage internal HIV-1 is protected from neutralizing antibodies. J Virol. 2012 Mar;86(5):2826-36.

62. Chu H, Wang JJ, Qi M, Yoon JJ, Wen X, Chen X, et al. The intracellular virus-containing compartments in primary human macrophages are largely inaccessible to antibodies and small molecules. PLoS One. 2012;7(5):e35297.

63. Kadiu I, Narayanasamy P, Dash PK, Zhang W, Gendelman HE. Biochemical and biologic characterization of exosomes and microvesicles as facilitators of HIV-1 infection in macrophages. J Immunol. 2012 Jul 15;189(2):744-54.

64. Groot F, Welsch S, Sattentau QJ. Efficient HIV-1 transmission from macrophages to T cells across transient virological synapses. Blood. 2008 May 1;111(9):4660-3.

65. Gousset K, Ablan SD, Coren LV, Ono A, Soheilian F, Nagashima K, et al. Real-time visualization of HIV-1 GAG trafficking in infected macrophages. PLoS Pathog. 2008 Mar 7;4(3):e1000015.

66. Gordon S. The macrophage. Bioessays. 1995;17(11):977 <last_page> 986.

67. Patel HM. Serum opsonins and liposomes: their interaction and opsonophagocytosis. Crit Rev Ther Drug Carrier Syst. 1992;9(1):39-90.

68. Najjar VA. Biological effects of tuftsin and its analogs. Drugs of the future. 1987;12(2):147; 147,160; 160.

69. Fridkin M. Tuftsin: its chemistry, biology, and clinical potential. Crit Rev Biochem Mol Biol. 1989;24(1):1; 1,40; 40.

70. Agrawal AK, Gupta CM. Tuftsin-bearing liposomes in treatment of macrophage-based infections. Adv Drug Deliv Rev. 2000;41(2):135 <last_page> 146.

71. Agarwal A. Tuftsin-bearing liposomes as rifampin vehicles in treatment of tuberculosis in mice. Antimicrob Agents Chemother. 1994;38(3):588; 588,593; 593.

72. Kim SS, Ye C, Kumar P, Chiu I, Subramanya S, Wu H, et al. Targeted delivery of siRNA to macrophages for anti-inflammatory treatment. Mol Ther. 2010 May;18(5):993-1001.

73. Qin J, Chen D, Hu H, Cui Q, Qiao M, Chen B. Surface modification of RGD-liposomes for selective drug delivery to monocytes/neutrophils in brain. Chem Pharm Bull (Tokyo). 2007 Aug;55(8):1192-7.

74. Senior RM, Gresham HD, Griffin GL, Brown EJ, Chung AE. Entactin stimulates neutrophil adhesion and chemotaxis through interactions between its Arg-Gly-Asp (RGD) domain and the leukocyte response integrin. J Clin Invest. 1992 Dec;90(6):2251-7.

75. Jain S, Mishra V, Singh P, Dubey PK, Saraf DK, Vyas SP. RGD-anchored magnetic liposomes for monocytes/neutrophils-mediated brain targeting. Int J Pharm. 2003 Aug 11;261(1-2):43-55.

76. Geijtenbeek TB, Gringhuis SI. Signalling through C-type lectin receptors: shaping immune responses. Nat Rev Immunol. 2009 Jul;9(7):465-79.

77. McGreal EP, Martinez-Pomares L, Gordon S. Divergent roles for C-type lectins expressed by cells of the innate immune system. Mol Immunol. 2004 Nov;41(11):1109-21.

78. Wijagkanalan W, Higuchi Y, Kawakami S, Teshima M, Sasaki H, Hashida M. Enhanced anti-inflammation of inhaled dexamethasone palmitate using mannosylated liposomes in an endotoxin-induced lung inflammation model. Mol Pharmacol. 2008 Nov;74(5):1183-92.

79. Kawakami S, Sato A, Nishikawa M, Yamashita F, Hashida M. Mannose receptor-mediated gene transfer into macrophages using novel mannosylated cationic liposomes. Gene Ther. 2000 Feb;7(4):292-9.

80. Kawakami S, Wong J, Sato A, Hattori Y, Yamashita F, Hashida M. Biodistribution characteristics of mannosylated, fucosylated, and galactosylated liposomes in mice. Biochim Biophys Acta. 2000 Dec 15;1524(2-3):258-65.

81. Chono S, Kaneko K, Yamamoto E, Togami K, Morimoto K. Effect of surface-mannose modification on aerosolized liposomal delivery to alveolar macrophages. Drug Dev Ind Pharm. 2010 Jan;36(1):102-7.

82. Chono S, Tanino T, Seki T, Morimoto K. Efficient drug targeting to rat alveolar macrophages by pulmonary administration of ciprofloxacin incorporated into mannosylated liposomes for treatment of respiratory intracellular parasitic infections. J Control Release. 2008 Apr 7;127(1):50-8.

83. Engel A, Chatterjee SK, Al-arifi A, Riemann D, Langner J, Nuhn P. Influence of spacer length on interaction of mannosylated liposomes with human phagocytic cells. Pharm Res. 2003 Jan;20(1):51-7.

84. Nakamura K, Kuramoto Y, Mukai H, Kawakami S, Higuchi Y, Hashida M. Enhanced gene transfection in macrophages by histidine-conjugated mannosylated cationic liposomes. Biol Pharm Bull. 2009 Sep;32(9):1628-31.

85. Espuelas S, Thumann C, Heurtault B, Schuber F, Frisch B. Influence of ligand valency on the targeting of immature human dendritic cells by mannosylated liposomes. Bioconjug Chem. 2008 Dec;19(12):2385-93.

86. Scott AM, Wolchok JD, Old LJ. Antibody therapy of cancer. Nat Rev Cancer. 2012 Mar 22;12(4):278-87.

87. Bestman-Smith J, Gourde P, Desormeaux A, Tremblay MJ, Bergeron MG. Sterically stabilized liposomes bearing anti-HLA-DR antibodies for targeting the primary cellular reservoirs of HIV-1. Biochim Biophys Acta. 2000 Sep 29;1468(1-2):161-74.

88. Homem de Bittencourt PI, Lagranha DJ, Maslinkiewicz A, Senna SM, Tavares AMV, Baldissera LP, et al. LipoCardium: Endothelium-directed cyclopentenone prostaglandin-based liposome formulation that completely reverses atherosclerotic lesions. Atherosclerosis. 2007;193(2):245 <last_page> 258.

89. Antony AC. The biological chemistry of folate receptors. Blood. 1992 Jun 1;79(11):2807-20.

90. Kamen BA, Smith AK, Anderson RG. The folate receptor works in tandem with a probenecid-sensitive carrier in MA104 cells in vitro. J Clin Invest. 1991 Apr;87(4):1442-9.

91. Leamon CP. Delivery of macromolecules into living cells: a method that exploits folate receptor endocytosis. Proceedings of the National Academy of Sciences - PNAS. 1991 -07;88(13):5572; 5572,5576; 5576.

92. Antony AC. Folate receptors. Annu Rev Nutr. 1996;16:501-21.

93. Shen F, Wu M, Ross JF, Miller D, Ratnam M. Folate receptor type gamma is primarily a secretory protein due to lack of an efficient signal for glycosylphosphatidylinositol modification: protein characterization and cell type specificity. Biochemistry. 1995 Apr 25;34(16):5660-5.

94. Reddy JA, Haneline LS, Srour EF, Antony AC, Clapp DW, Low PS. Expression and functional characterization of the beta-isoform of the folate receptor on CD34(+) cells. Blood. 1999 Jun 1;93(11):3940-8.

95. Xia W, Hilgenbrink AR, Matteson EL, Lockwood MB, Cheng JX, Low PS. A functional folate receptor is induced during macrophage activation and can be used to target drugs to activated macrophages. Blood. 2009 Jan 8;113(2):438-46.

96. Thomas TP, Goonewardena SN, Majoros IJ, Kotlyar A, Cao Z, Leroueil PR, et al. Folate-targeted nanoparticles show efficacy in the treatment of inflammatory arthritis. Arthritis Rheum. 2011 Sep;63(9):2671-80.

97. Furusho Y, Miyata M, Matsuyama T, Nagai T, Li H, Akasaki Y, et al. Novel Therapy for Atherosclerosis Using Recombinant Immunotoxin Against Folate Receptor beta-Expressing Macrophages. J Am Heart Assoc. 2012 Aug;1(4):e003079.

98. Hu J. Enhanced delivery of AZT to macrophages via acetylated LDL. J Controlled Release. 2000 -12;69(3):327; 327,335; 335.

99. Aouadi M, Tesz GJ, Nicoloro SM, Wang M, Chouinard M, Soto E, et al. Orally delivered siRNA targeting macrophage Map4k4 suppresses systemic inflammation. Nature. 2009 Apr 30;458(7242):1180-4.

100. Georganopoulou DG, Chang L, Nam J-, Thaxton CS, Mufson EJ, Klein WL, et al. From The Cover: Nanoparticle-based detection in cerebral spinal fluid of a soluble pathogenic biomarker for Alzheimer's disease. Proceedings of the National Academy of Sciences. 2005; 2005;102(7):2273 <last_page> 2276.

101. Na HB, Lee JH, An K, Park YI, Park M, Lee IS, et al. Development of a T_1 contrast agent for magnetic resonance imaging using MnO nanoparticles. Angew Chem Int Ed Engl. 2007;46(28):5397-401.

102. Slowing II, Trewyn BG, Lin VS. Mesoporous silica nanoparticles for intracellular delivery of membrane-impermeable proteins. J Am Chem Soc. 2007 Jul 18;129(28):8845-9.

103. Wu X, Liu H, Liu J, Haley KN, Treadway JA, Larson JP, et al. Immunofluorescent labeling of cancer marker Her2 and other cellular targets with semiconductor quantum dots. Nat Biotechnol. 2003 Jan;21(1):41-6.

104. Kohler N, Sun C, Fichtenholtz A, Gunn J, Fang C, Zhang M. Methotrexate-immobilized poly(ethylene glycol) magnetic nanoparticles for MR imaging and drug delivery. Small. 2006 Jun;2(6):785-92.

105. Medarova Z, Pham W, Farrar C, Petkova V, Moore A. In vivo imaging of siRNA delivery and silencing in tumors. Nat Med. 2007; 2007;13(3):372 <last_page> 377.

106. Caravan P. Strategies for increasing the sensitivity of gadolinium based MRI contrast agents. Chem Soc Rev. 2006 Jun;35(6):512-23.

107. Bulte JW, Kraitchman DL. Iron oxide MR contrast agents for molecular and cellular imaging. NMR Biomed. 2004 Nov;17(7):484-99.

108. Lu AH, Salabas EL, Schuth F. Magnetic nanoparticles: synthesis, protection, functionalization, and application. Angew Chem Int Ed Engl. 2007;46(8):1222-44.

109. Park J, Joo J, Kwon SG, Jang Y, Hyeon T. Synthesis of monodisperse spherical nanocrystals. Angew Chem Int Ed Engl. 2007;46(25):4630-60.

110. Gu H, Ho PL, Tsang KW, Wang L, Xu B. Using biofunctional magnetic nanoparticles to capture vancomycin-resistant enterococci and other gram-positive bacteria at ultralow concentration. J Am Chem Soc. 2003 Dec 24;125(51):15702-3.

111. Saiyed Z, Telang S, Ramchand C. Application of magnetic techniques in the field of drug discovery and biomedicine. Biomagn Res Technol. 2003 Sep 18;1(1):2.

112. Safarik I, Safarikova M. Magnetic techniques for the isolation and purification of proteins and peptides. Biomagn Res Technol. 2004 Nov 26;2(1):7.

113. Xu C, Xu K, Gu H, Zhong X, Guo Z, Zheng R, et al. Nitrilotriacetic acid-modified magnetic nanoparticles as a general agent to bind histidine-tagged proteins. J Am Chem Soc. 2004 Mar 24;126(11):3392-3.

114. Xu C, Xu K, Gu H, Zheng R, Liu H, Zhang X, et al. Dopamine as a robust anchor to immobilize functional molecules on the iron oxide shell of magnetic nanoparticles. J Am Chem Soc. 2004 Aug 18;126(32):9938-9.

115. Liong M, Lu J, Kovochich M, Xia T, Ruehm SG, Nel AE, et al. Multifunctional inorganic nanoparticles for imaging, targeting, and drug delivery. ACS Nano. 2008 May;2(5):889-96.

116. Kim J, Park S, Lee JE, Jin SM, Lee JH, Lee IS, et al. Designed fabrication of multifunctional magnetic gold nanoshells and their application to magnetic resonance imaging and photothermal therapy. Angew Chem Int Ed Engl. 2006 Nov 27;45(46):7754-8.

117. Wainberg MA. AIDS: Drugs that prevent HIV infection. Nature. 2011 Jan 20;469(7330):306-7.

118. Pretorius E, Klinker H, Rosenkranz B. The role of therapeutic drug monitoring in the management of patients with human immunodeficiency virus infection. Ther Drug Monit. 2011 Jun;33(3):265-74.

119. Lasic DD. Doxorubicin in sterically stabilized liposomes. Nature. 1996;380(6574):561 <last_page> 562.

120. Barenholz Y(. Doxil® — The first FDA-approved nano-drug: Lessons learned. J Controlled Release. 2012;160(2):117 <last_page> 134.

121. Torchilin VP. Recent advances with liposomes as pharmaceutical carriers. Nature Reviews Drug Discovery. 2005;4(2):145 <last_page> 160.

122. Liu Y, Pan J, Feng S. Nanoparticles of lipid monolayer shell and biodegradable polymer core for controlled release of paclitaxel: Effects of surfactants on particles size, characteristics and in vitro performance. Int J Pharm. 2010;395(1-2):243 <last_page> 250.

123. Avgoustakis K. Pegylated Poly(Lactide) and Poly(Lactide-Co-Glycolide) Nanoparticles: Preparation, Properties and Possible Applications in Drug Delivery. Current Drug Delivery. 2004;1(4):321 <last_page> 333.

124. Cho K, Wang X, Nie S, Chen ZG, Shin DM. Therapeutic nanoparticles for drug delivery in cancer. Clin Cancer Res. 2008 Mar 1;14(5):1310-6.

125. Panyam J, Labhasetwar V. Biodegradable nanoparticles for drug and gene delivery to cells and tissue. Adv Drug Deliv Rev. 2003;55(3):329 <last_page> 347.

126. Chan JM, Zhang L, Yuet KP, Liao G, Rhee JW, Langer R, et al. PLGA-lecithin-PEG core-shell nanoparticles for controlled drug delivery. Biomaterials. 2009 Mar;30(8):1627-34.

127. Guthi JS, Yang SG, Huang G, Li S, Khemtong C, Kessinger CW, et al. MRI-visible micellar nanomedicine for targeted drug delivery to lung cancer cells. Mol Pharm. 2010 Feb 1;7(1):32-40.

128. Lebel RM, Menon RS, Bowen CV. Relaxometry model of strong dipolar perturbers for balanced-SSFP: application to quantification of SPIO loaded cells. Magn Reson Med. 2006 Mar;55(3):583-91.

129. Liu W, Dahnke H, Rahmer J, Jordan EK, Frank JA. Ultrashort T_2* relaxometry for quantitation of highly concentrated superparamagnetic iron oxide (SPIO) nanoparticle labeled cells. Magn Reson Med. 2009 Apr;61(4):761-6.

130. Girard OM, Ramirez R, McCarty S, Mattrey RF. Toward absolute quantification of iron oxide nanoparticles as well as cell internalized fraction using multiparametric MRI. Contrast Media Mol Imaging. 2012 Jul-Aug;7(4):411-7.

131. Sihorkar V, Vyas SP. Potential of polysaccharide anchored liposomes in drug delivery, targeting and immunization. J Pharm Pharm Sci. 2001 May-Aug;4(2):138-58.

132. Kabanov AV, Gendelman HE. Nanomedicine in the diagnosis and therapy of neurodegenerative disorders. Prog Polym Sci. 2007;32(8-9):1054-82.

133. Nowacek AS, Balkundi S, McMillan J, Roy U, Martinez-Skinner A, Mosley RL, et al. Analyses of nanoformulated antiretroviral drug charge, size, shape and content for uptake, drug release and antiviral activities in human monocyte-derived macrophages. J Control Release. 2011 Mar 10;150(2):204-11.

134. Mascheri N, Dharmakumar R, Zhang Z, Paunesku T, Woloschak G, Li D. Fast low-angle positive contrast steady-state free precession imaging of USPIO-labeled macrophages: theory and in vitro experiment. Magn Reson Imaging. 2009 Sep;27(7):961-9.

135. Beduneau A, Ma Z, Grotepas CB, Kabanov A, Rabinow BE, Gong N, et al. Facilitated monocyte-macrophage uptake and tissue distribution of superparmagnetic iron-oxide nanoparticles. PLoS One. 2009;4(2):e4343.

136. Balkundi S, Nowacek AS, Veerubhotla RS, Chen H, Martinez-Skinner A, Roy U, et al. Comparative manufacture and cell-based delivery of antiretroviral nanoformulations. Int J Nanomedicine. 2011;6:3393-404.

137. Nowacek AS, McMillan J, Miller R, Anderson A, Rabinow B, Gendelman HE. Nanoformulated antiretroviral drug combinations extend drug release and antiretroviral responses in HIV-1-infected macrophages: implications for neuroAIDS therapeutics. J Neuroimmune Pharmacol. 2010 Dec;5(4):592-601.

138. Nowacek AS, Miller RL, McMillan J, Kanmogne G, Kanmogne M, Mosley RL, et al. NanoART synthesis, characterization, uptake, release and toxicology for human monocyte-macrophage drug delivery. Nanomedicine (Lond). 2009 Dec;4(8):903-17.

139. Wessels E, Simpson JC. Impact of live cell imaging on coated vesicle research. Semin Cell Dev Biol. 2007;18(4):412 <last_page> 423.

140. Kingsley JD, Dou H, Morehead J, Rabinow B, Gendelman HE, Destache CJ. Nanotechnology: a focus on nanoparticles as a drug delivery system. J Neuroimmune Pharmacol. 2006 Sep;1(3):340-50.

141. Huang J, Gautam N, Bathena SP, Roy U, McMillan J, Gendelman HE, et al. UPLC-MS/MS quantification of nanoformulated ritonavir, indinavir, atazanavir, and efavirenz in mouse serum and tissues. J Chromatogr B Analyt Technol Biomed Life Sci. 2011 Aug 1;879(23):2332-8.

142. Roy U, McMillan J, Alnouti Y, Gautum N, Smith N, Balkundi S, et al. Pharmacodynamic and antiretroviral activities of combination nanoformulated antiretrovirals in HIV-1-infected human peripheral blood lymphocyte-reconstituted mice. J Infect Dis. 2012 Nov 15;206(10):1577-88.

143. Ganz T, Nemeth E. Iron metabolism: interactions with normal and disordered erythropoiesis. Cold Spring Harb Perspect Med. 2012 May;2(5):a011668.

144. Andrews NC. Forging a field: the golden age of iron biology. Blood. 2008 Jul 15;112(2):219-30.

145. McCarthy JR, Weissleder R. Multifunctional magnetic nanoparticles for targeted imaging and therapy. Adv Drug Deliv Rev. 2008 Aug 17;60(11):1241-51.

146. Keegan ME, Whittum-Hudson JA, Mark Saltzman W. Biomimetic design in microparticulate vaccines. Biomaterials. 2003 Nov;24(24):4435-43.

147. Talelli M, Rijcken CJ, Lammers T, Seevinck PR, Storm G, van Nostrum CF, et al. Superparamagnetic iron oxide nanoparticles encapsulated in biodegradable thermosensitive polymeric micelles: toward a targeted nanomedicine suitable for image-guided drug delivery. Langmuir. 2009 Feb 17;25(4):2060-7.

148. Balkundi S, Nowacek AS, Roy U, Martinez-Skinner A, McMillan J, Gendelman HE. Methods development for blood borne macrophage carriage of nanoformulated antiretroviral drugs. J Vis Exp. 2010 Dec 9;(46). pii: 2460. doi(46):10.3791/2460.

149. Puligujja P, McMillan J, Kendrick L, Li T, Balkundi S, Smith N, et al. Macrophage folate receptor-targeted antiretroviral therapy facilitates drug entry, retention, antiretroviral activities and biodistribution for reduction of human immunodeficiency virus infections. Nanomedicine. 2013 Nov;9(8):1263-73.

150. Jung CW, Jacobs P. Physical and chemical properties of superparamagnetic iron oxide MR contrast agents: ferumoxides, ferumoxtran, ferumoxsil. Magn Reson Imaging. 1995;13(5):661-74.

151. Tong S, Hou S, Zheng Z, Zhou J, Bao G. Coating optimization of superparamagnetic iron oxide nanoparticles for high T_2 relaxivity. Nano Lett. 2010 Nov 10;10(11):4607-13.

152. Maity D, Chandrasekharan P, Yang CT, Chuang KH, Shuter B, Xue JM, et al. Facile synthesis of water-stable magnetite nanoparticles for clinical MRI and magnetic hyperthermia applications. Nanomedicine (Lond). 2010 Dec;5(10):1571-84.

153. Huang X, Zhuang J, Chen D, Liu H, Tang F, Yan X, et al. General strategy for designing functionalized magnetic microspheres for different bioapplications. Langmuir. 2009 Oct 6;25(19):11657-63.

154. Zhang L, Yu F, Cole AJ, Chertok B, David AE, Wang J, et al. Gum arabic-coated magnetic nanoparticles for potential application in simultaneous magnetic targeting and tumor imaging. AAPS J. 2009 Dec;11(4):693-9.

155. Liang YY, Zhang LM, Jiang W, Li W. Embedding magnetic nanoparticles into polysaccharide-based hydrogels for magnetically assisted bioseparation. Chemphyschem. 2007 Nov 12;8(16):2367-72.

156. Sanganeria P, Sachar S, Chandra S, Bahadur D, Ray P, Khanna A. Cellular internalization and detailed toxicity analysis of protein-immobilized iron oxide nanoparticles. J Biomed Mater Res B Appl Biomater. 2014 Apr 30.

157. Rogers MJ. New insights into the molecular mechanisms of action of bisphosphonates. Curr Pharm Des. 2003;9(32):2643-58.

158. Guo D, Li T, McMillan J, Sajja BR, Puligujja P, Boska MD, et al. Small magnetite antiretroviral therapeutic nanoparticle probes for MRI of drug biodistribution. Nanomedicine (Lond). 2013 Aug 1.

159. Pierson T, McArthur J, Siliciano RF. Reservoirs for HIV-1: mechanisms for viral persistence in the presence of antiviral immune responses and antiretroviral therapy. Annu Rev Immunol. 2000;18:665-708.

160. Saksena NK, Wang B, Zhou L, Soedjono M, Ho YS, Conceicao V. HIV reservoirs in vivo and new strategies for possible eradication of HIV from the reservoir sites. HIV AIDS (Auckl). 2010;2:103-22.

161. Nowacek AS, Balkundi S, McMillan J, Roy U, Martinez-Skinner A, Mosley RL, et al. Analyses of nanoformulated antiretroviral drug charge, size, shape and content for uptake, drug release and antiviral activities in human monocyte-derived macrophages. J Controlled Release. 2011 3/10;150(2):204-11.

162. Puligujja P, McMillan J, Kendrick L, Li T, Balkundi S, Smith N, et al. Macrophage folate receptor-targeted antiretroviral therapy facilitates drug entry, retention, antiretroviral activities and biodistribution for reduction of human immunodeficiency virus infections. Nanomedicine. 2013 Nov;9(8):1263-73.

163. Liu W, Dahnke H, Rahmer J, Jordan EK, Frank JA. Ultrashort T_2* relaxometry for quantitation of highly concentrated superparamagnetic iron oxide (SPIO) nanoparticle labeled cells. Magn Reson Med. 2009 Apr;61(4):761-6.

164. Martinez-Skinner AL, Veerubhotla RS, Liu H, Xiong H, Yu F, McMillan JM, et al. Functional proteome of macrophage carried nanoformulated antiretroviral therapy demonstrates enhanced particle carrying capacity. J Proteome Res. 2013 May 3;12(5):2282-94.

165. Puligujja P, Balkundi SS, Kendrick LM, Baldridge HM, Hilaire JR, Bade AN, et al. Pharmacodynamics of long-acting folic acid-receptor targeted ritonavir-boosted atazanavir nanoformulations. Biomaterials. 2015 Feb;41:141-50.

166. Huang J, Gautam N, Bathena SP, Roy U, McMillan J, Gendelman HE, et al. UPLC-MS/MS quantification of nanoformulated ritonavir, indinavir, atazanavir, and efavirenz in mouse serum and tissues. J Chromatogr B Analyt Technol Biomed Life Sci. 2011 Aug 1;879(23):2332-8.